Flapping Motion of a Three-Dimensional Foil for Propulsion and Maneuvering of Underwater Vehicles

by

Melissa Dawn Flores

B. S. in Ocean Engineering
Massachusetts Institute of Technology, 2002

Submitted to the Department of Ocean Engineering
in partial fulfillment of the requirements for the degree of

Master of Science in Ocean Engineering

at the

MASSACHUSETTS INSTITUTE OF TECHNOLOGY

June 2003

Author .....
Department of Ocean Engineering
May 12, 2003

Certified by .....
Michael S. Triantafyllou
Professor of Ocean Engineering
Thesis Supervisor

Accepted by .....
Michael S. Triantafyllou
Chairman, Departmental Committee on Graduate Students

Flapping Motion of a Three-Dimensional Foil for Propulsion and Maneuvering of Underwater Vehicles

by

Melissa Dawn Flores

Submitted to the Department of Ocean Engineering
on May 12, 2003, in partial fulfillment of the
requirements for the degree of
Master of Science in Ocean Engineering

Abstract

Experiments were performed on a three-dimensional NACA 0015 foil with a 5.5 cm average chord and 24.3 cm span performing a combined roll and pitch motion. The trailing edge of the foil was tapered. The motion was produced by harmonically rolling and pitching the foil near the root using two-axis control. Tests to determine the mean thrust coefficient of the foil were conducted over a wide parametric space. This parameter space included two roll amplitudes, with induced heave (at the 0.7 span) to chord ratio of $h_{0.7}/c = 1.00$ and 1.50; respectively, with Strouhal numbers ranging from 0.20 to 0.80; and maximum angle of attack varying between 15 and 50 degrees. The angle of attack and Strouhal number were also defined using the motion at the 0.7 span. A planform area mean thrust coefficient of 2.07 was recorded for 40 degrees maximum angle of attack and $h_{0.7}/c = 1.50$. Experiments to measure the mean lift and thrust coefficient were performed after adding a static bias to the foil pitch. Mean lift coefficients of near 4 were achieved in this manner. Further maneuvering tests were accomplished by measuring the forces produced by an impulsively starting foil in still water and at $U = 0.4\ m/s$. Peak forces and impulse were measured for pitch angles between 30 and 90 degrees and for three different roll velocities. The highest propulsive impulse measured was 2.25 Newton-seconds at a maximum roll amplitude of 1.28 m/s and pitch angle of 40 degrees.

Wake velocities were measured using Laser Doppler Velocimetry (LDV) and Digital Particle Imaging Velocimetry (DPIV) in three ancillary experiments. First, mean velocities across the wake at five spanwise locations were recorded using LDV. The wake width was found to be the excursion of the foil at the 70% span, validating our previous assumption. In the second experiment, using LDV, we measured the phase-average velocity and produced a three-dimensional plot of the wake behind the foil at the 0.7 span. Finally, DPIV for the same flapping parameters map the velocity field in the wake for various foil positions in a half-cycle.

Thesis Supervisor: Michael S. Triantafyllou
Title: Professor of Ocean Engineering

Acknowledgments

I would first like to thank my colleagues Victor Polidoro and Stephen Licht for building the flapping foil module. They can take some comfort in the fact that their module was used for something, even if it didn't end up on their AUV. They are both very talented engineers and answered my millions of questions with patience. Thanks also to Karl McLetchie for the foil mold and for keeping me going through the last hours of the PIV tests with gram crackers. Thanks to my UROP Maggie Loftus for keeping me on track and excited about the project!

My advisor, Prof. Triantafyllou, and research engineers, Dr. Franz Hover and Dr. Rich Kimball, really guided me through this whole experience. I wouldn't have gotten anywhere without their ideas, support, and advice. Thanks also to Prof. Alexandra Techet for all of her help in using DPIV.

I would also like to acknowledge the financial support of SNAME through the William M. Kennedy Scholarship, and the Ocean Engineering Department at MIT. Both SNAME and our Department are incredibly supportive of research endeavors for students like myself, and it really wouldn't be possible for me to stay at MIT for this degree without that support.

Last but certainly not least, I would like to thank my husband, Praxedis. Thank you for a wonderful wedding and honeymoon in the middle of all of this research! You make me believe that I can accomplish anything, and with your support and understanding I know that I can.

Nomenclature

c	average foil chord in meters, 0.055
s	foil span in meters, 0.243
U	propeller tunnel steady inflow speed in meters per second
u	LDV measured velocity in the U direction
ρ	fluid density
ν	fluid kinematic viscosity
Re	chord Reynolds Number, Uc/ν
θ_o	amplitude of sinusoidal pitch motion $\theta(t)$
ϕ_o	amplitude of sinusoidal roll motion $\phi(t)$
R_0	distance from center of roll axis to root of the foil in meters, 0.218
d/s	fraction of span
$R_{d/s}$	distance from center of roll axis to d/s of span, $R_0 + d$
$R_{0.7}$	distance from center of roll axis to 70% of span, $R_0 + 0.7s$
β	angle of attack due to roll motion only
α_{max}	maximum angle of attack
$2h_{0.7}$	wake width at $R_{0.7}$ (arclength), $2R_{0.7}\phi_o$
$h_{0.7}/c$	normalized wake width
f	frequency of foil motion in Hertz
T	period of foil motion in seconds
ω	frequency of foil motion in radians per second
St	Strouhal number, $2h_{0.7}f/U$
$F_x(t)$	thrust force in Newtons; mean value $\overline{F}_x$
$F_y(t)$	lift force in Newtons; mean value $\overline{F}_y$

C_T mean thrust coefficient, $2\overline{F}_x/\rho U^2 cs$

C_L mean lift coefficient, $2\overline{F}_y/\rho U^2 cs$

SA swept area of $R_{0.7}$ (arclength), $2\phi_o({R_{0.7}}^2 + 2R_0R_{0.7})$

$C_{T_{SA}}$ mean thrust coefficient, $2\overline{F}_x/\rho U^2 SA$

AR aspect ratio, $AR = s/c = 4.4$

p momentum, $F(t) = \frac{dp}{dt}$

J impulse in either the global X or Y direction, $p_f - p_i$

t_r rise time of impulse (time to rise from 10% to 90% of final value)

t_p peak time of impulse (the time required for the response to reach the peak of the overshoot from 10% of its final value)

M_p Maximum (percent) overshoot of impulse

t_s settling time of impulse (the time required for the response to reach and stay within 5% of its final value from 10% of its final value)

Contents

List of Figures

List of Tables

Chapter 1

Introduction

Despite impressive innovations in underwater robotics, both the military and scientific communities would benefit from more maneuverable vehicles for which current propeller systems are impractical. This work focuses on the feasibility of applying a mechanical model of the oscillatory fin motion used by fish in an autonomous underwater vehicle (AUV) for propulsion. Results from experiments done at MIT using a flapping foil in two-dimensional heave and pitch motion show net thrust production for propulsion as well as net lift through biasing of the foil for use in maneuvering. In this project, experiments were conducted with similar goals in mind, but instead using a hydrofoil in a three dimensional oscillatory motion to mimic that of the figure-eight flapping pattern observed in some species of fish.

Fish, birds, and insects share a common source of propulsion and maneuvering by all using flapping appendages that can generally flap as well as twist with respect to an axis fixed to their bodies. Here we focus on the lift-based oscillatory motion produced by the ocean sunfish (as well as other particular species of fish), sea turtles, penguins, and sea lions. The fact that these animals can produce significant thrust makes flapping foil propulsion an interesting area of research for scientists and engineers. To improve the performance of our designs, we need to study and quantify the characteristics of this type of locomotion.

The basic flow mechanism of the oscillating foil is the vortex wake. In general, a flapping foil generates a vortex wake where the vortices are shed at the extreme

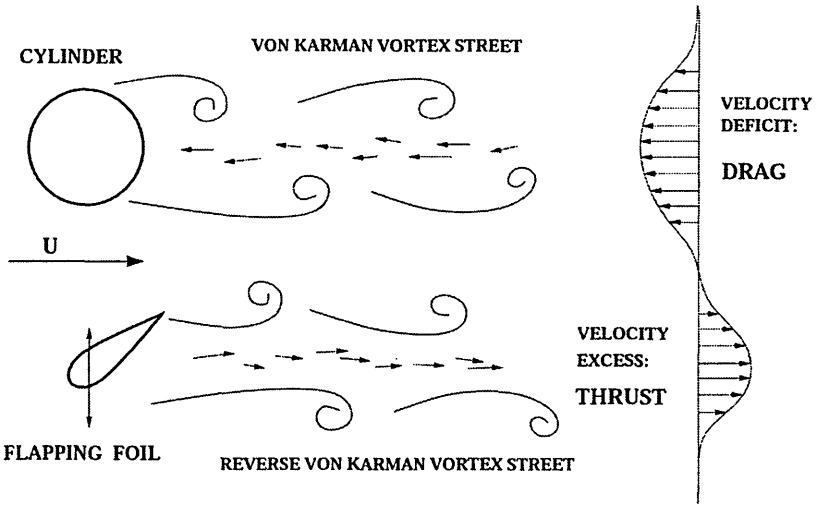

Figure 1-1: Von Kármán vortex street and reverse von Kármán street behind a flapping foil, F. Hover

amplitudes, producing a reverse von Kármán vortex street. In a bluff body, vortex shedding produces drag while a flapping foil can produce net thrust [1].

Many researchers have focused on the hydrodynamic and aerodynamic performance of steady wings at constant angles of attack. The classical theory of oscillating airfoils was developed by T. Theodorsen, T. Von Karman, and W. R. Sears in the 1930's as a result of interest in aircraft flutter problem [2]. Another useful application of the classical theory is in biofluiddynamics, the study of fluid flow around the wings of birds and insects and the fins of fish. As we will see in the literature review, a number of researchers have since looked at the unsteady flow around oscillating wings. Existing data on flapping foils are derived from biological experiments on birds, insects, and fish, as well as qualitative flow visualization and quantitative thrust and efficiency data measurements on hydrofoils. A selection of these investigations are described here.

1.1 Previous Work

The parameters discussed in these papers are the reduced frequency (k), the Strouhal number (St), the Reynolds number (Re), the heave amplitude to chord ratio (h_o/c), the pitch angle amplitude (θ), and the mean angle of attack (α).

The reduced frequency is defined as:

$$k = \frac{\omega c}{2U} \tag{1.1}$$

where ω is the frequency in rad/sec, c is the chord length in meters, and U is the free-stream velocity. The Strouhal number is defined as:

$$St = \frac{2h_o f}{U} \tag{1.2}$$

where f is the heave frequency in Hz and $2h_o$ is an estimate of the wake width in meters.

The Reynolds number is defined as:

$$Re = \frac{Uc}{\nu} \tag{1.3}$$

where ν is the kinematic viscosity coefficient.

Freymuth (1988) [3] performed experiments on a NACA 0015 foil in both pure pitch and pure plunge. These experiments were conducted in a low-speed wind tunnel, with foil-chord Reynolds numbers between 5,200 and 12,000. These experiments focused on flow visualization, with particular interest in the vortex pattern produced by the individual motions. Results of both pure plunging and pure pitching motion showed the 'propulsive vortical signature' as a staggered vortex street which forms a jet-like velocity component away from the foil.

He observed in the plunging case that for an angle of attack of 5 degrees two

strong trailing vortices shed per cycle. He identified weak leading edge separation travelling down the foil and merged with the trailing edge vortex. This leading edge vortex reinforced the trailing edge vortex formation. It was also observed that when alpha became much larger than 5 degrees, strong leading edge separation weakened the generation of the thrust vortex. He finally noted that reducing the frequency of oscillation for high alpha caused the distance between vortices to reduce, and for low enough frequency of oscillation the drag producing vortex pattern emerged.

Koochesfahani (1987) [2] conducted more extensive tests on a NACA 0012 foil pitching about its quarter-chord point. These tests were conducted in a low speed water channel at Reynolds number of about 12,000 and sinusoidal and non-sinusoidal profiles at small pitch amplitudes of 2 and 4 degrees. The frequency of oscillation was gradually increased to show the transition from the drag vortex wake to the thrust vortex wake. The mean velocity profile of the wake was measured using laser doppler velocimetry (LDV) to compliment the dye visualization.

Koochesfahani reports that for low frequencies, Kármán vortices are shed, representing a drag wake. At higher values of frequency, a reverse Kármán street is observed, creating a velocity component pointing downstream to create a jet. These results agreed with numerical calculation, but Koochesfahani warns that the critical frequency, k, calculated numerically which represents a transition from drag to thrust wake was not constant in his experiments. He noted that generally the frequency for vortex roll-up in the wake depended on the oscillation amplitude, with the critical value decreasing as the oscillation increased.

He notes the special case of transition where the vortices are in line downstream, representing a condition where there is neither drag or thrust. The thrust producing quality of the wake cancels the airfoil drag. He concludes by stating that the structure of the wake is dependent on the amplitude, frequency, and shape of the oscillation.

J. Anderson (1996) [4] performed Digital Particle Image Velocimetry (DPIV) on a foil oscillating in both heave and pitch. She created a vortex pattern map showing wake patterns on a plot of Strouhal number verses angle of attack for $h_o/c = 1.0$.

Figure 1-2 shows six different wake regions A-F. In reviewing previous flow visu-

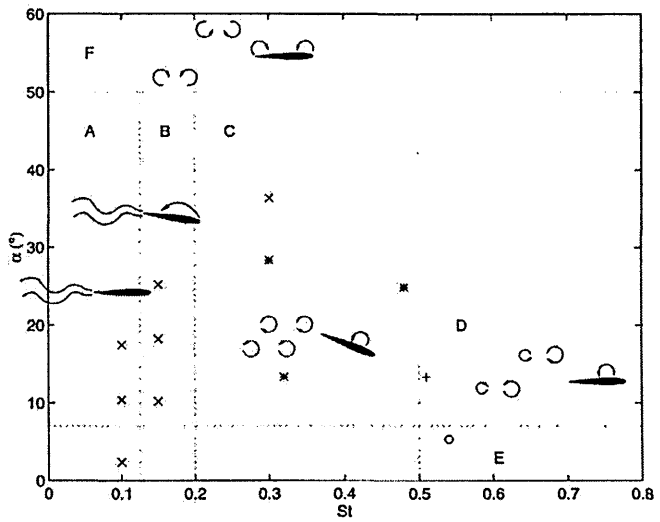

Figure 1-2: Wake pattern as function of St and α for $h_0/c = 1.0$, Anderson (1996).

alization work on a flapping foil, Haugsdal [5] summarizes that the following characteristics were found:

A. von Kármán street along the path of the trailing edge is evident.

B. Similar to A, the difference is a weak leading edge vortex has started to form, even at low angle of attack.

C. Contains two vortices per cycle reverse Kármán street.

D. Four vortices are shed per cycle, two from the leading edge and two from the trailing edge.

E. Four vortices are shed per cycle which all originate from the trailing edge.

F. The "piston mode" shedding characterized by very high angle of attack, $\alpha > 50°$.

One of the main conclusions from Anderson is that the shape of the angle of attack profile significantly influences wake structure. This profile is nominally harmonic, but deforms as the Strouhal number increases. Sinusoid and square wave profiles produced the clearest wakes, with two vortices shed per cycle. Multiple peaks in the angle of attack profile at high Strouhal number cause additional shedding which mixes the wake.

Read [6] furthermore summarizes Anderson's work:

> While region C is the region of optimal wake pattern for efficiency and thrust, the vortex interactions that create the thrust vortex wake do vary with heave amplitude. Anderson made observations in this region for three heave amplitudes. For small heave amplitude ($h_o/c = 0.25$), the vortex wake is dominated by trailing edge vortices. For intermediate heave amplitude ($h_o/c = 0.50$), both leading and trailing edge vortices contribute to producing the jet. For the largest amplitude tested ($h_o/c = 1.00$), she observed a thrust vortex wake dominated by leading edge vortices. These observations led Anderson to conclude that even though the thrust wake is produced for several heave amplitudes, the optimum double amplitude is of the same order as the chord length.

Triantafyllou et al (1991) (1993) (1996) [7] [8] [1] Professor M. Triantafyllou and his research staff at MIT performed experiments on a NACA 0012 foil in pitch and heave. Experiments were done to measure mean thrust force coefficients and efficiency. A large parameter space was tested. The test matrix included three heave amplitudes, $h_o/c = [0.25, 0.50, 0.75]$. Maximum angle of attack ranged from $\alpha_{max} = 5°$ to 30° in 5° increments. Strouhal number ranged from about St = 0.05 to 0.55, and phase angles of $\psi = [75°, 90°, 105°]$ were tested.

The test parameters and experimental configuration were very similar to the apparatus used by Read [6] and Haugsdal [5]. Read summarizes the results of Triantafyllou et al:

> For $h_0/c = 0.75$, $\alpha_{max} = 20.2°$, and $\psi = 75°$, a maximum efficiency of 87% was obtained at St = 0.30. For the same parameters at St = 0.46, an efficiency of just over 80% was obtained with a thrust coefficient of approximately 0.83. The highest thrust coefficient reported was about 1.6 for $h_0/c = 0.75$, $\psi = 90°$, St = 0.48, and $\alpha_{max} = 30°$. The efficiency for that run was just over 70%.
>
> The experimental values of thrust, power, and efficiency were compared to analytical and numerical solutions. Linear theory from Lighthill [9] [10] was used for analytical prediction, while numerical simulation from Streitlien and Triantafyllou [8] was used for non-linear prediction. For the high performance parameter set described above, experimental efficiency was higher than that predicted by either linear or non-linear theory. The authors attributed this discrepancy to the formation of strong leading edge dynamic stall vortices.

D. Read (2000) [6] Read did experiments to investigate the propulsion and maneuvering forces produced by a heaving and pitching foil. Tests were completed at

the MIT Towing Tank on a harmonically heaving and pitching NACA 0012 foil with a span of 60 cm and chord length of 10 cm. Experiments to determine the thrust coefficient and propulsive efficiency of the foil were conducted over a large parameter space. This parameter space included two heave amplitudes, $h_o/c = 0.75$ and 1.00, and phase angles between heave and pitch $\psi = [70°, 80°, 90°, 100°, 110°]$. Strouhal number ranged from 0.05 to 0.60 and maximum angles of attack varied between 10 and 50 degrees. All tests were done at a Reynolds number of 40,000. An extensive study of angle of attack profile was conducted.

He records planform area thrust coefficients of 2.4 for 35 degrees maximum angle of attack and efficiencies of up to 71.5% for 15 degrees maximum angle of attack. A plateau of good efficiency, in the range of 50% to 60%, was shown. He notes that generally a phase angle of 90° was most desirable, since phase angles other than 90° are more susceptible to corrupted angle of attack profiles, i.e. the distortions appear at lower Strouhal number. Higher order heave motion was implemented to alter undesirable angle of attack profiles with encouraging results. He observed that the performance decline caused by phase angles other than 90 degrees is negated. He therefore suggests that controlling the angle of attack through slight modifications to motion motion should be studied further, but could be difficult to implement on motion control cards other than the one he used.

He next investigated mechanisms to produce mean lift and showed that high mean lift coefficients could be achieved by adding a static bias to the foil pitch. Mean lift coefficients of over 4 were achieved in this manner. He measured both the thrust and lift mean coefficients, and then produced radial vector plots. These vectors show what he calls 'good vectoring capability' that would be useful in maneuvering.

A series of experiments were then conducted starting the foil from rest. Two different motions were tried. These impulsive starts showed very high instantaneous forces. He states in summary that the forces involved appear to be limited only by the maximum velocity of the foil, and that different foil motions create different instantaneous force vectors. This would allow a body to provide a variety of maneuvers from rest.

Walker and Westneat (1997) (2000) [11] [12] Walker and Westneat conducted an experiment to research fish locomotion for *Gomphosus Varius*, one of the many species of fish that use oscillating pectoral fins for maneuvering and propulsion. They observed that in *G. Varius* the fin oscillates largely up and down in a slightly inclined figure-eight pattern with respect to the fish's body, and both frequency and area swept by the pectoral fins increased linearly with increasing swimming speed. They concluded from their study that:

> Kinematic data, direct force measurement, and some flow visualization data suggest that the fins of *G. Varius* function in a strikingly similar manner to the wings of insects. This suggests that the lift-based mechanism in insects and fishes has converged on a similar pattern either as a result of shared design constraints of the flapping appendage or as a common goal of thrust maximization.

Interestingly they report that the *G. Varius* does not use a more drag-based mechanism at the lower speeds investigated in that study and, perhaps as a consequence, cannot swim steadily at low relative speeds.

Next Westneat and Walker performed a computer simulation to compare the mechanical performance of rowing and flapping appendages across a range of speeds. Flapping appendages proved to be more mechanically efficient than rowing appendages at all swimming speeds, suggesting that animals that frequently engage in locomotor behaviors that require energy conservation should employ a flapping stroke. They note that this begs the question of why rowing occurs at all. The authors suggest that one answer lies in the ability of rowing fins to generate more thrust than flapping fins during the power stroke (the down- or backstroke half of the motion). Large forces are necessary for maneuvering behaviors such as accelerations, turning, and braking. Therefore it is possible that there is a trade-off where at some relatively low speed rowing becomes desirable for maneuvering, while generally nature prefers flapping. Evidence of this is that species that make aquatic migrations, such as fur seals and sea lions, employ the flapping method [13].

Haugsdal (2000) [5] Haugsdal performed experiments at the MIT Towing Tank on a NACA 0014 foil oscillating in pitch and heave. Tests to determine the thrust

coefficient and propulsive efficiency of the foil were conducted over a large parameter space. Strouhal number ranged from 0.10 to 0.80 and maximum angles of attack varied between 10 and 35 degrees. The heave amplitude was $h_o/c = 1.0$ and with a 90 degree phase angle between heave and pitch. Four different angle of attack profiles were studied: square profile, saw tooth profile, cosine profile, and profile caused by simple harmonics in both heave and pitch motion. Flow visualization using dye for these different cases is included as well. Finally, some starting maneuvers were performed in which the foil performed one cycle in heave and pitch in still water.

The cosine angle of attack profile performed best. Efficiency of 64% and a thrust coefficient of 0.624 was found for a Strouhal number of 0.35 and 20 degrees maximum angle of attack. Comparison with propeller efficiency shows lower efficiency at corresponding thrust coefficient. However, Haugsdal notes that except for the motion control nothing is done to optimize the foil. The thickness over chord ratio, chord along the span, trailing edge, h_o/c, and motion control of the flap could all be optimized.

The flow visualization explains why the cosine angle of attack profile performed best. For the cosine profile, only two thrust vortices are observed, while for high Strouhal numbers the simple harmonics produced two thrust and four drag vortices. He notes that the the drag vortices can be expected when the angle of attack profile has more than two inflection points. Therefore, one can predict *a priori* from the angle of attack profile when drag vortices will be produced.

Three methods for starting maneuvers were employed, varying the duration of the down and upward stroke. The motion itself differed from the motion for propulsion in that the maximum heave and pitch coincided, instead of being out of phase. The motion was therefore more like a fish tail flapping back and forth instead of a smooth oscillation. Relatively large forces were found. Equal duration of the up and down stroke proved to be the best, producing relatively large maximum instantaneous forces near 50 N ($C_X = 3.36$ by non-dimensionalizing by the maximum heave velocity).

Chapter 2

Variable Study

2.1 Equations of Motion

All experiments were conducted using simple sinusoidal harmonic motion. The roll motion as a function of time, t, is

$$\phi(t) = \phi_o \sin(\omega t) \tag{2.1}$$

where ϕ_o is the roll amplitude in radians (or degrees), ω is the frequency is rad/sec, and time, t, is in seconds. The pitch motion is then

$$\theta(t) = \theta_o \sin(\omega t + \frac{\pi}{2}) \tag{2.2}$$

where θ_o is the pitch amplitude in radians.

We know that it is important to know the shape of the resulting angle of attack profile from a given combination of parameters. The three-dimensional case differs from the two-dimensional case because the angle of attack profile is a function of span for the 3-D case. Here we use the 2-D formulation, then plot the angle of attack for different spanwise locations. First, for a foil undergoing only a roll motion the angle of attack as a function of span and time is:

$$\beta(R_{d/s}, t) = \arctan \frac{R_{d/s}\dot{\phi}(t)}{U} \tag{2.3}$$

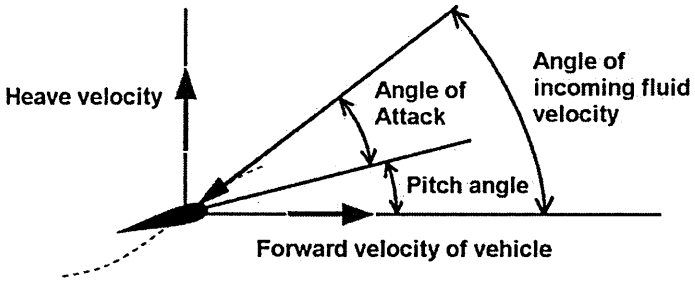

Figure 2-1: Foil Parameters, Polidoro (2003)

$$R_{d/s} = R_0 + d \tag{2.4}$$

where d is measured in meters and is a percentage of the span, R_0 is the distance from the center of rotation to the hub in meters (which was 0.218 meters), and d/s is therefore a non-dimensional number between 0 and 1 that gives a fraction of the span. For example, $R_{0.7}$ is 0.388 meters. We have to include the R_0 distance because the roll velocity is non-zero at the root of the foil. U is the incoming flow speed in meters/sec and $\dot{\phi}(t)$ is the derivative of the roll velocity. Figure 2-1 shows the foil parameters. Pitching the foil (using a positive θ_o), decreases the angle of attack and thus for a rolling and pitching foil, we subtract the angle of attack due to pitch from the angle of attack due to roll:

$$\alpha(s,t) = \beta(s,t) - \theta(t) \tag{2.5}$$

$$\alpha(s,t) = \arctan(\frac{s\dot{\phi}(t)}{U}) - \theta(t) \tag{2.6}$$

We then solve for the derivative of roll velocity:

$$\dot{\phi}(t) = \phi_o \omega \cos(\omega t) \tag{2.7}$$

Substituting equations 2.7 and 4.5 into 2.6, we have the equation for the maximum

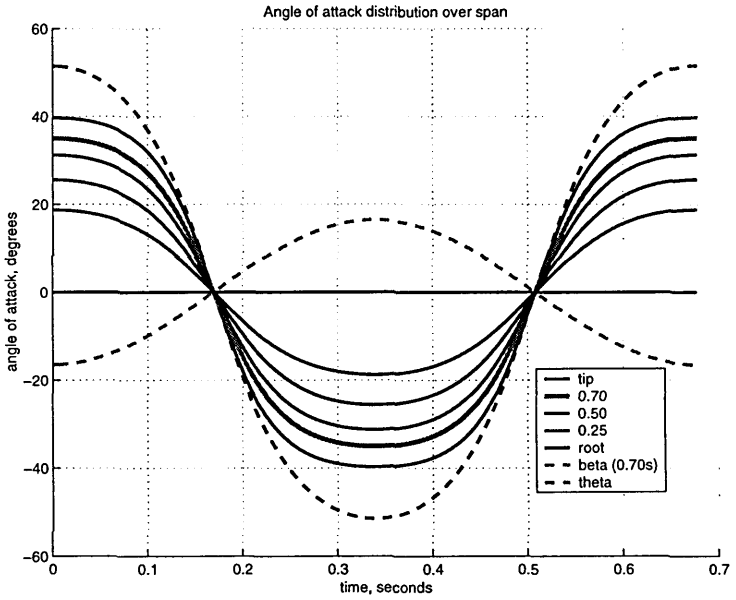

Figure 2-2: Sample angle of attack profile, $St = 0.4$, $\alpha_{max} = 35°$

angle of attack achieved over one period, T calculated at $R_{0.7}$:

$$\alpha_{max} = 0 \rightarrow T\{\arctan(\frac{R_{0.7}\phi_o\omega\cos(\omega t)}{U}) - \theta_o \sin(\omega t + \frac{\pi}{2})\} \tag{2.8}$$

Figure 2-2 shows an example of an angle of attack solution for different spanwise locations. This particular profile is for $St = 0.4$ with a maximum angle of attack of 35°. In this case, β is large enough that subtracting θ still gives a smooth, sinusoidal angle of attack profile. In some cases, where θ becomes larger to achieve low maximum angles of attack, an inflection point develops. An example of this will be shown in a later section.

2.2 Test Matrix Variables

In 2-D tests the heave/chord ratio is used to non-dimensionalize the heave amplitude. For our 3-D tests, we decided to keep the same convention to non-dimensionalize the roll amplitude using the heave amplitude determined at the 0.7 span. We therefore

define $h_{0.7}$ as:

$$h_{0.7} = R_{0.7}\phi \tag{2.9}$$

where $R_{0.7}$ is the distance in meters from the center of rotation to the 0.7 span, and ϕ_o is the roll amplitude. Although defined in the Introduction, we will review and clarify our particular definition of the Strouhal number for the 3-D rolling and pitching foil:

$$St = \frac{2h_{0.7}f}{U} \tag{2.10}$$

where $h_{0.7}$ is the heave amplitude at $R_{0.7}$, f is the frequency in Hz, and U is the velocity in meters/second. We chose the $2h_{0.7}$ as an estimate of the width of the foil wake.

We now have defined the three non-dimensional parameters to uniquely describe the input variables:

- Heave amplitude at 0.7 span, $h_{0.7}/c$
- Strouhal number, $St = 2h_{0.7}f/U$
- Maximum angle of attack, α_{max}

Just like in the 2-D case of Read [6] and Haugsdal [5], we can see from equation 2.8 that the input variables for each experiment are:

- Frequency, ω
- Roll Amplitude, ϕ_o
- Pitch Amplitude, θ_o
- Inflow speed, U
- Time, t

Non-Dimensional Parameter	Controller Input
0.7 span heave/chord ratio, $h_{0.7}/c$	roll amplitude, ϕ_o
Strouhal Number, St	frequency, ω and inflow speed, U
Maximum AoA, α_{max}	pitch amplitude, ϕ_o

Table 2.1: Non-dimensional and dimensional input variables

However, if we want to present data in non-dimensional form we have to determine the variables for each experiment from the non-dimensional parameters of the test matrix. The test matrices for propulsion and maneuvering tests were chosen by first determining the heave/chord ratio for testing. $h_{0.7}/c$ is the heave amplitude at the 0.7 span non-dimensionalized by the average chord. The heave amplitude at the 0.7 span is the roll amplitude multiplied by 0.7 span in meters (half-arc length). Thus the roll amplitude, ϕ_o is determined and fixed. Next, we choose the Strouhal number and find the inflow speed and flapping frequency to achieve the desired Strouhal number. We knew to reach higher Strouhal numbers we would need to have a low inflow speed since the frequency of flapping is mechanically limited. We also want U to be constant for a set of tests, so really we solve for input frequency. This leaves us with finding the pitch amplitude, θ_o that gives us the desired maximum angle of attack. Microsoft Excel was used to solve for θ_o in Equation 2.8 using the Goal Seek function. The non-dimensional parameters and dimensional inputs are summarized in Table 2.1.

2.3 Resulting Angle of Attack Profiles

Extensive discussion of angle of attack solutions is included by Read [6]. One important note is that there are two solutions for pitch amplitude, one thrust producing and the other drag producing. Also, beyond a certain Strouhal number, low angles of attack cannot be achieved. In other words, there is a minimum value of the maximum angle of attack that will produce thrust for a given set of parameters. Looking at equation 2.8, we see that as Strouhal number (directly related to ω) increases, the

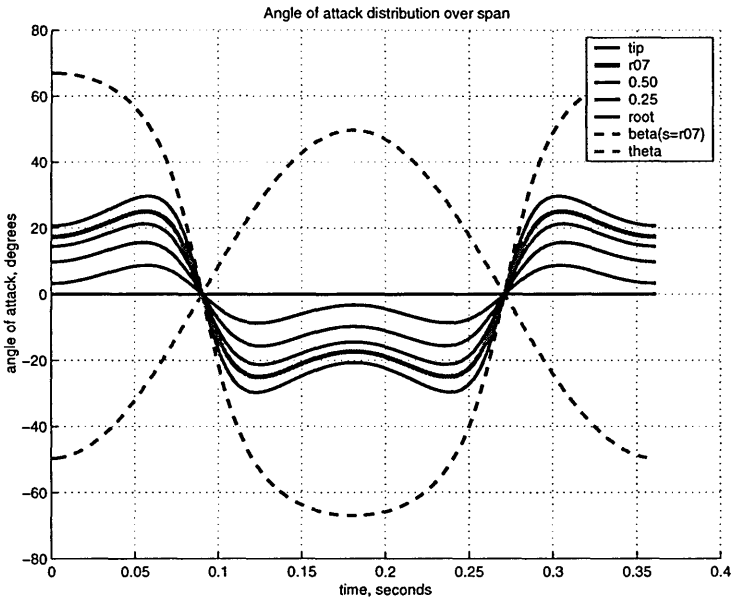

Figure 2-3: Sample of inflection points in angle of attack profile

positive part of the equation gets large. Therefore to keep α small the pitch amplitude θ_o has to become large too. The sum of (β) and (θ) does not maintain a smooth, sinusoidal profile for high Strouhal numbers at low α_{max}. Mechanically large pitch amplitudes at high frequencies are not possible.

Haugsdal [5] found that the cosine angle of attack profile was the best for producing thrust. For our foil parameters, simple harmonics produced a nearly sinusoidal angle of attack. However, as was hinted at the end of the last section, as Strouhal number increases it becomes more difficult to produce thrust at relatively low angles of attack. This is because the angle of attack profile starts to have inflection points.

We see an example of such behavior in Figure 2-3. This particular case is for a Strouhal number of 0.75 and maximum α_{max} of 25° with $h_{0.7}/c = 1.5$. The inflection becomes larger as we solve for smaller angles of attack. Haugsdal [5] and Anderson [4] showed that multiple peaks in the angle of attack profile like we see here produce drag vortices in addition to the thrust vortices. Therefore, the thrust decreases as the angle of attack decreases and eventually the foil is producing only drag and no thrust.

Chapter 3

Experimental Setup and Methods

3.1 General Description

The flapping foil actuator module was designed for use on an autonomous underwater vehicle (AUV), and was also used in this project to measure forces and torques on a flapping foil. The module was attached to a six-axis dynamometer and installed in the MIT Water Tunnel. Section 3.1.5 addresses the accuracy of measured force and torque signals due to the design of the module and installation. The module actuator produces two-axis motion with two degrees of freedom, rolling and pitching. The two axes cross, so that the motion produced was an elongated, flat figure-eight.

All experiments were conducted in the MIT Department of Ocean Engineering Marine Hydrodynamics Laboratory (MHL). The laboratory facility contains a test section of a two-story closed loop water tunnel. Fluid velocity is controlled by a variable speed impeller. Adjacent to the control panel are two PCs. In our case one PC, called Cornerflow, was used to communicate with the foil module for motion control. The other PC, Water-tunnel, ran the data acquisition program TestPoint for the experiments measuring forces with the dynomometer. Cornerflow runs the Dantec software used by the LDV system. Another separate computer was used to run the LaVision software used by the PIV system.

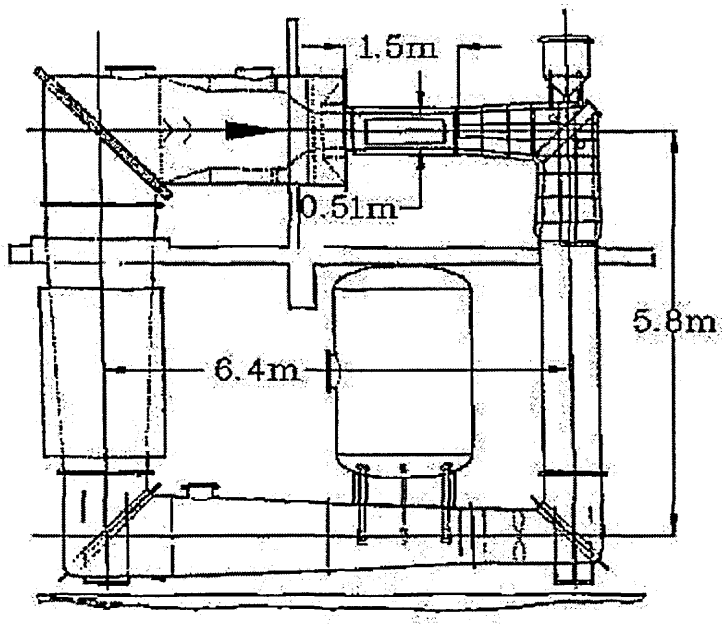

Figure 3-1: MHL Water Tunnel

3.1.1 The Water Tunnel and Module Housing

This section describes the Water Tunnel facility in greater detail, and describes how the flapping foil actuator model was installed for force measurements. A module housing was constructed to surround the module box and attach to the dynamometer to measure forces. A fairing was also constructed to protect the module from adverse hydrodynamic forces resulting from interaction of the box's seal and the inflow.

The planform of the entire tunnel is about 6 meters, and the test section is about 0.50 meters square by 1.5 meters in length. Figure 3-1 shows a schematic of the tunnel [14]. The storage tank on the first level is used to fill the tunnel. An air vent valve was employed in the dynomometer window to ensure the tunnel was completely full surrounding the foil module before every testing session. The impeller is located in the lower horizontal section of the tunnel which is driven by a large DC motor. The impeller speed is adjusted manually using dials which adjust the field current via a variable resistor on the control panel. Free stream turbulence intensity as a function

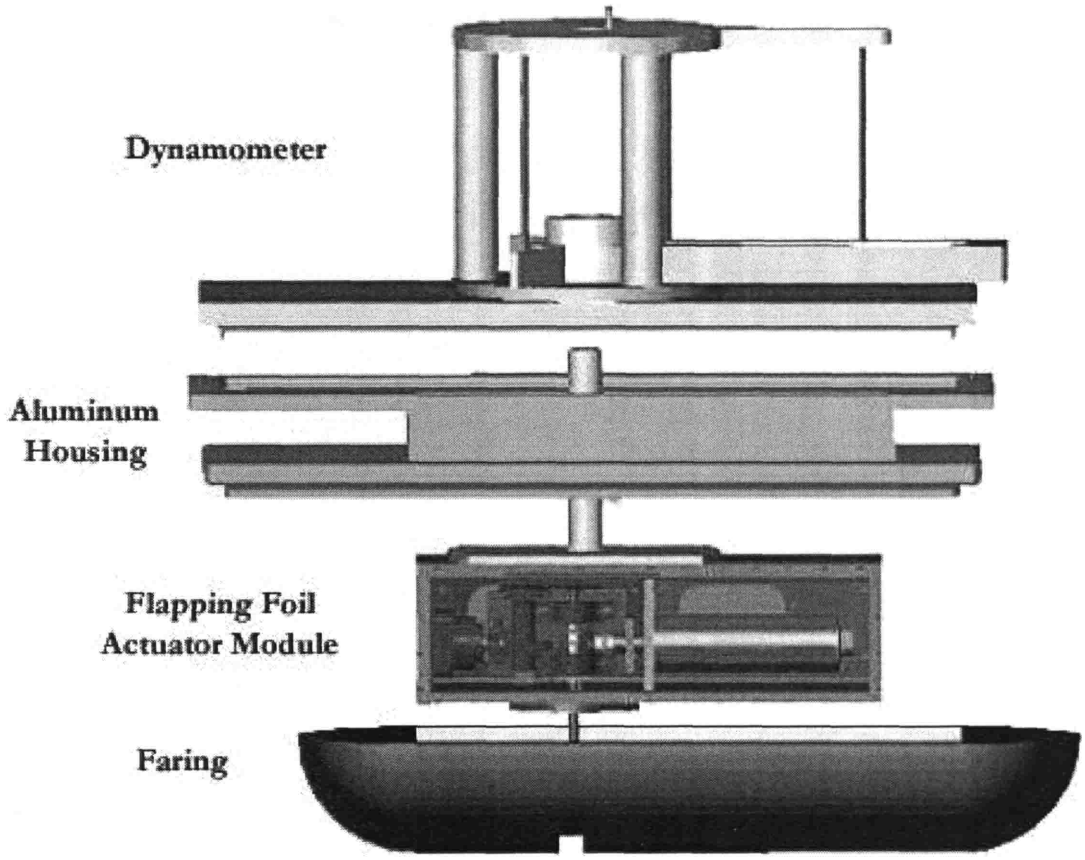

Figure 3-2: Module Housing Assembly

of tunnel speed was measured previously in an empty tunnel by Lurie [15] using hot wire anemometry. These measurements showed a free stream turbulence intensity of 1%.

In the test section, there were four removable windows; one on each side. Our experiment was installed from the top. The six-axis dynamometer used to measure forces was attached to a window. A three-piece aluminum housing was constructed to fit between the top of the tunnel test section and the dynomometer to surround the foil module. The dynamometer window was held to the aluminum housing with 12 C clamps. Figure 3-2 shows the disassembled sections. The dynamometer held the foil module via a shaft attached to the module box. There was only approximately 1 cm distance between the dynamometer window and the top of the module box when

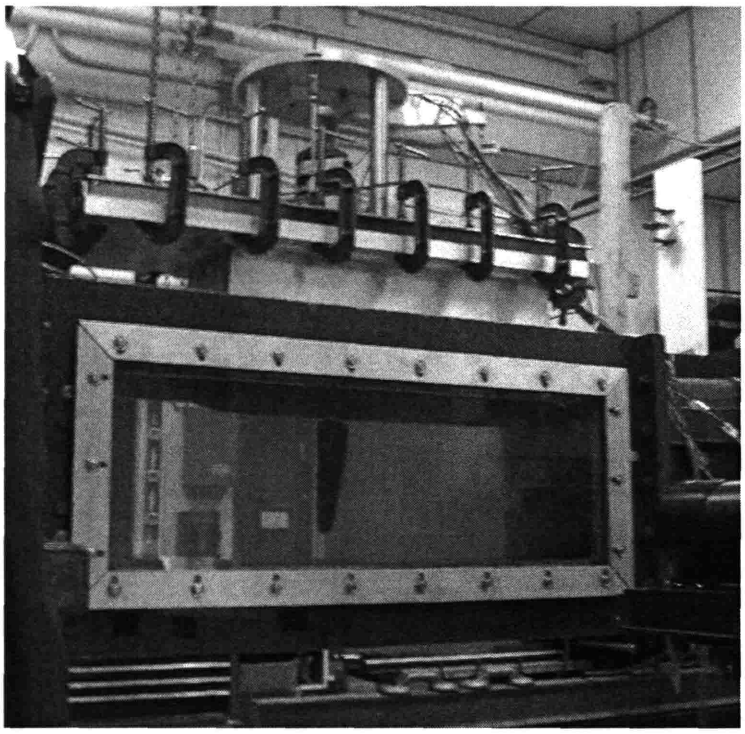

Figure 3-3: Module Housing Assembly Installed in the Water Tunnel

assembled.

A fairing was constructed using wood and waterproof sealant to attach to the aluminum housing from inside the test section. The fairing was constructed to minimize flow interaction with the foil module and the module's waterproof seal, named the bellows. The bellows design was the major obstacle in retrofitting the module box to the water tunnel for experiments. This large rubber seal protruded into the test section, making the fairing essential. The fairing caused problems in the beginning because it would touch the box and corrupt the force signal, so it was modified several times to ensure that it was not touching the module or bellows.

Figure 3-3 shows a picture of the complete assembly inside the test section of the water tunnel. When assembled, the module fits inside the aluminum housing. Therefore, the bottom of the box was on the same plane as the top of the tunnel. Two Impulse connectors were used on the module, one for power and one for communica-

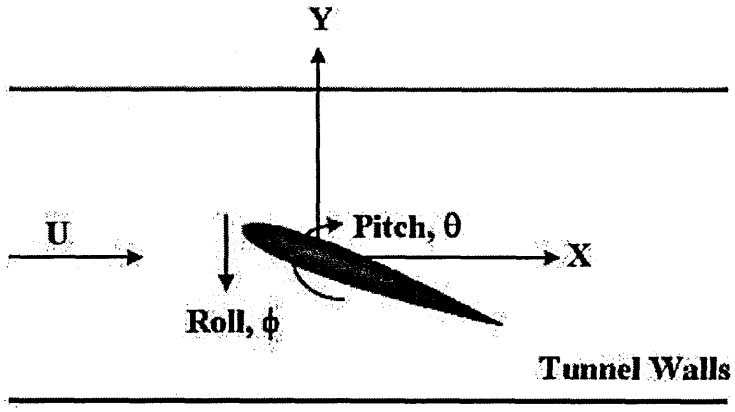

Figure 3-4: Top View of a cross-section of the Foil in the Tunnel

tions. The Impulse connectors attached to the flange piece of the aluminum housing connected the foil module inside the tunnel to outside the test section. The cables were tied such that they would not hang down into the flow, but wound carefully so that they would not put any forces on the foil module.

Figure 3-4 shows a sketch of a cross-section of the foil inside the tunnel, from a top view. The X force (thrust) is measured in the downstream direction. The Y force (lift) is measured across the wake, or out of the tunnel side window. The roll motion is in line with the Y force. The pitch angle is referenced from the X axis.

3.1.2 The Flapping Foil Actuator Module Construction

This section describes the construction of the flapping foil actuator module. A somewhat detailed description of the actuator design, waterproof seal, and foil is included. We also describe the shortcomings of the design, and the retrofit to add a torque sensor after its initial construction.

The flapping foil module box was constructed from 3/4 inch thick lexan. Figure 3-5 shows a mechanical drawing of the inside of the module. It is about 8 1/2 inch square by 2 feet long rectangular box with a O-ring-sealed lid and slot for the protruding foil shaft. The foil itself is mounted via a taper pin to the end of the foils shaft. The shaft is supported by two radial ball bearings mounted into pillow blocks and has an

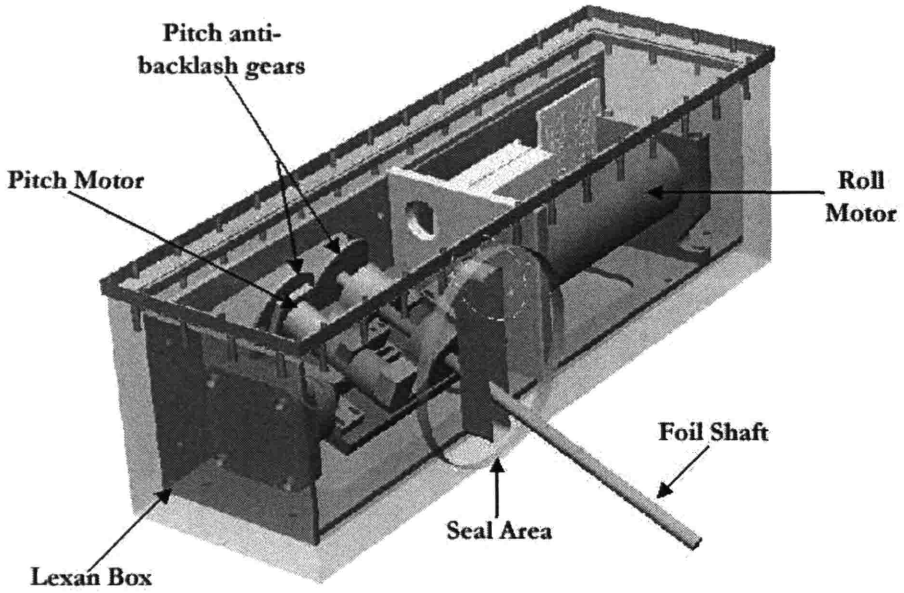

Figure 3-5: Solid model drawing of the flapping foil actuator, Licht and Polidoro (2002).

anti-backlash gear attached to the end. A DC brush motor and anti-backlash gears actuate the pitch motion. The motor and bearings are mounted to an aluminum plate. The aluminum plate is supported by a piece connecting the plate to a double-roller taper bearing on one side, and by a coupling to the roll motor shaft on the other side. The roll motion is actuated by a DC brush motor rotating the aluminum plate. The pitch motor had a 3 stage gear reduction, resulting in a 1.5 degree maximum backlash, and the roll motor has a 1 degree maximum backlash.

The module is divided into two compartments; one for the roll motor and electronics, the other for the rotating plate. The compartments are separated by a bulkhead. The roll motor bolts onto the bulkhead. A hole in the separating plate allows the roll motor shaft to extend through to the aluminum plate compartment. The coupling between the two consists of a sleeve with a matching machined keyway, a square drive extension piece, the miniature torque sensor, and an aluminum piece to attach the square end of the sensor to the aluminum plate. This retrofit had set-screws and a taper pin that would vibrate loose after many tests, so the motion was continually

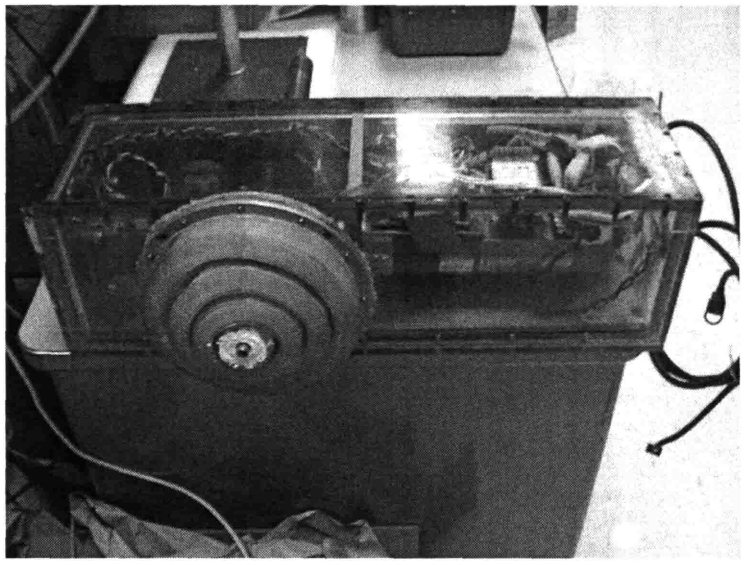

Figure 3-6: Flapping Foil Actuator Box with Bellows Seal

monitored to ensure that it was smooth and not jerky. The torque sensor was not part of the original design; therefore the space requirement forced the choice of a physically small sensor that had square ends.

The slot in the lexan box for the foil shaft was sealed with a large, corrugated, rubber piece. Figure 3-6 shows a picture of the bellows seal on the box. The seal design required many iterations to optimize its shape and compliance. The bellows were made using a mold designed by Victor Polidoro, first carefully laying triangular strips of Kevlar into all of the spaces and then pouring the mixture into the mold. A cylinder was placed in the center for mold alignment and to take the place of the shaft seal as the mold sets. The shaft seal was a small cylinder with two O-rings that were glued into the bellows with waterproof adhesive. The bellows attached to the module box using two aluminum rings. The module box had a round lexan piece with an O-ring seal that seals with one aluminum ring face. The bellows is squeezed between the two aluminum rings, which have screw holes to finally secure the bellows assembly to the module box. The first bellows lasted for about a month's worth of tests, then a crack was discovered in the rubber. The slow leak did not harm any of the electronics. We did not use the additive to make the bellows compliant the

second time, and it lasted much longer but also eventually tore.

The foil used for all experiments was of a triangular shape, with a linearly tapered trailing edge and straight leading edge. It had an approximate NACA 0015 section, average chord 5.5 cm and span 24.3 cm. The maximum chord was 7.5 cm at the root and tapered to 3.5 cm at the rounded tip. It was constructed using a stainless steel triangular skeleton and polyurethane plastic in a mold designed by Karl McLetchie. A 1/4 inch diameter stainless rod welded to the skeleton was inserted in the mold at the approximate 1/4 chord position. The foil was spray painted black to absorb laser light for safety reasons and sanded for a smooth finish.

3.1.3 Actuator Module Electronics and Communication

This section describes the controller and program used in the actuator module to achieve our desired motion. We were able to record the position, torque, velocity, and error in position for both axis. Although we used two computers, we were also able to sync the force data with the position data. Finally we include a control and data collection diagram.

Control of the module was accomplished using a Galil DMC-1425 two-axis, PID motion control card installed in the module. The DMC-1425 communicated with Cornerflow via the Ethernet. Control code was written in the two-letter command code created by Galil. An internal editor allows programs to be quickly entered and downloaded. We used their WSDK support software for tuning, downloading programs through the internal editor, and for the communication terminal. The two letter commands can alternatively be entered in the terminal and executed immediately.

The control code used roll amplitude, pitch amplitude, allowable encoder error on both axis, period, pitch bias angle, and number of cycles as inputs. Since the motion was sinusoidal and the pitch motion relative to the roll motion is out of phase 90 degrees, we were able to take advantage of the DMC-1425 vector mode using circular interpolation. The DMC-1425 allows a long 2-D path consisting of arc segments to be prescribed. Motion along the path is continuous at the chosen vector speed. The DMC-1425 performs the computations of circular interpolation. We were able to then

prescribe a 3-D path since it allows a pair of two axes to be selected for coordinated motion consisting of circular segments.

An amplifier controlled power and current to the motors. Both DC motors had optical encoders. A conversion factor of encoder counts per degree was found. The conversion factor was validated by recording the actual position, in encoder counts, for every run. We could then apply the conversion factor and ensure this agreed with the commanded amplitudes.

We were able to record the actual position, error in position, velocity, commanded torque, and torque from sensor for both axes using a C++ interface code running from Cornerflow that samples the buffer at a rate of about 1 microsecond and writes all values to an ASCII text file. The circle program was executed in a line in the C++ code. This way the second programming thread could be used to set a digital output on the motion control card high going in the positive direction or low when travelling in the negative direction when the foil crossed the zero axis for the roll. This pulse signal was sent through two lines of the impulse connector to the data acquisition breakout board so that we could sync the forces and position of the foil. It was also used to collect phase-average data with the LDV and PIV systems. The final two lines of the impulse connector were used for a simple flood alarm.

Figure 3-7 shows a control and data collection diagram. The module required +24 V power, which was supplied by a 40V, 166 amp maximum DC power supply. The DC Converter then distributed power to the DMC-1425 and the two motors. The force sensors are powered by the signal conditioner. A 25 lb maximum force sensor was chosen for the X direction, and 50 lb maximum force sensor for the Y for all tests except the static bias tests, where smaller sensors were used. The flood alarm was externally powered by a smaller power supply, since it only required +12 V.

3.1.4 Data Collection and Processing

This section describes the purpose of both computers in data collecting, and how the signals were saved and processed using MATLAB. A diagram of the system is presented. We also describe the procedure for executing a typical run, and show time

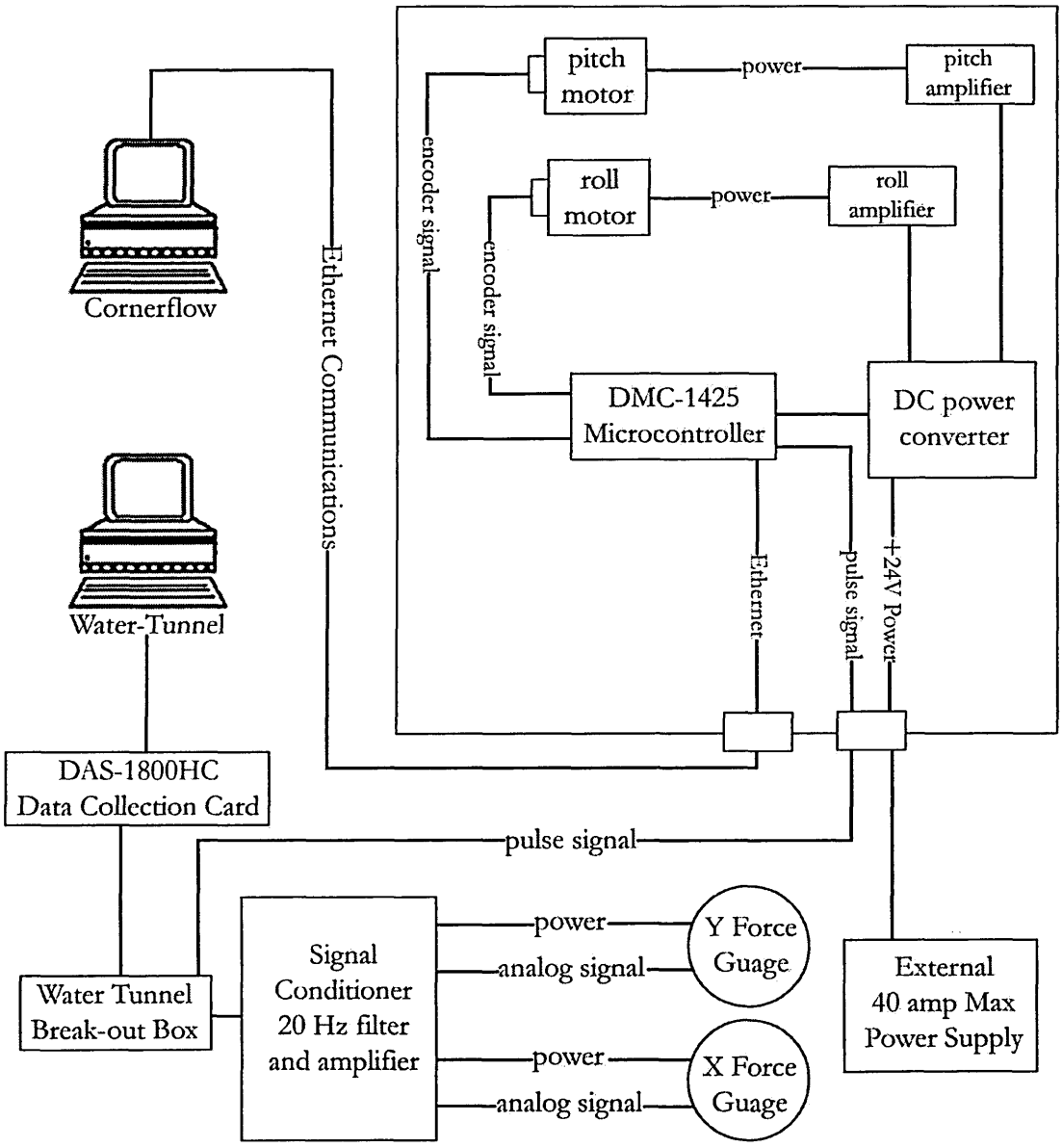

Figure 3-7: Control and Data Collection

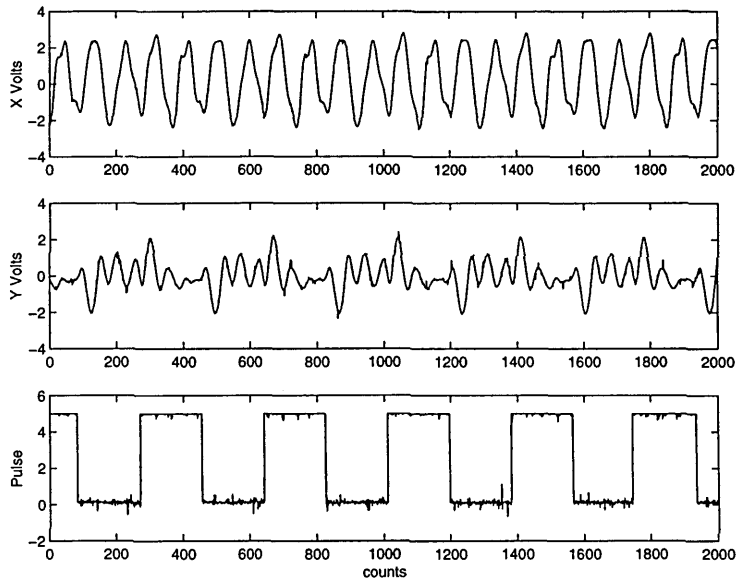

Figure 3-8: Raw Data, Forces

traces for a typical run.

Data collection for force measurements was accomplished using a Keithley MetraByte DAS-1800HC Series Function call driver and the program TestPoint on the computer called Water-tunnel. The card collected and recorded the three important data signals simultaneously: the pulse signal (which tells us the foil position and makes synchronization with the position data possible), Y force, and X force. The X and Y signals from the force gauges on the dynamometer pass through a signal conditioner which amplifies the signal to 0 to +5V and filters at 20 Hz cut-off. The signals then go through the water-tunnel break-out box and finally to Water-Tunnel's data collection card. Both the raw data and the average were saved. The sampling rate was 1000 Hz for all runs.

An example of the recorded raw force data for a typical propulsion run is shown in Figure 3-8. The data is unprocessed, so the vertical scale is in Volts. The Y force gauge is twice as large as the X force gauge. For each run, 50 periods of motion were recorded and then averaged. Figure 3-9 shows an example of the recorded encoder feedback and torque signal. The two data sets are separate because they

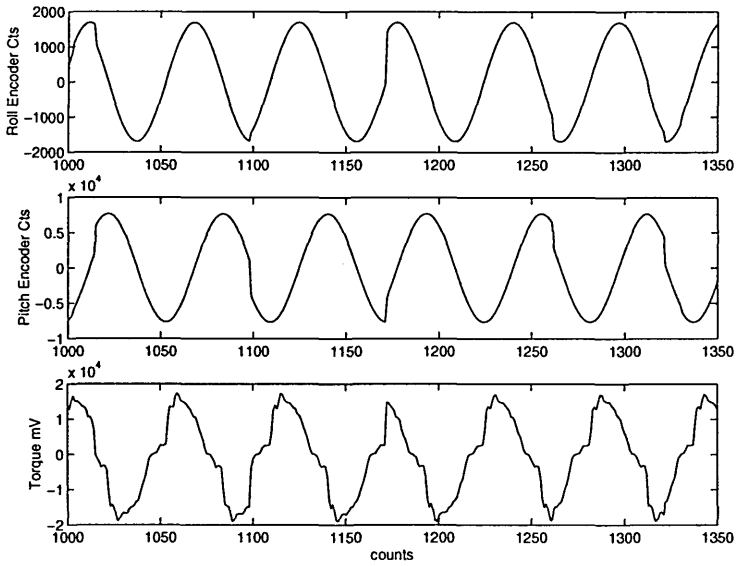

Figure 3-9: Raw Data, Position

were recorded on two different computers. They also have different sampling rates. Once both signals are converted to time traces in seconds instead of counts, the pulse signal then links them in time since it is set to change state for a zero crossing in the roll. The typical testing procedure started by entering the parameters for the run in the Galil terminal, starting the code by running the C++ program so that the position data would be saved, then starting the TestPoint program to record forces. Once the 50 cycles were taken, the force and position files were both saved.

We saw some slight discontinuities in the position (encoder feedback) time traces. These discontinuities in the position data could be due to numerous things. Because the C++ program communicating with the Galil card to record encoder counts was not time stamped, we would not know if some data points were missing. The data transmission between the Galil card and Cornerflow could be interrupted. The C++ program could have slightly irregular sampling. It could possibly be due to mechanical backlash, but it seems more likely to us that a data point or two was skipped occasionally due to communication interrupts since some skips are larger than the backlash rating.

The code we used would slowly bring the foil to its maximum commanded roll position, then instantaneously begin. This was not ideal, since the torque on the pitch motor would not allow for high pitch motion at high frequencies. We overcame this difficulty somewhat by setting the error limits for the pitch axis high, so that it would not quit the program because of the first instantaneous jump it had to make. The foil was centered by turning the pitch axis while at a constant tunnel impeller speed until the lift force was as close to zero as possible.

Data processing was accomplished using the program MATLAB. Scripts were written to read, parse, and plot the data, as well as perform the necessary computations. Data were not filtered for the purpose of calculation. The data were zeroed by the initial offset recorded before the motion of the foil began. Both Read [6] and Haugsdal [5] describe why this is important, especially concerning the X or thrust force. Read explains that zeroing the data before any motion starts ensures that the drag on the foil will be included in the thrust calculation, i.e. only the net force will be measured. Zeroing the data with the portion of the signal at flow speed, but with no motion, excludes the foil drag and leads to an artificially high value of mean thrust.

3.1.5 Force and Torque Measurement Accuracy

During preliminary experiments, we noticed frequencies much higher than the driving frequency appearing in the force measurements. We believed these frequencies were due to vibrations of the module in the tunnel. First, we ran a spectrum analysis of runs with the foil module sitting in a full tunnel, with no electronics on, and observed a frequency spike at 30 Hz on the X force sensor. We therefore decided to use a 20 Hz analog filter for all runs thereafter for both the X and Y force sensors.

After all experiments were completed, we did a spectrum analysis of runs from the starting maneuvers. These runs were an impulsive start of the foil, and we observed frequencies three times or more above the driving frequency. Figure 3-10 shows the results for one representative case of a impulsive start of the foil at a driving frequency of 2.5 Hz. We observe a large spike between 10 and 13 Hz measured by the X force sensor. The lift signal does not show clear peaks, but does show frequency components

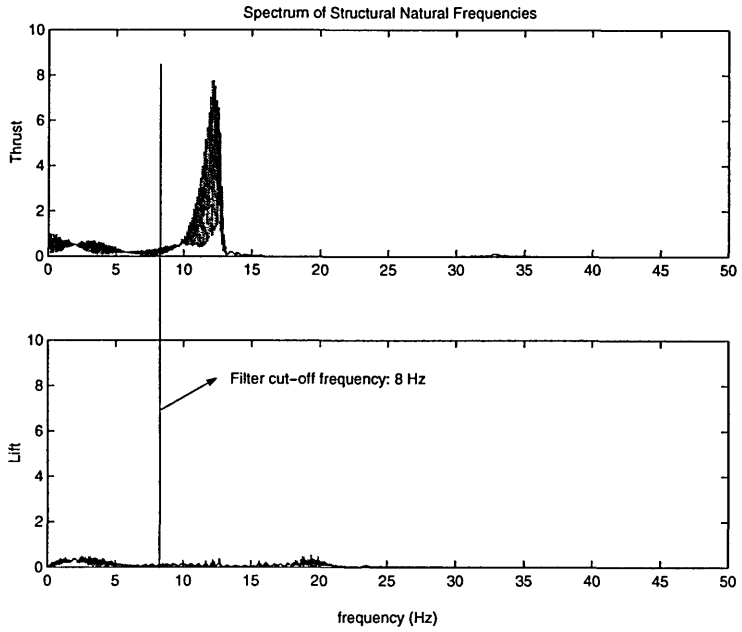

Figure 3-10: Spectrum Analysis of the Assembly (Impulsive Start, driving frequency 2.5 Hz)

around 20 Hz. The signals presented in the appendix will be filtered to try to exclude frequency components believed to be due to structural vibrations, i.e. frequencies above 8 Hz for both axes. This is to see unsteady hydrodynamic forces, with the understanding that structural vibrations would be present were the foil used as a propulsor on an underwater vehicle.

Next, we examined the magnitude of the forces and torques measured for runs performed without the foil attached, but actuating the foil module at the same parameters. We believe the measured forces are due to the inertia of the moving parts and added mass of the box, if it is indeed vibrating. The torque measurement taken with and without the foil were almost exactly the same, making it impossible to calculate a meaningful value of efficiency. The bellows design more than likely causes this difficulty, since it seems to be absorbing almost all of the input power provided by the roll motor.

Figure 3-11 shows a representative run of comparisons between force measurements with the foil on and actuated, then with the foil off and actuated (both in

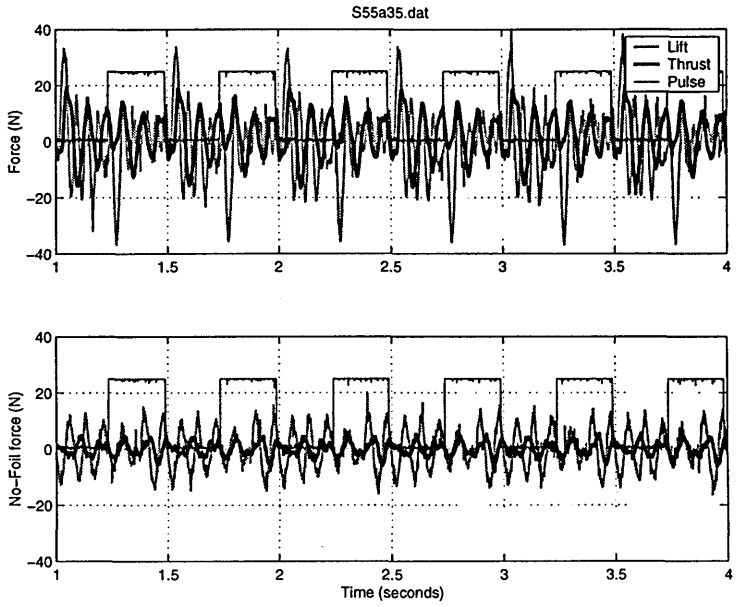

Figure 3-11: Comparison of Forces with and without the Foil (unfiltered), Period 2 Hz and Roll Amplitude 12 degrees

water). The pulse signal shows that the two data sets are in sync in foil position. This is for a run with a frequency of 2 Hz and maximum roll amplitude of 12 degrees, which converts to a Strouhal number of 0.55. This particular run is average, since propulsion tests were conducted with frequencies between 1 and 3 Hz. We observed that as the frequency and amplitude of motion increase or decrease, the no-foil comparison increases or decreases proportionately.

The no-foil signal averages almost to zero, so the plots of mean forces presented in the results sections are valid with an error of 2% or less calculated by comparing the mean no-foil force to the foil-on mean force. The error in the average thrust coefficients was calculated for many runs to check the 2% error limit.

We concluded that the time traces are so closely linked that it is too difficult to determine the time trace due to hydrodynamic forces alone. In other words, the measured dynamic forces have a portion of the signal due to the mechanical properties of the actuator, but the mean values of F_X and F_Y are different, so this is valid data. If one wants to predict dynamic forces for another actuator, this will be an obstacle

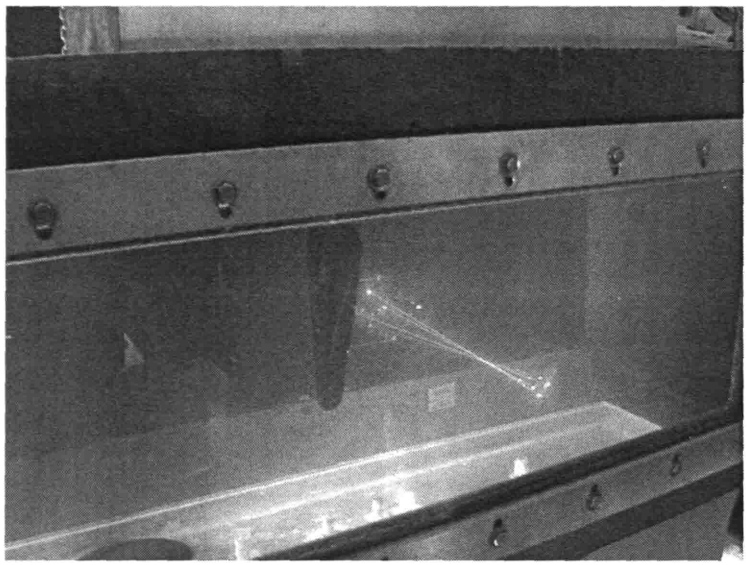

Figure 3-12: Picture of LDV Laser Beams Crossing to Measure Velocity in the Wake

since a different actuator will have different mechanical properties. However, since the average of the no-foil forces are very close to zero, the average force measurements will still provide a road-map in understanding the forces produced by a given three-dimensional flapping motion to be employed in an AUV controls code.

3.1.6 Laser Doppler Velocimetry

The LDV system was used to gather mean velocity at points the wake at different spanwise locations. Another experiment was done across the wake at the 0.7 span, but instead used the pulse signal to do a phase average of the velocity. A 3-D plot of the wake velocity as a function of foil position was then constructed.

Figure 3-12 shows the laser beams crossing at a point in the foil wake to measure the velocity. The LDV laser used is mounted on a traverse, which can be positioned to a resolution of better than 0.01 mm in the x, y and z directions. The laser obtains velocities by shooting two beams, green and blue, to form a fringe pattern. The spacing of the fringe pattern is known and therefore the velocity is calculated by measuring the difference in time it takes a particle to travel between the fringes.

Mean axial and vertical velocities as well as their standard deviations were collected by the laser system and processed using Dantec's FVA flow software. The laser system and its operation is described in [16] and [17]. The laser was calibrated by Kimball [18] using a spinning disk method capable of calibrating both the streamwise and vertical velocity components to better than 0.5% of reading.

3.1.7 Digital Particle Imaging Velocimetry

Unlike other particle methods, DPIV allows the measurement of an entire instantaneous 2-D or 3-D velocity particle field. In general, DPIV tracks groups or patterns of particles using digital FFT and cross-correlation routines. These routines are described and analyzed by Willert and Gharib [20] as well as Adrian [21]. DPIV uses a laser beam focused and then fanned to form a thin 2-D sheet of light to illuminate a sheet of particles and takes a picture of the particle field. A second pulse of the laser illuminates the same sheet at a known time afterward and takes another picture (approximately 1 ms). The system used in this setup is from LaVision, Inc. The camera is a Megaplus ES4.0 2k x 2k CCD camera from Redlake MASD, Inc (formerly the Kodak Megaplus ES4.0). The laser was a 120 mJ/pulse ND:Yag laser from New Wave Research, which is frequency doubled to operate at 532 nm (green) light. The system is capable of acquiring PIV image pairs continuously at 7 Hz or phase synchronized to an external event by a TTL input signal. For the flapping foil a +5 V DC trigger signal was sent to the LaVision computer each time the foil rolled through its midline position. A phase lag was then input into the LaVision software to command when the images should be acquired, allowing phase averaged data to be obtained at 7 different angles in one roll-cycle.

The fluid is seeded with neutrally buoyant fluorescent particles approximately 40 to 70 mm in diameter. The data is saved real-time. For our set-up, the camera was located under the tunnel pointed upwards. Therefore we captured the X-Y velocity plane in the wake at the 0.7 span. The foil is visible in the picture as a reference. The camera was mounted to an support attached to a plate where the laser head was mounted. The plate support for the laser was attached to the LDV traverse so that

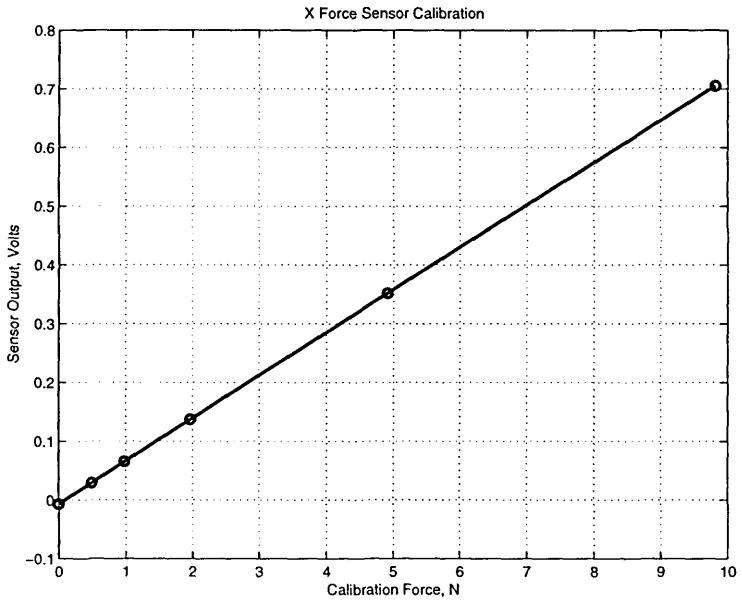

Figure 3-13: Sensor Linearity, X

we could take advantage of the traverse's exact positioning capability.

3.2 Calibration

3.2.1 Sensor Linearity

Both X and Y force sensors for checked for linear behavior. Force sensors were tested using several known weights. The sensors exhibited good linearity, within 1% of the range calibrated. Figure 3-13 and Figure 3-14 show the results of these tests. The actual forces exerted during tests had mean values between 0 and 5 Newtons on the X force sensor for propulsion tests, with peak values between 10 and 25 Newtons. The actual forces exerted on the Y force sensor had mean values up to 9 Newtons in pitch bias tests, with peak values between 10 and 50 Newtons. The sensors were calibrated before a set of tests were conducted. For the pitch bias tests, we also calibrated right after to see if they exhibited any drift. From day to day, as well as before and after tests, the drift was less then 2%. The calibrations were performed by hanging a

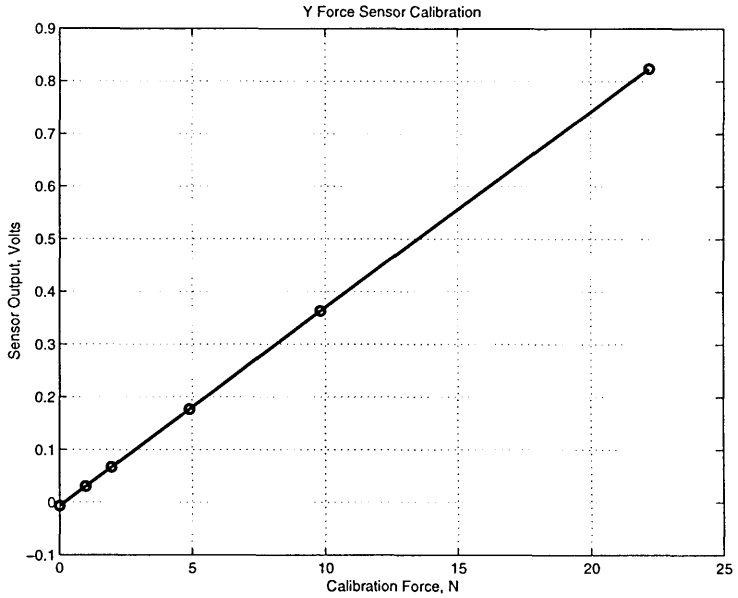

Figure 3-14: Sensor Linearity, Y

known weight from a pulley in line with the foil in either direction, running TestPoint for 10 seconds, and recording the average force. Then the weight was removed, and put back on. We repeated recording the average with one weight several times, then moved on to the next weight. The average value of several runs for each weight was plotted in MATLAB, and then the calibration constants were calculated by finding the slope.

Chapter 4

Propulsion Experiments

The X and Y force data trace and mean value for each run was recorded by TestPoint. The average thrust force is:

$$\overline{F}_x = \frac{1}{T}\int_0^T X(t)dt \tag{4.1}$$

where T is the period of one cycle of the foil motion. The time average of each signal was not calculated over one period, but over 50 periods for a given run. The average lift force $\overline{F}_y$ is calculated in the same way. In propulsion tests, the average lift force was near zero.

Mean force data in this section and following sections are presented in terms of the non-dimensional force coefficient:

$$C = \frac{\overline{F}}{\frac{1}{2}\rho U^2 cs} \tag{4.2}$$

where ρ is the density of water in kg/m^3, c is the average foil chord in meters, and s is the foil span in meters. U is the flow speed in m/s aligned with the global X axis. F is the measured force in Newtons. F is either X or Y, the thrust and lift components. Therefore, C_T would by the thrust coefficient, or X component and C_L would be the lift coefficient, or Y component.

Note that the thrust coefficient could also be defined by the swept area of the foil instead of the projected planform of the foil. The swept area is a function of roll

amplitude, pitch amplitude, and pitch axis location along the chord of the foil. If we approximate it by just the roll amplitude ϕ_o, the the swept area of $R_{0.7}$ is:

$$SA = 2\phi_o({R_{0.7}}^2 + 2R_oR_{0.7}) \tag{4.3}$$

where ϕ_o is the roll amplitude in radians, and R_0 is the distance from the center of rotation to the hub of the foil. The swept area is essentially the area between the arc length of $R_{0.7}$ and the arc length of the hub of the foil.

Using the swept area instead, Equation 4.2 for thrust becomes:

$$C_{T_{SA}} = \frac{F}{\frac{1}{4}\rho\phi({R_{0.7}}^2 + 2R_oR_{0.7})U^2} \tag{4.4}$$

In the following figures, C_T is defined as in Equation 4.2. To convert C_T to $C_{T_{SA}}$, multiply by 0.84 for $h_o/c = 1.0$ and 0.52 for $h_o/c = 1.5$.

4.1 Results for Simple Harmonic Motion

The range of the parameter space for simple harmonic propulsion experiments is:

- Strouhal number, 0.2 or 0.4 to 0.8 (0.05 increment)
- Heave/Chord Ratio $h_{0.7}/c$, 1.00 and 1.50
- Maximum AoA, 15° to 50° (5° increment)

The test matrix is reduced by the fact that some angles of attack cannot be achieved above a certain Strouhal number. The maximum Strouhal number was 0.80 because of lower limitation on the inflow speed, U, and upper limitation on frequency due to mechanical limitations. The maximum roll amplitude was about 14°, or $h_{0.7}/c = 1.72$ because of the tunnel side walls. Propulsion experiments were conducted at a inflow speed of $U = 0.40\ m/s$ for $h_{0.7}/c = 1.0$ tests, and $U = 0.60\ m/s$ for $h_{0.7}/c = 1.5$ tests. The tunnel inflow is slightly more stable at 0.60 m/s, but to achieve the desired Strouhal numbers for the $h_{0.7}/c = 1.0$ tests we had to reduce the inflow speed. This

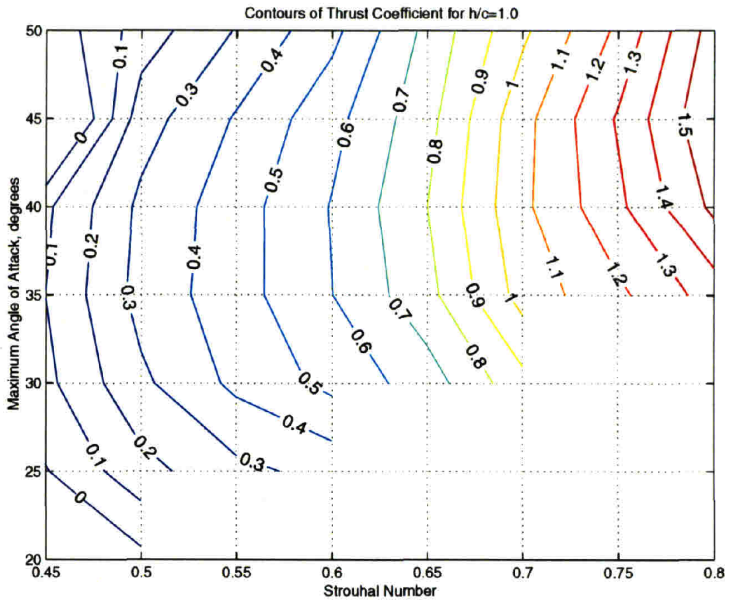

Figure 4-1: Contours of thrust coefficient for $h_{0.7}/c = 1.0$

was measured at all times by the LDV system and monitored so that it was within 0.01 m/s. These speeds corresponds to a Reynolds number of approximately 33,000 and 22,000, respectively, based on average chord of the foil.

Maximum thrust coefficients of 2 were recorded for the highest Strouhal number where measurements were possible. A discussion of the region of high Strouhal number and low angle of attack is included, as well as comparisons with the two-dimensional results.

In Figures 4-1 and 4-2 we show the results of experiments conducted and two different roll amplitudes, $h_{0.7}/c = 1.0$ and $h_{0.7}/c = 1.5$. This corresponds to roll amplitudes of 8 and 12 degrees. Oscillations up to about 3 Hz were possible, giving a maximum Strouhal number of 0.8. Maximum angle of attack varies from 20 degrees to 50 degrees. Contours are calculated from experimental points taken at increments of 0.05 Strouhal number and 5 degrees maximum angle of attack. Two runs were conducted at each point to validate repeatability for $h_{0.7}/c = 1.5$ tests.

In Figure 4-1 we show a maximum thrust coefficient of 1.5 for both 40 and 45 degrees maximum angle of attack at a Strouhal number of 0.8. Thrust coefficient

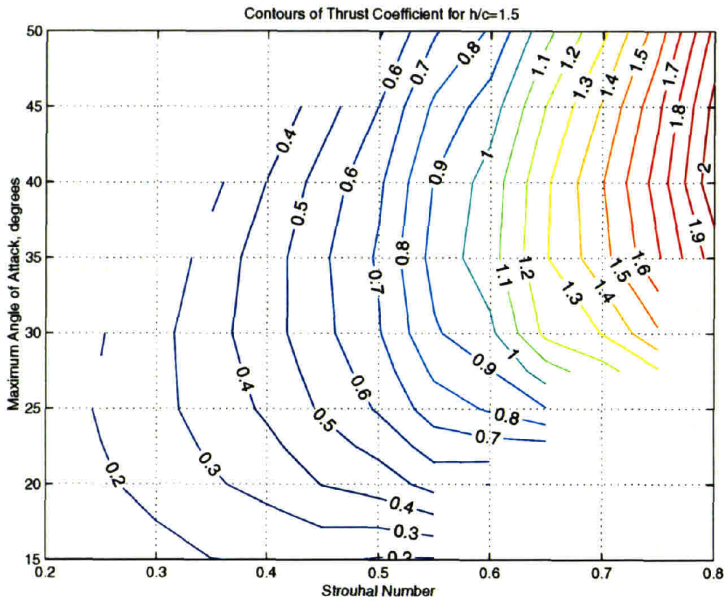

Figure 4-2: Contours of thrust coefficient for $h_{0.7}/c = 1.5$

increases with higher Strouhal number for every case where data were collected. The area where no data was collected exists because a high pitch amplitude is required to preserve a smaller maximum angle of attack at the higher Strouhal numbers. High pitch amplitudes at high frequencies could have sheared our pitch coupling.

The transition from drag to thrust is notable. The lowest contour in the figure is the point at which the average force in the X direction was zero. This contour represents the transition in the wake between thrust producing and drag producing vortex patterns. At relatively low and high maximum angles of attack, transition to thrust does not occur until a calculated Strouhal number of 0.5.

Figure 4-2 shows the results of experiments conducted at $h_{0.7}/c = 1.5$. Oscillations up to 3 Hz were again possible, but the speed was slightly increased to give the same maximum calculated Strouhal number of 0.80. Maximum angle of attack ranged from 15 to 50 degrees. Contours are calculated from experimental points taken at increments of 0.05 Strouhal number and 5 degrees maximum angle of attack.

In Figure 4-2 we show a maximum thrust coefficient of 2.07 at 40 degrees maximum angle of attack and Strouhal number of 0.80. A nearly identical value of 2.03 is

recorded at 45 degrees angle of attack and the same Strouhal number. The Strouhal number and maximum angle of attack match the $h_{0.7}/c = 1$ case for the parameters of highest average thrust. In dimensional form, C_T is 4.8 Newtons, or a little over 1 pound. Unlike the $h_{0.7}/c = 1.0$ case, at relatively low maximum angles of attack transition to thrust occurred around a calculated Strouhal number of 0.2. This result is more in line with the two-dimensional results. A transition to thrust for high maximum angle of attack did not occur until a Strouhal number of around 0.4.

We must be reminded that in both of these figures the Strouhal number, maximum angle of attack, and $h_{0.7}/c$ values are all dependent on our definition of an equivalent heave motion, unlike the two-dimensional case. These parameters are all a function of span for the three-dimensional case. The purpose of the definitions were to make comparisons with two-dimensional data.

The shape of the contours between the three- and two-dimensional case are very similar, with reasonably close numerical values. The highest thrust coefficient measured for the two-dimensional case was 2.17, and here we recorded 2.03. In the two-dimensional case, a transition from thrust back to drag for high Strouhal number and low angle of attack was observed. In these cases, the angle of attack profile had become distorted enough to cause the foil to produce drag. Refer to figure 2-3 to see the example of Strouhal number of 0.7 and maximum α_{max} of 30° with $h_{0.7}/c = 1.5$. Higher-order motions to correct the angle of attack profile greatly helped produce higher values of thrust coefficient [6]. Since the shape of the contours look the same for the three-dimensional case, it seems we could assume that the contours in the lower right hand corners approach zero. Higher order motions could significantly improve the thrust production for those cases.

Unfortunately, since efficiency could not be calculated because the bellows seal absorbed so much power and therefore made our torque measurement inaccurate for calculating hydrodynamic efficiency, we must refer back to the two-dimensional case results. There, generally high hydrodynamic efficiency areas are not paired with good thrust performance. However, large thrust coefficients are attainable with moderate to good efficiency. All heave amplitudes for the two- and three-dimensional cases show

similar thrust performance, but note that swept area thrust coefficients are higher for the lower heave amplitude. Higher thrust is the product of larger motions, but in the two-dimensional case efficiencies are slightly reduced, as might be expected from ideal propeller considerations. Time traces for selected parameter sets are included in Appendix A.

4.2 Results for Pitch Only Motion

A small set of runs was conducted under the conditions of no roll motion ($\phi(t) = 0$) and only pitch. The pitch motion was sinusoidal, consistent with all other tests:

$$\theta(t) = \theta_o \sin(\omega t + \frac{\pi}{2}) \tag{4.5}$$

where θ_o is the pitch amplitude in radians. Therefore, the motion was a quick fluttering of the trailing edge. Mean thrust was recorded from data taken over 50 cycles of pitch motion. Oscillations of up to 5 Hz were possible, with θ_o up to 30° possible up to 3 Hz. Tests were conducted in still water, so we leave them in dimensional form since there is no 'U' to use to non-dimensionalize according to Equation 4.2.

Figure 4-3 shows the results of these tests. We see that the magnitude of the mean forces are very small, less than 5% of the mean forces recorded in propulsion tests. However, those were recorded with an inflow speed and these were in still water. Not being able to non-dimensionalize these forces makes it difficult to compare. But, these small forces seem to indicate that the roll motion is especially important in still water, when a vehicle starts from rest. A large mass of water needs to be accelerated to move the vehicle forward, and the roll motion together with the pitch motion provides that ability. Possibly a foil with non-tapered trailing edge or smaller aspect ratio would provide more thrust. Additionally higher thrust may be produced with a chord-wise flexible foil.

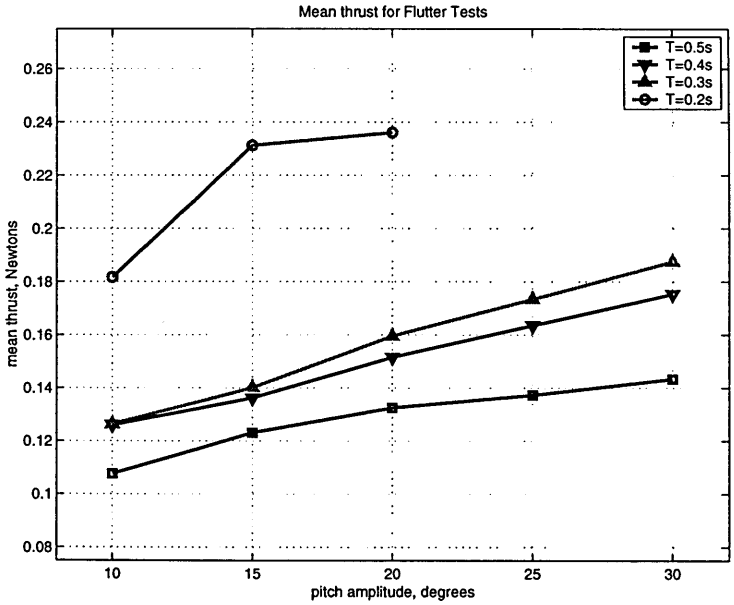

Figure 4-3: Mean Thrust Force for Flutter Tests

Chapter 5

Flapping Foil Maneuvering

There are three important components to locomotion: accelerating/decelerating, maneuvering, and cruising. This is true for fish and for our ideal flapping foil AUV. Maneuvering is important to fish living in complicated habitats such as coral reefs, weed beds, or rocky shores. This form of locomotion requires frequent sharp turns at slow speeds. An AUV with high maneuvering capability would be able to deploy to said habitats where often current AUVs cannot go. In this section, we build on previous experimental results from the two-dimensional case measuring forces produced by commanded motions with added pitch bias. We then examine a half-cycle motion and full-cycle motion of the foil from rest to measure the starting forces and impulse.

5.1 Maneuvering by Pitch Bias

Thus far we have focused on the X force, or thrust force for propulsion. However, we see in Figures 3-8 and 3-11 that the Y force is quite large (about twice as much as the X force) . Therefore, roughly 2/3 of the force produced by the foil was in the form of lift, but since the force was symmetric the mean lift was zero.

By adding some bias to the angle of attack, we hope to take advantage of these large lift forces in maneuvering. This was done by Read [6] and high mean lift forces were recorded. He explains the idea:

> ... the simplest way to do this is to add a static offset, or bias, to the pitch

angle. In propulsion tests the pitch (θ) of the foil was zero at maximum heave (roll (ϕ)), and at the commanded maximum pitch amplitude as the foil crossed zero heave (roll). Thus the mean pitch of the foil was at zero angle of attack to the mean flow. In the maneuvering case, we set the mean pitch position of the foil at some non-zero angle of attack to the mean flow. The foil then oscillates about this new mean pitch, biasing the angle of attack by that many degrees in that direction. For example, a foil programmed to oscillate so that it has a 15° maximum angle of attack would experience ±15° angle of attack. If we add 5° positive bias to the foil, it would pitch up 5° from its initial position and consider that position as zero. Once oscillations began, the foil would see +20 degrees and −10 degrees angle of attack.

Experiments were conducted in the parameter space of good thrust producing runs from the propulsion results. A maximum angle of attack of 40° was tested for Strouhal numbers 0.4 and 0.7 for $h_{0.7}/c = 1.0$ and 1.5, with one additional experiment at $h_{0.7}/c = 0.5$ for a Strouhal number of 0.4. Pitch biases ranged from -10 to 30 in increments of 5°. Negative pitch bias was added to show that the lift forces are symmetric for positive and negative bias. For each set of parameters, the mean lift thrust and lift coefficient over one cycle are given. As with the propulsion experiments, the time average of each signal was not calculated over one period, but over 50 periods for a given run. Each data point was collected at least twice to determine repeatability. Sample time traces are included in Appendix B.

5.1.1 Results

In Figure 5-1 we show the mean lift coefficients for 40° maximum angle of attack. We plot these against one set of tests where the foil was held at a constant angle of attack (no flapping) while the static lift was recorded. Very large values of lift are obtained for the flapping cases. The lift coefficient seems to be very much dependent on the Strouhal number while the effect of $h_{0.7}/c$ appears to be small. However, in both the lower Strouhal number and higher Strouhal number comparisons, the runs with the lowest $h_{0.7}/c$ value had slightly higher mean lift coefficients.

The highest mean lift occurred at a pitch bias angle of 30°. For these parameters, the angle of attack over one cycle will have a minimum of 10° and a maximum of

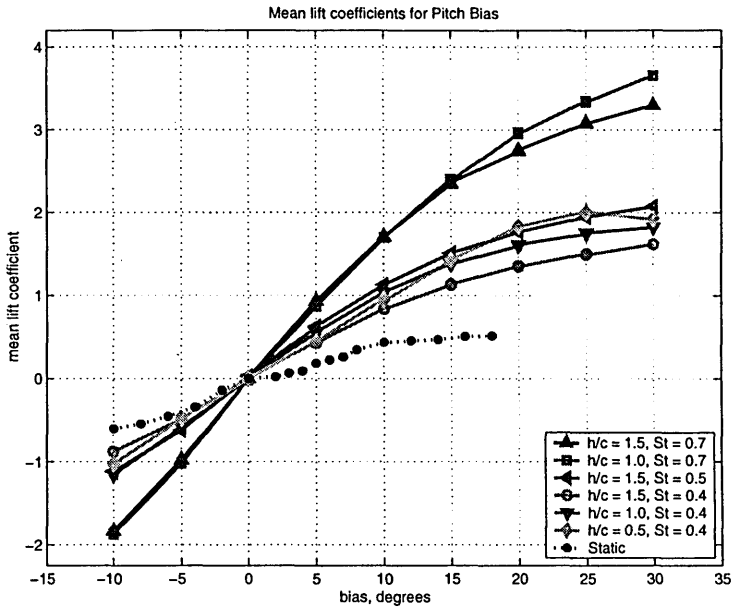

Figure 5-1: Mean lift coefficients for Bias Tests

70°. The steady stall angle for this foil appears to be about 15°, with a maximum lift coefficient of 0.55. Comparison with a NACA 63-018 and 63-012 at a Reynolds number of 5.8 x 10^6 experimental results are available in Hoerner's book, *Fluid Dynamic Lift* [22]. There, a maximum $C_L = 1.4$ with a stall angle of 13° is shown. However, there are key differences between this foil and our foil. First, since this is a two-dimensional result, we can approximately correct for 3-D effects using the results of Prandtl for an elliptically loaded foil described in [23] :

$$C_{L3D} = \frac{C_{L2D}}{1 + \frac{2}{AR}} \tag{5.1}$$

where AR is the aspect ratio s/c. However, applying this formula gives a 3-D estimated C_L of 0.96. This equation is valid provided the aspect ratio is high enough, and ours may be low enough to be questionable. Additionally it is doubtful that our loading is elliptical. Kerwin [23] also cautions that the Prandtl approximation always over-predicts C_L. Second, this foil has a 6% camber while ours has no camber, so without camber we expect slightly less lift. Third, we also have a gap between the

hub of the foil and the faring. The stall angle we measured also does not quite agree with Hoerner since it levels out after 10° to our final testing point at 18°. In any case, the flapping cases are operating well above the static stall angle. Dynamic stall is therefore taking place over the cycle.

Anderson [4] includes a review of dynamic stall research. She summarizes a description of the dynamic stall process from Reynolds and Carr [24]:

> As the angle of attack increases past the steady stall angle, the flow around the foil remains thin and inviscid. The boundary layer on the suction side of the foil begins to show signs of flow reversal, beginning at the trailing edge and progressing towards the leading edge. Then, when a critical angle is reached, the flow separates, the boundary layer detaches and a very strong vortical flow develops. A vortex forms near the leading edge of the foil, grows and moves along the foil surface, significantly affecting the performance of the foil.

McAlister, Carr, and McCroskey [25] describe an important way that dynamic stall differs from steady stall. Anderson summarizes:

> In dynamic stall, the dividing streamline from the point of zero shear into the wake encloses a narrow boundary-layer-like zone of reversed flow. By comparison, for static stall, the point of separation coincides with the point of zero shear. The severity of dynamic stall depends on when in the foil oscillation cycle the stall occurs. The kinematics of the foil govern the dynamic stall vortex (DSV) development, reattachment and convection processes.

McAlister *et. al* [25] found in their experiments that increasing the reduced frequency postponed stall to progressively higher angles of attack. Our results agree with this trend. In our data it appears the dynamic stall angle is higher for larger Strouhal number. In fact it appears to be well above 30° for $St = 0.7$, our limit of testing. Anderson remarked that the phenomenon of dynamic stall presents us with some interesting possibilities in flapping foil propulsion. She notes that the lift enhancement is certainly beneficial, and finally that dynamic stall can either hinder or improve thrust an efficiency depending on the position of the DSV [4].

In observing these and the following data, we must remember that we ran the tunnel at a constant inflow speed. Read [6] makes the point that using a foil to

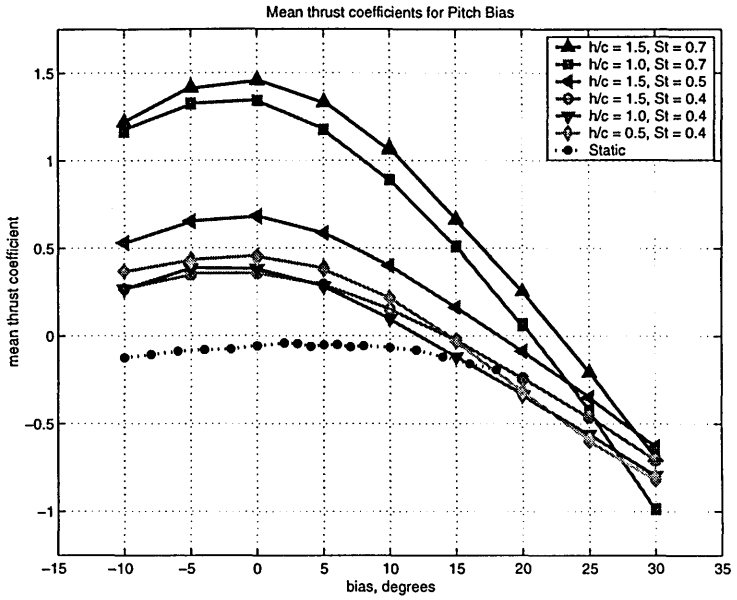

Figure 5-2: Mean thrust coefficients for Bias Tests

maneuver an AUV will result in a different heading and velocity. The relative flow seen by the foil would then change, resulting in different forces. Additionally unsteady currents would change the forces unless sensors were used to detect the inflow and it was steady. Then the AUV could adjust the flapping parameters to account for changes in the inflow.

Next we will look at the accompanying thrust component of the force for bias tests. Figure 5-2 plots the mean thrust coefficients as a function of bias angle for two different Strouhal numbers and three different $h_{0.7}/c$ values. We note that adding pitch bias always decreases the thrust coefficient, and that the effect of higher Strouhal number diminishes as the bias angle increases. The same trends were observed for the two-dimensional case. At 30° bias angle, the thrust coefficient appears to be almost independent of the Strouhal number. Also, the thrust coefficient becomes negative at 15° bias for the lower Strouhal number cases, and 20° bias for the higher Strouhal number cases. Finally, it is important to note that small bias angles still produce useful amounts of thrust, especially for high Strouhal number. As was true with lift, the effect on thrust of $h_{0.7}/c$ or roll amplitude ϕ_o appears to be small.

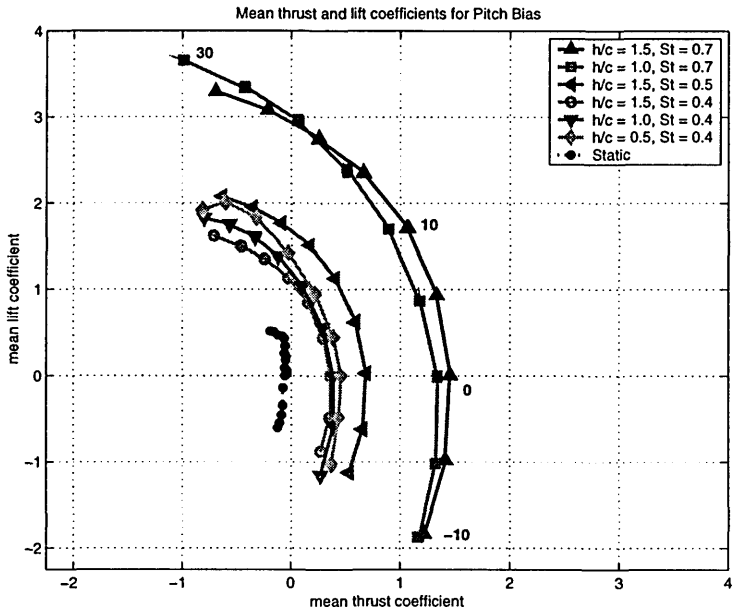

Figure 5-3: Mean thrust and lift coefficients for Bias Tests

The mean lift and thrust coefficients are given in Figure 5-3. The horizontal axis represents C_T and the vertical axis C_L. Each curve covers the range of bias angles; the zero bias angle always provides near zero mean lift. A few bias angles are labelled in the figure. The transition from thrust to drag producing motions occur for a bias angle between 15° to 25°. The transition in the 2-D case occurred at 24°, so this correlates well. Since the flapping foil is used for both propulsion and maneuvering, we can deduce the magnitude and direction of the forces produced from this plot of their components. Components of negative thrust with high lift represent parameters which create a maneuvering and braking force. Components of thrust and moderate values of lift would provide a maneuvering force while still creating a propulsion force.

5.2 Starting Maneuvers

A related problem in maneuvering involves the forces created when the foil moves through a single cycle, in still water. In these tests, the foil moved through either one half or one full cycle of roll motion. Tests were done at two inflow conditions:

still water, and then for the lowest possible speed of the water tunnel, 0.4 m/s, for comparison. The purpose of these tests was to begin to quantify the forces produced when a foil propelled body starts from rest [6].

For all tests, $h_{0.7}/c = 1.5$, or 12° roll amplitude. In all cases the foil was brought out to the maximum roll amplitude slowly, then swept through one full or one half-cycle of roll. The pitch is at 0° at the maximum roll amplitudes, and at its maximum amplitude as the roll crosses zero (identical to all previous tests). Therefore a pitch amplitude of 90° means the foil is perpendicular to the inflow at the maximum roll velocity. The maximum pitch amplitude ranged from 30° to 90°, in increments of 10°. Three different periods, $T = [1.0, 0.7, 0.4]$ seconds were tested. This corresponds to maximum roll velocities at $R_{0.7}$ of $R_{0.7}\dot{\phi} = [0.51, 0.72, 1.28]$ m/s. The equations of motion for a full cycle starting maneuver are:

$$\phi(t) = \phi_o \cos(\omega t),\ 0 < t < T \tag{5.2}$$

$$\theta(t) = \theta_o \sin(\omega t),\ 0 < t < T \tag{5.3}$$

and the roll velocity in $[\frac{rad}{sec}]$ is given by:

$$\dot{\phi}(t) = -\phi_o \omega \sin(\omega t) \tag{5.4}$$

For a half-cycle, the equations are used for $0 < t < \frac{T}{2}$. We drop the negative sign in equation 5.4 for convenience since it indicates direction only, and these maneuvers are symmetric. In this thesis for starting maneuvers we decided to start and end at maximum roll so that the foil would sweep through a larger continuous angle, rather than starting at zero roll and ending at zero roll. By sweeping the maximum angle the vortices shed as the foil changes direction are probably larger, creating greater forces. An alternative that has been tried in 2-D is to sweep through heave (equivalent to roll in 3-D) in a half-cycle as we did, but to end with the foil rotated to its maximum pitch amplitude. That would be more like a fish flapping its tail to change direction, whereas the motion we do is more like an 'S'. Since the motion

that we did is exactly the same as the motion for propulsion, one could transition smoothly the frequency and amplitudes used in starting for acceleration to a cruising frequency and amplitude.

Figure 3-4 shows the directions of positive X in line with the inflow, and Y in line with the roll motion. In this section, forces will be referred to as X and Y, rather than thrust and lift. For example, in the particular case of a maximum pitch amplitude of 90° the component of force perpendicular to the foil is now in the direction we have thus far referred to as 'thrust'. Therefore to eliminate confusion we will use global X and Y to show the direction of the force components with this understanding.

Before we see sample data and results, we consider the angle of attack profile. In still water there is no U component so β becomes $\frac{\pi}{2}$, giving a 'new' equation for angle of attack:

$$\alpha(t) = \pm\frac{\pi}{2} - \theta_o \sin(\omega t) \tag{5.5}$$

which is no longer a function of the span. The $\frac{\pi}{2}$ takes a minus sign to show when the foil changes direction.

For the half-cycle, the resulting angle of attack profile is shown in figure 5-4. It begins and ends at 90° since there is no pitch angle at the beginning and end of the motion. For the full-cycle we have the same profile, but switches sign when the foil changes direction.

Figure 5-5 shows the resulting angle of attack profile for the full-cycle motion in still water. The switch from negative to positive is not as drastic as it appears on the plot; this is simply the foil changing directions in roll.

Figure 5-6 shows a sample time trace of the X and Y forces and roll and pitch position. This particular case is a half-cycle motion, maximum roll amplitude of 1.28 m/s, and maximum pitch amplitude of 40° in still water. This case comes from the set of motions of the highest frequency. We see that the foil produces a large impulse force in both the X and Y direction. Both signals peak about the time the foil is half-way through its motion, then become slightly negative and finally settle to zero

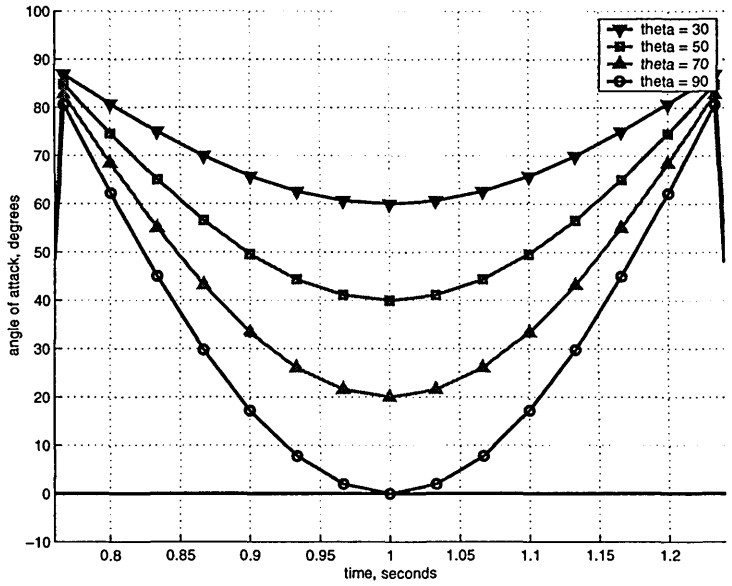

Figure 5-4: Angle of attack profile for half-cycle in still water

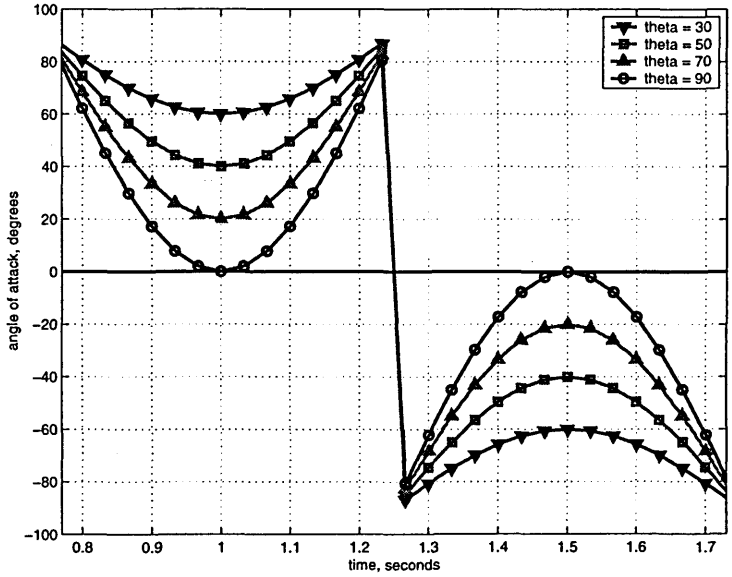

Figure 5-5: Angle of attack profile for full cycle in still water

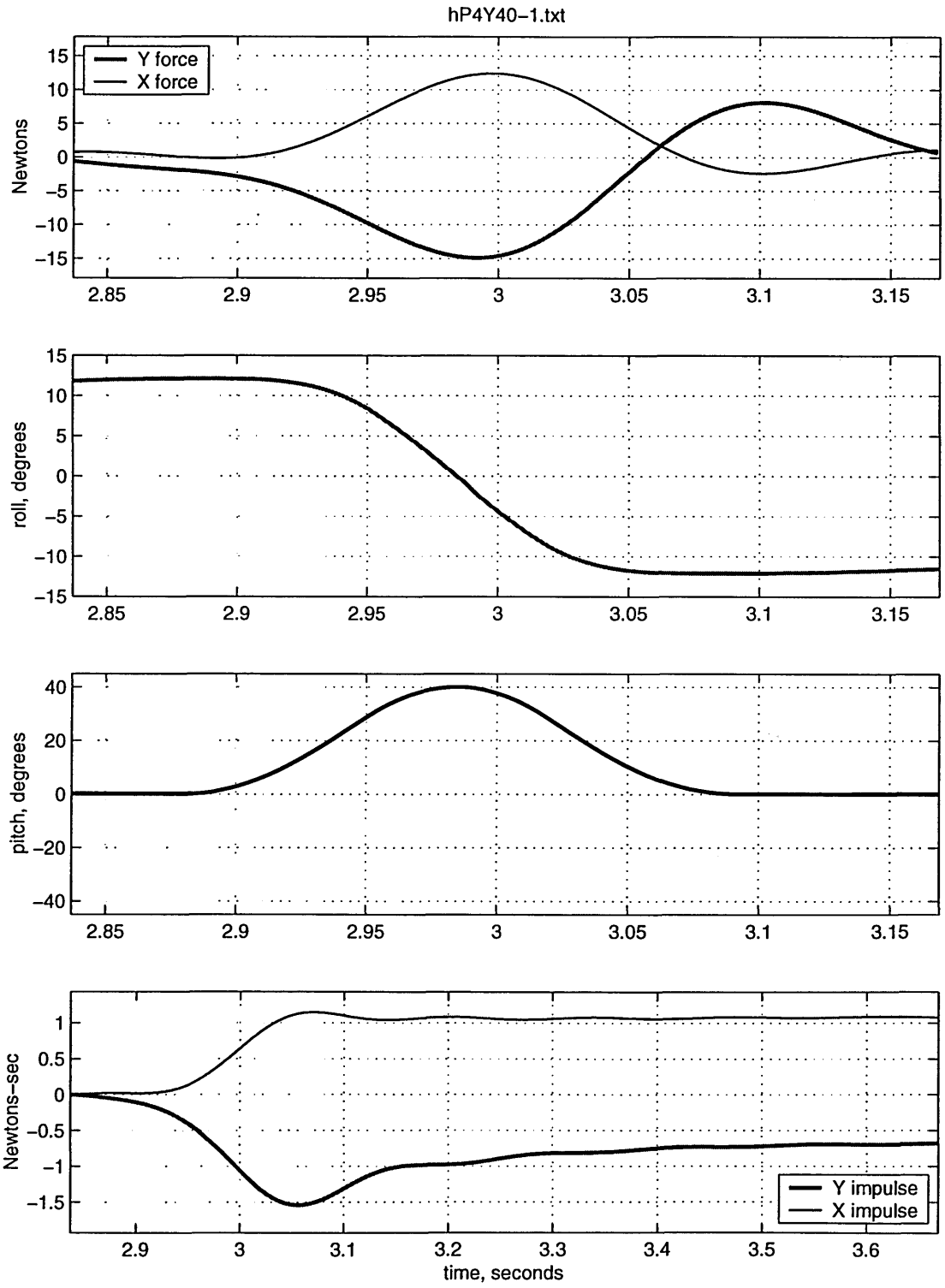

Figure 5-6: Time Trace of forces and position for an Impulsive Start (Half-cycle), Maximum roll amplitude at $R_{0.7}$ is 1.28 m/s, Maximum pitch amplitude = 40°, $U = 0$

after the foil has completed its motion.

Figure 5-7 shows a sample time trace of the same pitch amplitude and period as Figure 5-6, but for a full-cycle of motion instead of half-cycle. The force trace in the X direction now has two peaks, since we have shed a second vortex by going to a full-cycle motion. For a full-cycle, we therefore get twice the net X force measured in the half-cycle case. The Y force has a large negative, and then positive component of about the same magnitude.

It may be simpler to see the net force by considering an integral of the force, or impulse. We therefore start by additionally describing these forces in terms of momentum. From Newton's Second Law:

$$F(t) = \frac{dp}{dt} \tag{5.6}$$

where F(t) is the time variation of the measured force, and $\frac{dp}{dt}$ is the rate of change of momentum. If we integrate over time, we find the change of momentum:

$$\int_{p_i}^{p_f} dp = \int_{t_i}^{t_f} F(t)dt \tag{5.7}$$

The impulse, J, is defined in the impulse-momentum theorem:

$$p_f - p_i = J \tag{5.8}$$

Thus using Equations 5.7 and 5.8 we see that by taking a discrete integral of our measured forces we have the impulse. This may be more useful than considering peak forces, since knowing the change in momentum could be used to predict the velocity of a foil propelled body of known mass.

Figure 5-6 shows the impulse for the sample case of half-cycle forces. The time axis is slightly different for the impulse, so that we can see the ultimate value. The encoder position shows a discontinuity that is most likely an artifact of slightly irregular sampling of our interface program (refer back to Section 3.1.4). We can measure the following quantities from control system theory to a unit step input [27]:

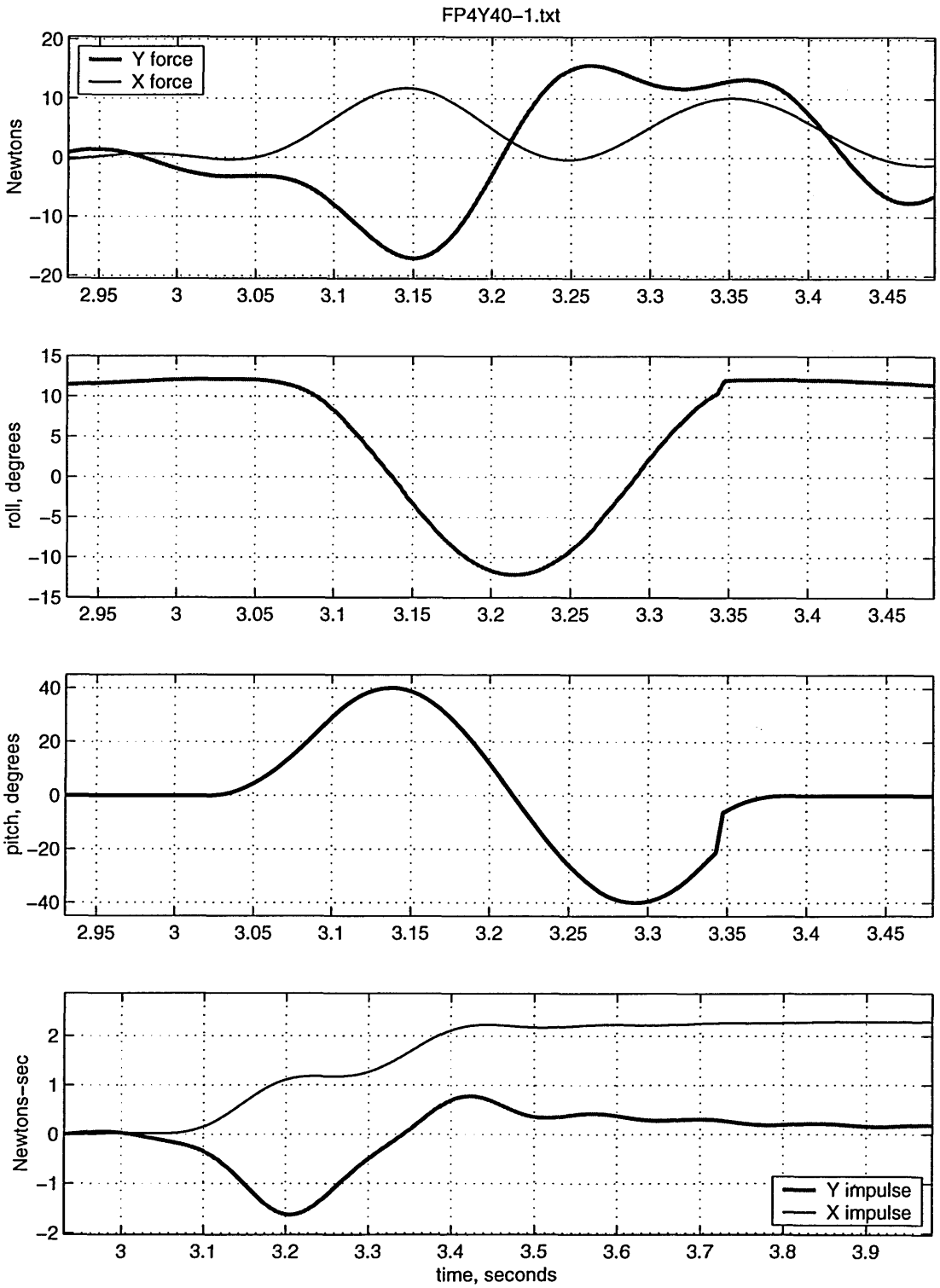

Figure 5-7: Time Trace of forces and position for an Impulsive Start (Full-cycle), Max. roll amplitude = 1.28 m/s, Max. pitch amplitude = 40°, $U = 0$

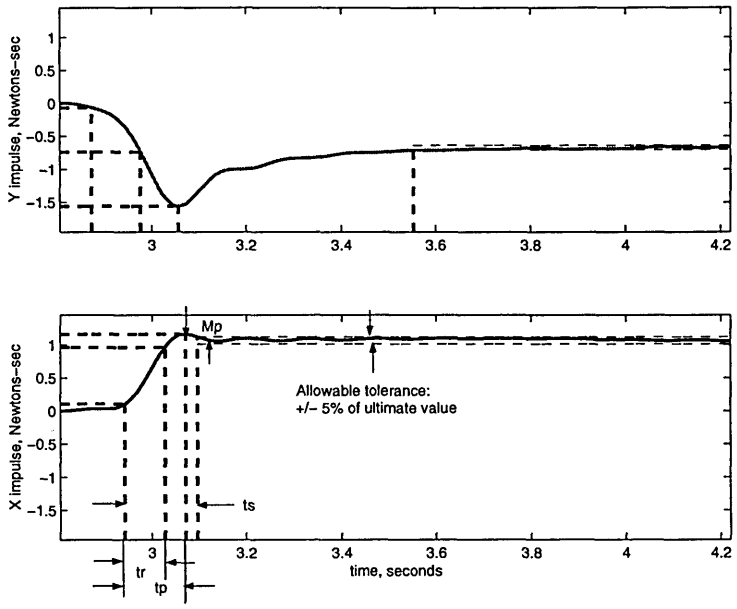

Figure 5-8: Impulse response definitions, half-cycle

- Rise time, t_r, the time required for the response to rise from 10% to 90% of its final value
- Peak time, t_p, the time required for the response to reach the peak of the overshoot from 10% of its final value
- Maximum (percent) overshoot, M_p
- Settling time, t_s, the time required for the response to reach and stay within 5% of its final value from 10% of its final value

Figure 5-8 shows the quantities we have named on the plot of the impulse from Figure 5-6. Both X and Y impulse traces look like a second order system response of an underdamped system to a step input.

Figure 5-9 shows the final value of impulse for the sample case of full-cycle forces shown in Figure 5-7. As was previously mentioned, the full cycle case produces two vortices in the X direction so roughly twice the impulse is recorded. The Y impulse ends near zero, since for the full-cycle the motion is symmetric and produces near

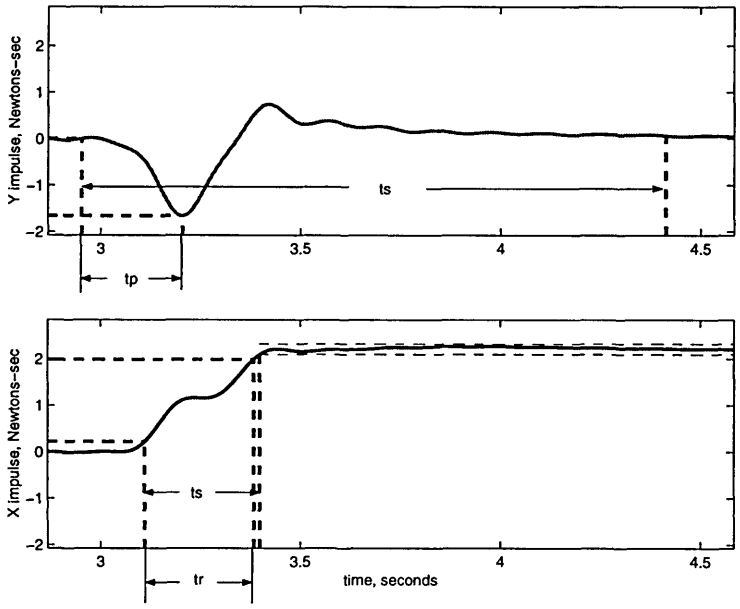

Figure 5-9: Impulse response definitions, full-cycle

symmetric Y forces. In contrast to the half-cycle response, the X impulse trace of the full-cycle case looks like the response in an overdamped system. Therefore the peak time and maximum percent overshoot do not exist. The quantities t_r and t_s are shown in the figure, and retain the same physical definition. The Y impulse trace of the full-cycle case does not look like a transient response to a step input, but we still choose to record the t_p, M_p, and t_s for comparisons between cases.

In the next two sections we present a summary of the results for half- and full-cycle cases in still water, and for an inflow speed of $U = 0.4\ m/s$.

5.2.1 Results for Impulsive Starts in Still Water

Figures 5-10 and 5-11 show the ultimate value of the impulse of X and Y components for all of the tests completed with the half-cycle motion in still water (only the contour for the X component is shown). The black x's mark points where data was actually taken, and the contour lines are interpolations. We see that for the Y impulse force that the difference in roll velocity makes less difference as the pitch amplitude

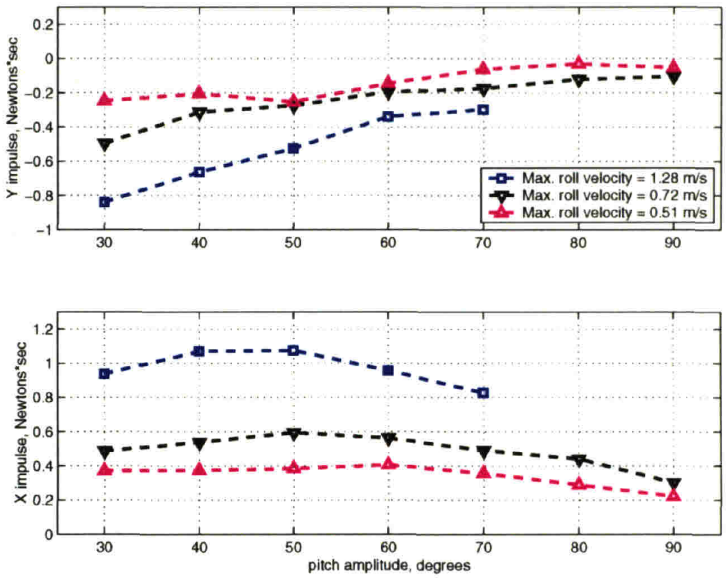

Figure 5-10: Impulse for Half-Cycle Starting Maneuvers in Still Water, X and Y components

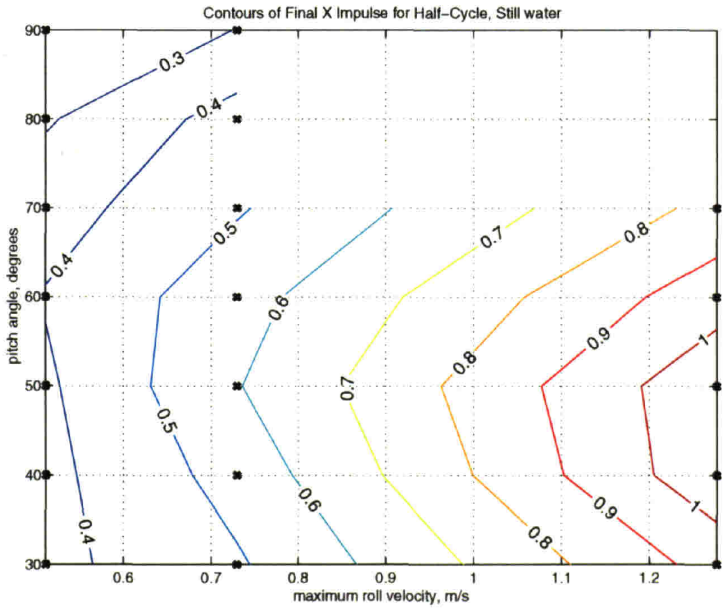

Figure 5-11: Contours of Impulse for Half-Cycle Starting Maneuvers in Still Water, X component

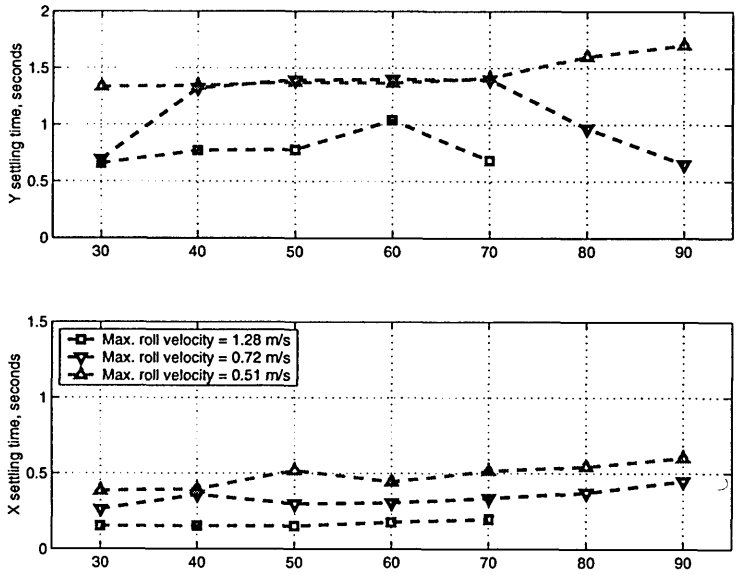

Figure 5-12: Settling time for Half-Cycle Starting Maneuvers in Still Water, X and Y components

approaches 90°. The Y final impulse value tends to zero as the pitch angle increases for all roll velocities. The X impulse is highest for all roll velocities at 50° pitch amplitude. For pitch amplitudes greater than 50° the performance degrades, and is worst at 90°. The impulse for both X and Y are of largest magnitude for the largest roll velocity.

In Figure 5-13 we show the ultimate value of the impulse X and Y components for all of the tests in still water with a full-cycle motion. Due to mechanical limitations, we could not perform high pitch amplitude motions for the highest roll amplitude. We see that the Y impulse for full-cycle motion is close to zero, but that the X impulse is twice as large as the half-cycle motion. The fact that the foil apparatus mounted in the tunnel is sweeping back across its own wake for the full-cycle motions may be one important difference between the forces measured here and those that would be measured on a vehicle.

Figures 5-12 and 5-14 show the settling time. For both cases and both axes, the settling time for the highest roll velocity is the shortest, as one would expect. The

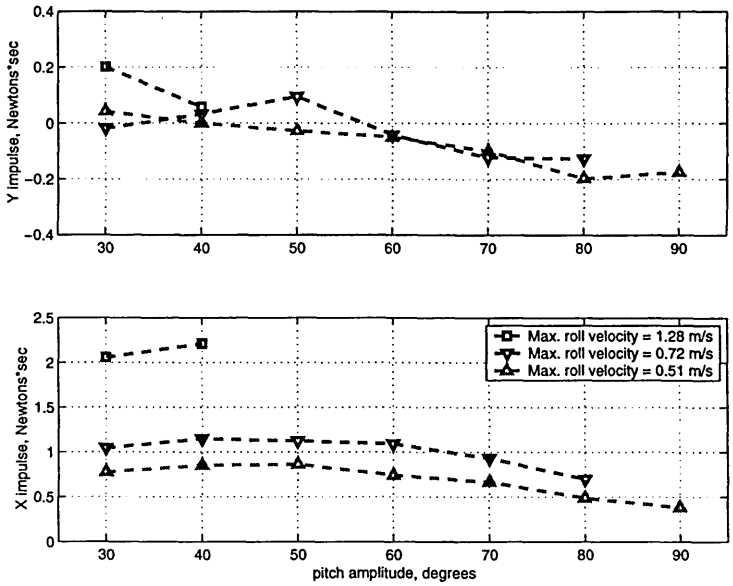

Figure 5-13: Impulse for Full-Cycle Starting Maneuvers in Still Water, X and Y components

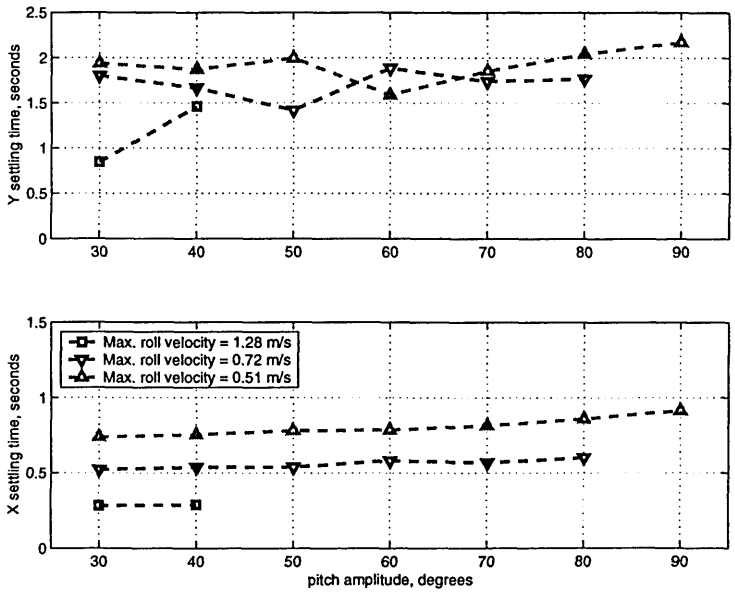

Figure 5-14: Settling time for Full-Cycle Starting Maneuvers in Still Water, X and Y components

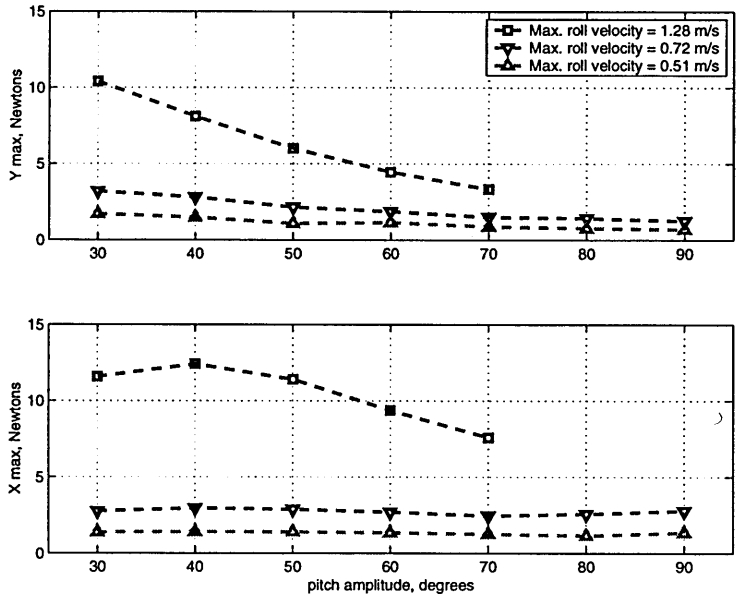

Figure 5-15: Maximum Force for Half-Cycle Starting Maneuvers in Still Water, X and Y components

settling time is almost independent of pitch angle and much more dependent on the driving frequency.

The force data were filtered with a perfect low-pass filter, with a cut-off frequency at three times the driving frequency. Figures 5-15 through 5-16 show the maximum forces of the filtered data for the half- and full-cycle cases. The maximum forces measured in the global X direction are nearly the same between the two cases, while the Y force is roughly twice as large for the full-cycle.

Tables including the ultimate impulse J, rise time t_r, peak time t_p, maximum percent overshoot M_p, and settling time t_s are included in Appendix C for both half- and full-cycle cases in still water.

5.2.2 Results for Impulsive Starts from Low Cruising Speed

We show in Figure 5-17 a time trace of forces and position for an impulsive start, half-cycle, in $U = 0.4\ m/s$ tunnel inflow speed. We see that the signal looks very similar to that of Figure 5-6 since they are for the same period and maximum pitch

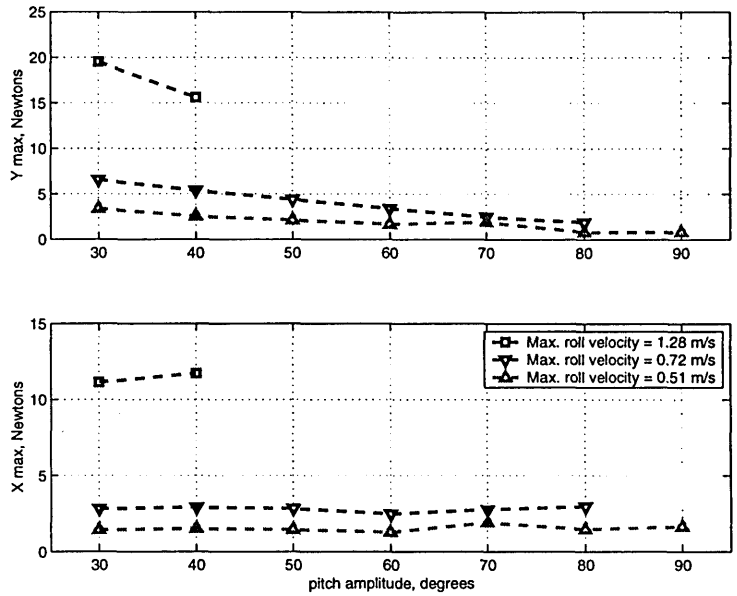

Figure 5-16: Maximum Force for Full-Cycle Starting Maneuvers in Still Water, X and Y components

amplitude. We can compare this figure to Figure 5-6 and see that the X impulse is slightly less. The Y impulse is also of smaller magnitude, and does not dip before settling to a final value.

Figure 5-18 shows a different period and maximum pitch amplitude than figure 5-17. For this higher pitch amplitude and slower roll velocity, we now have a very different looking force time trace. The X and Y forces are small compared to previous cases. The impulse for the X force, shown in the bottom plot in Figure 5-18, is negative. This result is directly related to the angle of attack profile, and will be further discussed after the presentation of the summary plot of impulses.

Figures 5-19 and 5-20 show the impulse of X and Y components for all of the tests completed with the half-cycle motion. We see that the Y impulse gets larger and switches direction as pitch amplitude increases. The X impulse instead gets smaller and switched direction as pitch amplitude increases. This is because now that we have an inflow, the angle of attack is different than the still water cases. Figure 5-20 shows the contours of the X impulse, with points where data was taken marked with

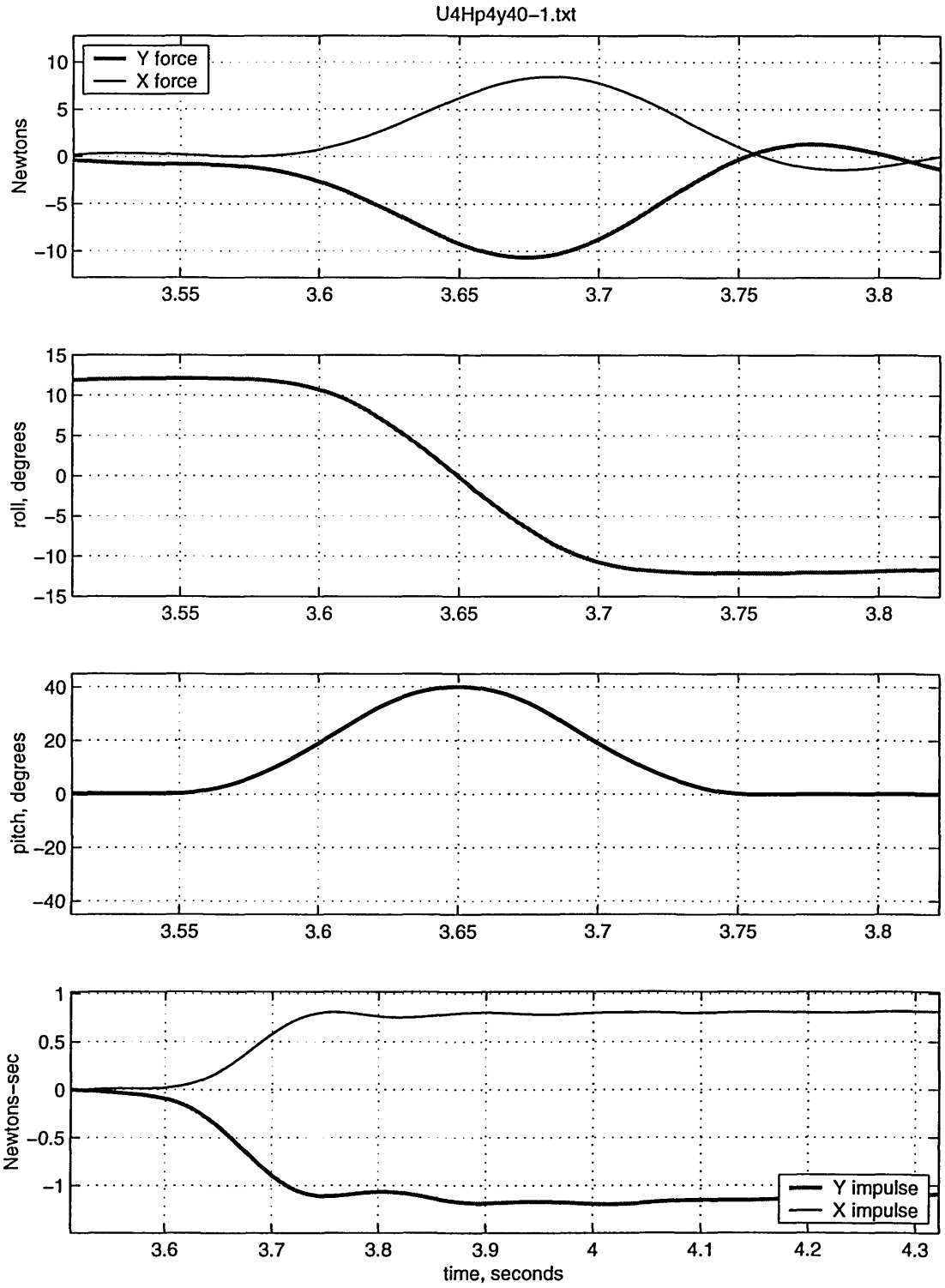

Figure 5-17: Time Trace of forces and position for an Impulsive Start (Half-cycle), Max. Roll Velocity = 1.28 m/s, Maximum Pitch Amplitude = 40°, $U = 0.4\ m/s$

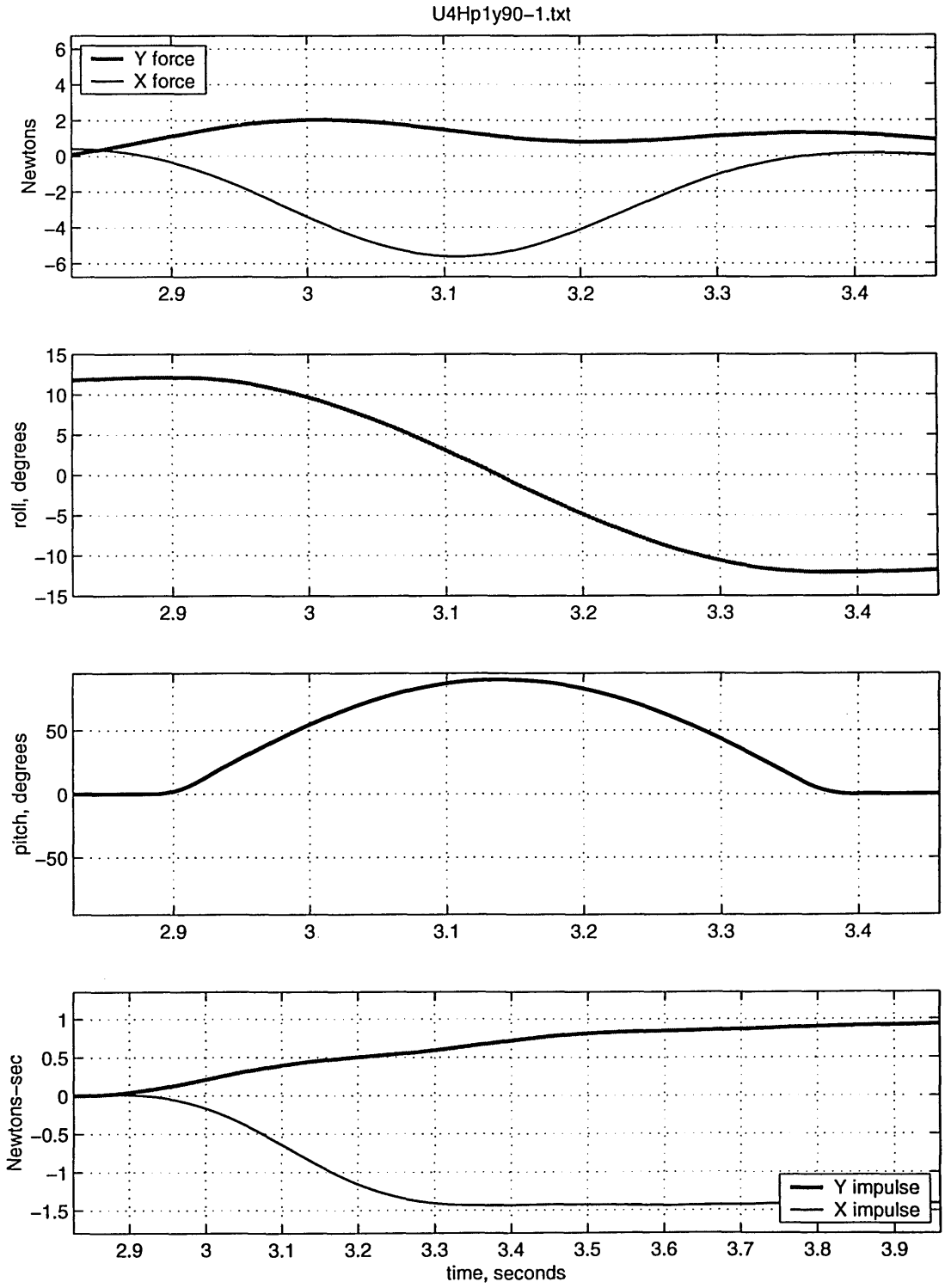

Figure 5-18: Time Trace of forces and position for an Impulsive Start (Half-cycle), Max. Roll Velocity = 0.51 m/s, Maximum Pitch Amplitude = 90°, $U = 0.4\ m/s$

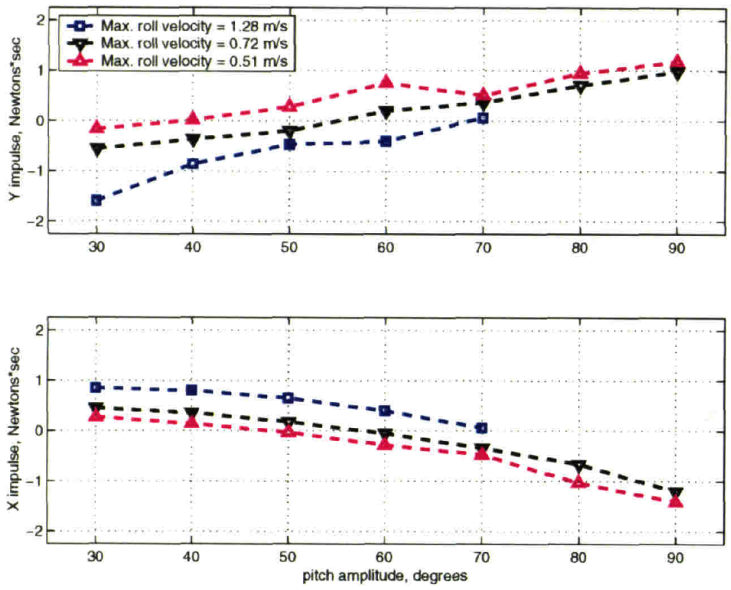

Figure 5-19: Impulse for Half-Cycle Starting Maneuvers for $U = 0.4\ m/s$, X and Y components

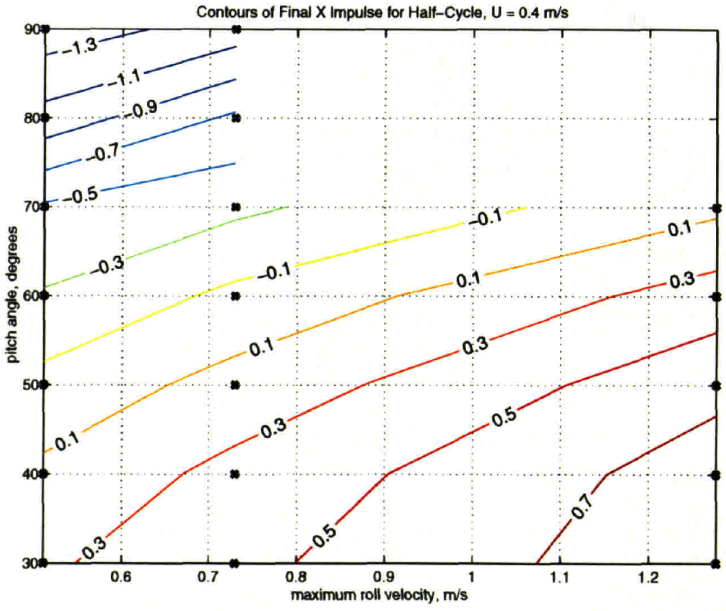

Figure 5-20: Contours of Impulse for Half-Cycle Starting Maneuvers for $U = 0.4\ m/s$, X component

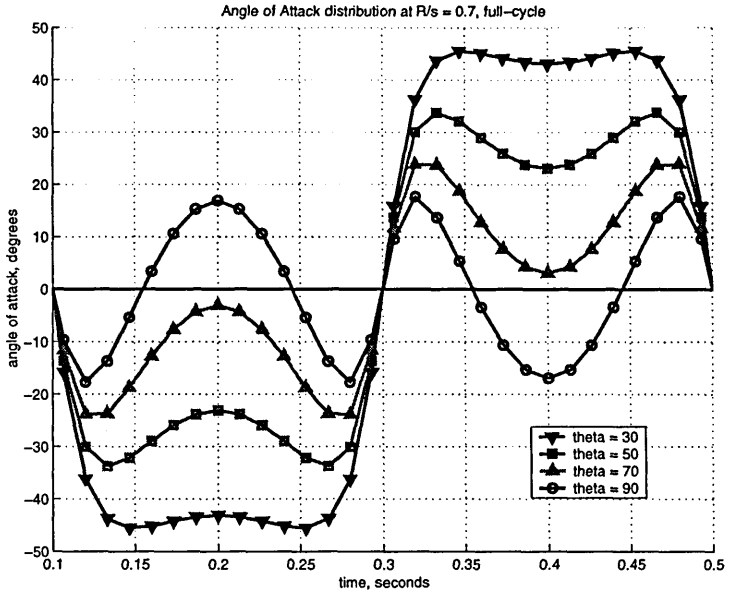

Figure 5-21: Angle of Attack distribution for θ_o = [30° 50° 70° 90°], Max. Roll Velocity = 1.28 m/s, $U = 0.4\ m/s$

black x's.

Figures 5-21 through 5-23 show the angle of attack profiles for the $U = 0.4\ m/s$ full-cycle cases. The angle of attack profile switches sign for a pitch amplitude of 60° for a maximum roll velocity of 0.51 m/s. For a maximum roll amplitude of 0.72 m/s, the angle of attack profile switches sign at 70°. The angle of attack profile for maximum roll velocity of 1.28 m/s never switches sign completely. The X impulse force peaks at 30° pitch amplitude for all cases because this is where the angle of attack profile is the most sinusoidal. As pitch amplitude increases, the angle of attack profile develops double-peaks, degrading the X force. When the angle of attack profile switches sign, the X force goes negative as the foil is producing drag instead of thrust.

In Figure 5-24 we show the impulse X and Y components for all of the tests with a full-cycle motion. We see that the Y impulse for full-cycle motion is almost identical to the half-cycle motion, except for the maximum roll amplitude of 1.28 m/s case where the impulse peaks at 50° instead of 60°. As was with the case with the X impulse forces in still water, the full-cycle impulse is about twice as large as for the

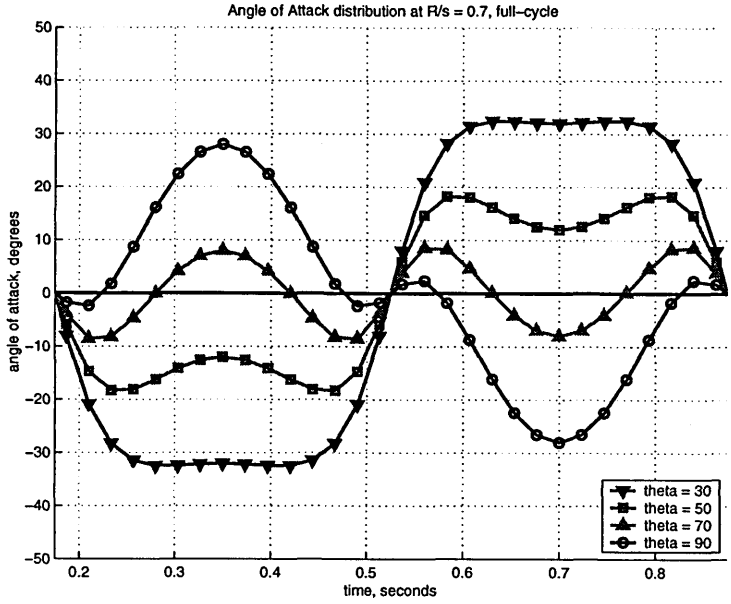

Figure 5-22: Angle of Attack distribution for θ_o = [30° 50° 70° 90°], Max. Roll Velocity = 0.72 m/s, $U = 0.4\ m/s$

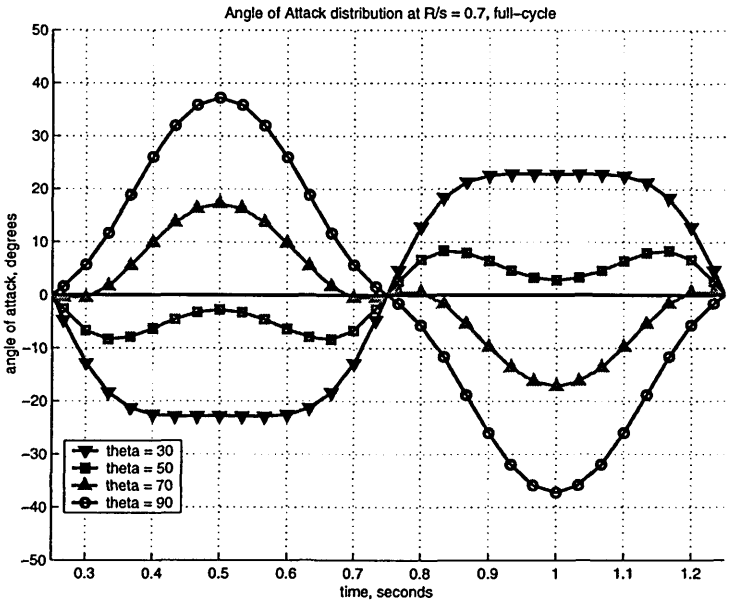

Figure 5-23: Angle of Attack distribution for θ_o = [30° 50° 70° 90°], Max. Roll Velocity = 0.51 m/s, $U = 0.4\ m/s$

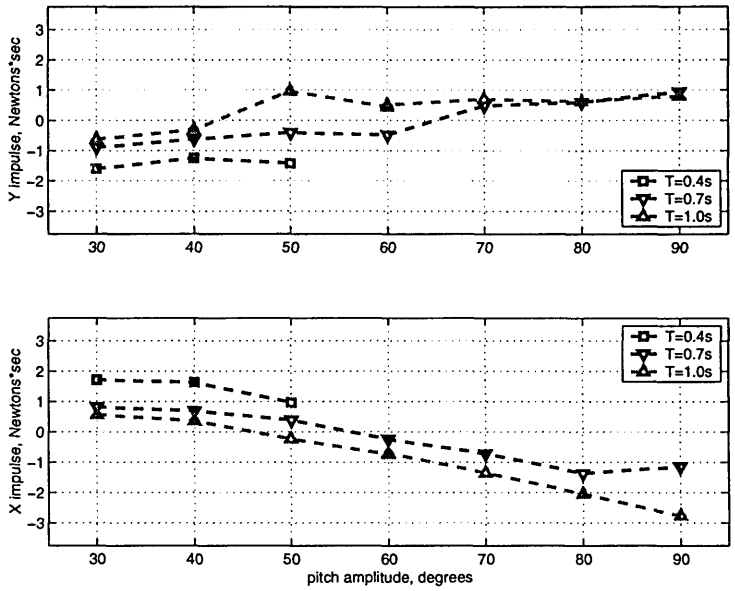

Figure 5-24: Impulse for Full-Cycle Starting Maneuvers for $U = 0.4\ m/s$, X and Y components

half-cycle. The angle of attack profile is the same shape as for the half-cycle, so we see again that the impulse switches sign for higher pitch amplitudes. This type of commanded motion could be used for braking, or deceleration. For example, if the vehicle was cruising at 0.4 m/s the pitch amplitude could be increased and a slower frequency commanded to slow the vehicle instead of back-driving the motors or doing a different flapping motion. This way smooth transitions in the flapping motion can accelerate and decelerate the vehicle.

We conclude from the starting maneuver study that impulsively started foils can produce large instantaneous forces. The highest forces and impulses produced were for moderate pitch angles, between 30° and 50°. The largest roll velocity tested always produced the largest impulse, maximum forces, and shortest settling time. Therefore large roll velocity with moderate pitch angle seem to be the best choice for producing the initial thrust required to start the vehicle. However, we did not try any roll amplitudes other than almost the largest amplitude that this actuator could produce in the tunnel. Intuitively a larger roll amplitude would be better since more water

is accelerated that way. We also did not test pitch angles below 30°, and possibly a smaller pitch angle would provide slightly more acceleration.

The magnitude of our impulse does not seem large enough to accelerate a vehicle of, for example, 100 kg. Obviously a larger foil is required (multiplied by the number of foils). The motions of full and half-cycle were chosen because they would provide the smoothest transition for a vehicle to go from rest to accelerating to cruising, and then decelerating.

Chapter 6

Wake Measurement Experiments

In this chapter, we present the results of tests using LDV and DPIV to experimentally study the wake structure of our flapping foil at one particular roll amplitude, pitch angle, and flapping frequency. These parameters were $h_{0.7}/c = 1.5, St = 0.60$, and $\alpha_{max} = 35°$. This case was chosen for its relatively high thrust with estimated reasonable efficiency. The planform thrust coefficient measured for this run was 1.1. We first used LDV to measure the average velocity across the wake behind five different spanwise locations of the foil, and then chose one spanwise location to produce a phase-average plot of the velocity. This plot gives us a picture of the wake in time, instead of the mean velocity over many cycles. Finally, phase-average DPIV was performed in the two-dimensional X-Y plane at $R_{0.7}$ for the same case.

We see in Figure 6-1 the variation of the angle of attack at different points along the span for our particular case. The angle of attack increases as we move toward the tip, since the excursion of the foil is increasing. Therefore, we expect the velocities closer to the hub to be lower than the mid-span because the angle of attack that it sees is lower.

6.1 Average Wake Velocity Results

Figure 6-2 shows the average streamwise velocity at points across the wake at five different spanwise locations. The data were taken at points across the wake shown

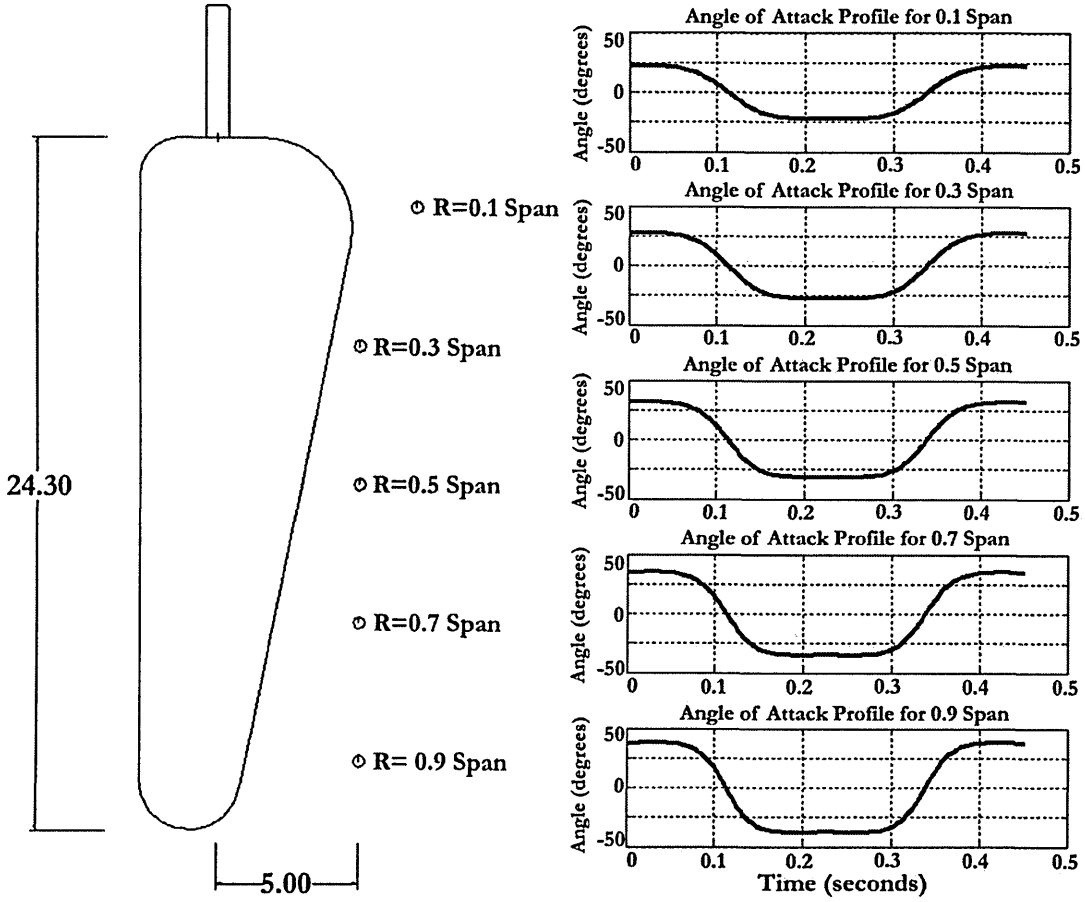

Figure 6-1: Angle of Attack profiles as a function of percent span

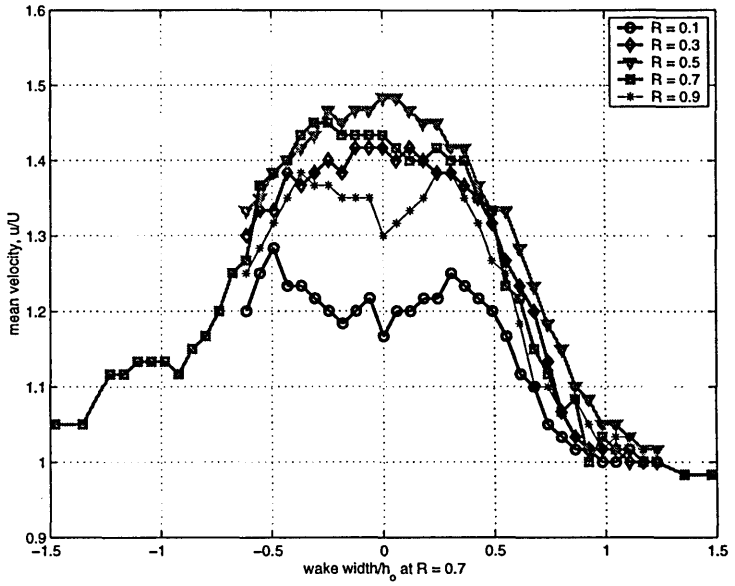

Figure 6-2: Average u/U velocity across the wake

in Figure 6-1 for a Strouhal number of 0.60 and maximum angle of attack of 35°. A sample size of 500 particles per measurement point was used to calculate the mean velocity. We chose to perform LDV all the way across the wake at $R_{0.7}$ to check symmetry. The LDV system performance degrades as we tried to measure velocities on the negative side of the wake because the laser power is diffused by travelling through more water. The sample size per point went as low as 300 in the interest of collection time. Therefore, for the other spanwise curves we assumed symmetry since the data quality is poorer on the other side of zero. We see that using the arc length at $R_{0.7}$ as an estimate for $2h_{0.7}$ is a valid choice because when nondimensionalizing the wake width by the roll amplitude at the 0.7 span location, we find the nondimensionalized wake width is indeed 1. We also see in increase in velocity relative to the inflow for all spanwise curves. A jet is being produced by the foil at about 1.5 times the inflow speed at its maximum. The largest velocity measured was at the mid-span. The $R_{0.3}$ and $R_{0.7}$ span curves are slightly lower, and the lowest velocity produced is near the hub ($R_{0.1}$). Near the tip, $R_{0.9}$ we see that the velocity is also lower, as expected. Although the angle of attack is highest at $R_{0.9}$, the loading is decreasing because it

has to go to zero at the tip. It seems most of the loading is carried by the foil section between $R_{0.3}$ and $R_{0.7}$.

6.2 Phase-Average Wake Velocity

Different from the average wake velocity, for this data the +5 V DC TTL input signal was synched to the data collection so that every data point collected had a time stamp associated with it. We therefore have finally the average velocity *as a function of foil position.*

6.2.1 LDV measurements

Figure 6-3 shows a phase-averaged plot of the velocity u in the wake. The data were taken by sampling with LDV at points across the wake, in the same way as the average velocity was taken but processed differently. The data were taken about one chord length behind the foil, and the $R_{0.7}$ span, for a Strouhal number of 0.60 and maximum angle of attack of 35 degrees. Each point consisted of 360 bins, so taking 3600 points resulted in bin counts between 5 and 20. Normally a higher bin count, near 100, should be employed but we were somewhat concerned about the robustness of the bellows seal.

The foil's roll motion at $R_{0.7}$ is overlayed in black. In the figure the x axis is the bin number (time), the y axis is the position across the wake, and the z axis is the measured velocity u. The bin number can be thought of as time because it corresponds to a foil position. Stacking each wake cut in chronological order creates a picture of the wake behind the foil during one cycle of motion. The data was copied so that the figure shows two cycles in a row to produce a clearer picture. Velocity above $U_{inf} = 0.6\ m/s$ is shown in red, while velocity below U_{inf} is green. We see that a thrust jet is produced in the middle of the wake, which we expected from what we know about the flapping foil wake (refer to Figure 1-1).

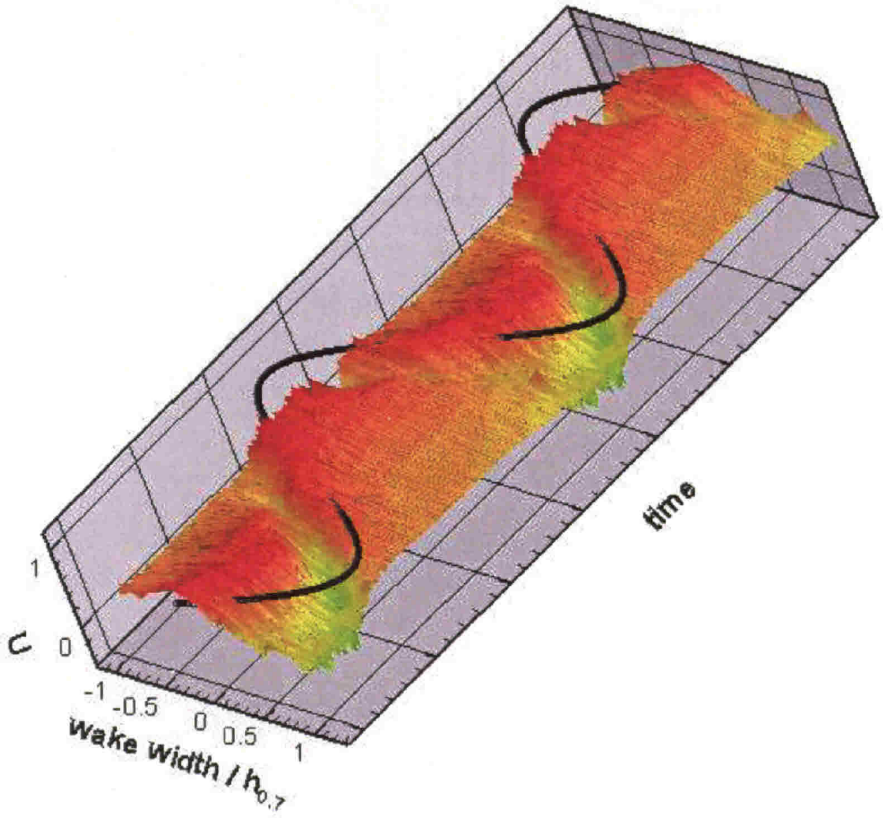

Figure 6-3: Three-dimensional plot of wake behind the foil, $R_{0.7}$, Strouhal number = 0.6, $\alpha_{max} = 35°$

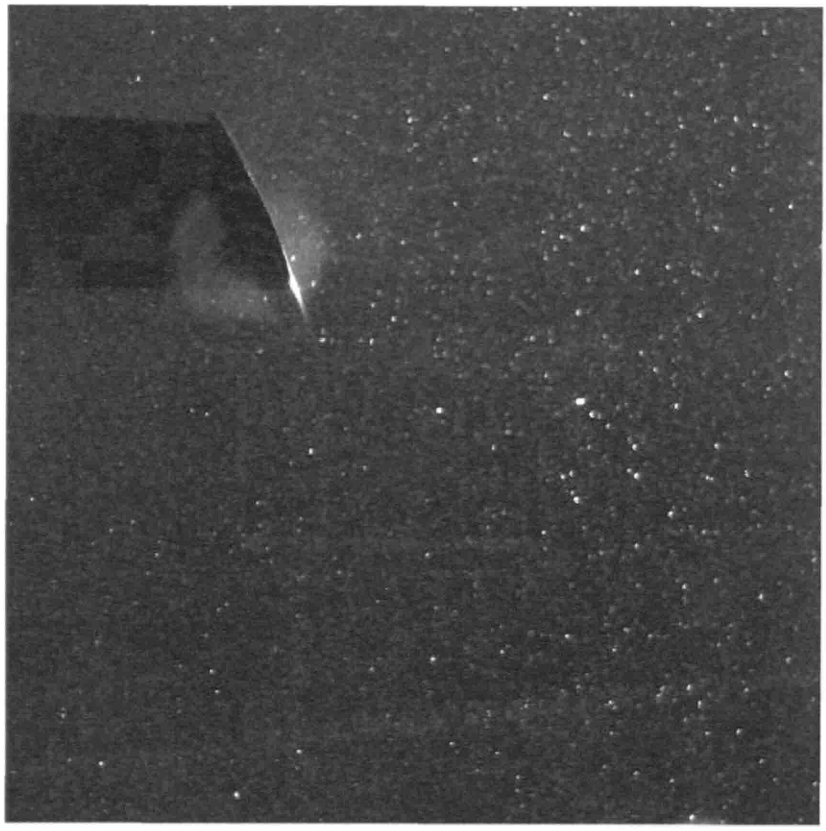

Figure 6-4: Sample PIV raw picture, Roll angle = 0 degrees

6.2.2 DPIV measurements

Figure 6-4 shows a sample picture taken by the PIV system. Figures 6-5 through 6-11 show the fluid velocity field in the wake of the foil (represented by the arrows). The inflow U is coming from above pointing down. The foil position is shown, with the large black arrow indicating the direction and magnitude of the roll velocity. The black dashed line shows the zero position of the foil. Half of the foil cycle is shown, from 0 degrees out to a maximum amplitude of -12 degrees, and then back to 0 degrees. The area to the left of the foil has no arrows because the foil's shadow prevented the laser sheet from illuminating any particles there. The foil and shadow were set to have zero velocity in processing. The velocity arrows overlay the vorticity. The red and blue indicate opposite signs of vorticity. The red is positive vorticity

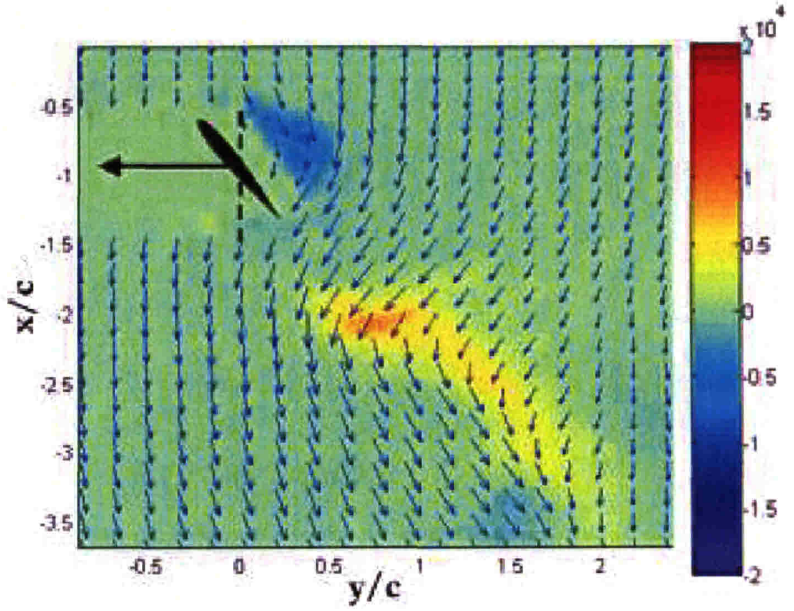

Figure 6-5: Roll angle = 0 degrees

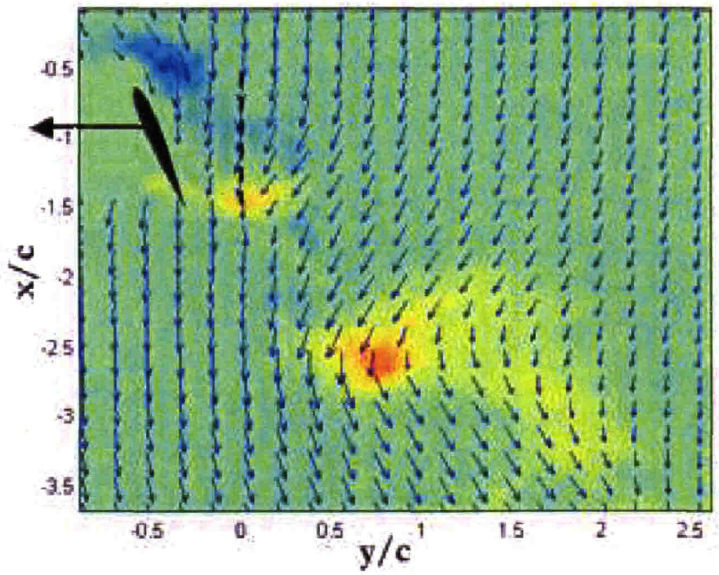

Figure 6-6: Roll angle = -4 degrees

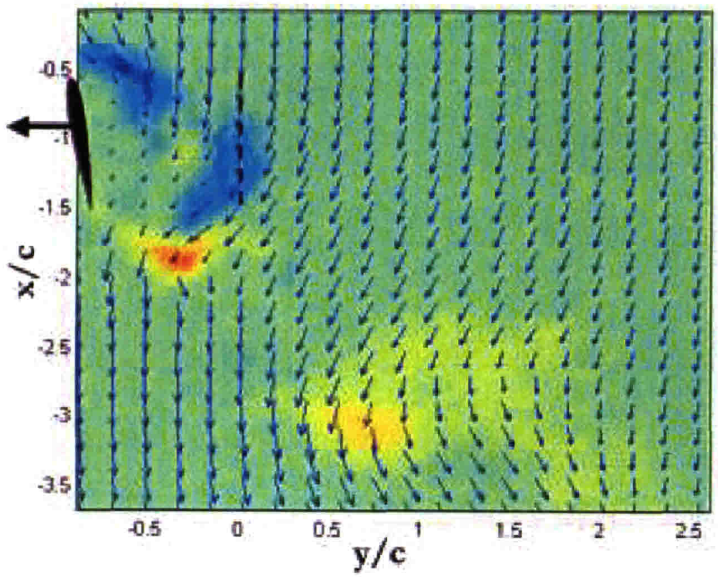

Figure 6-7: Roll angle = -8 degrees

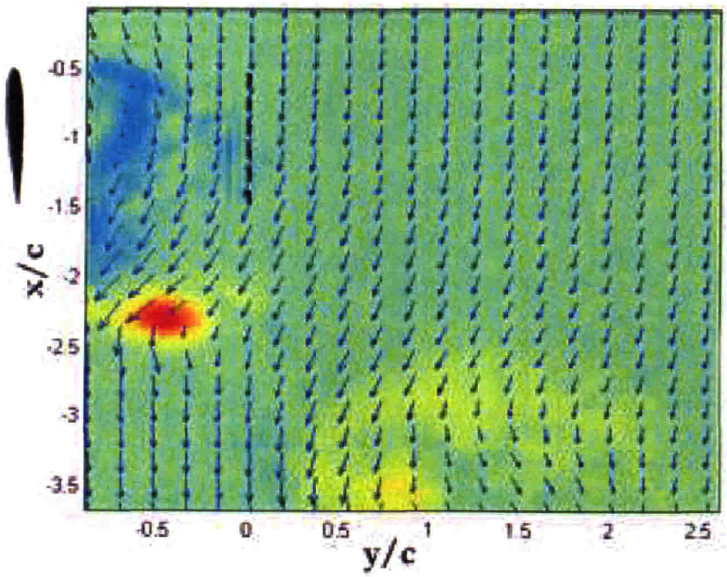

Figure 6-8: Roll angle = -12 degrees

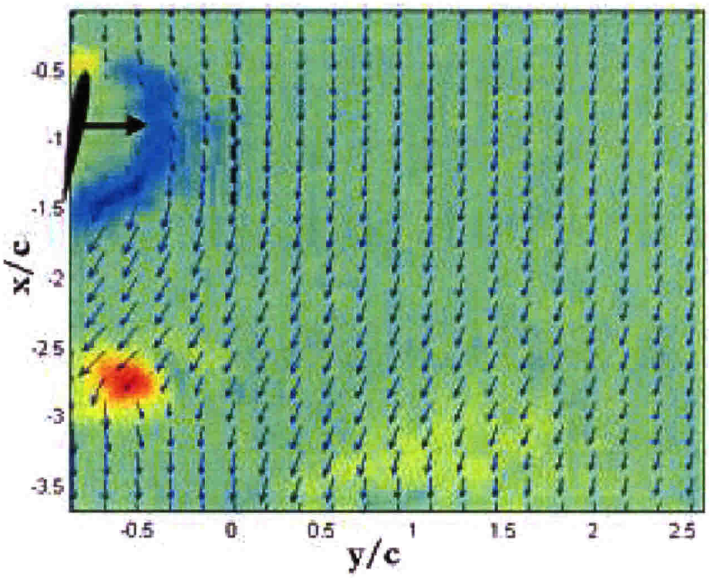

Figure 6-9: Roll angle = -8 degrees

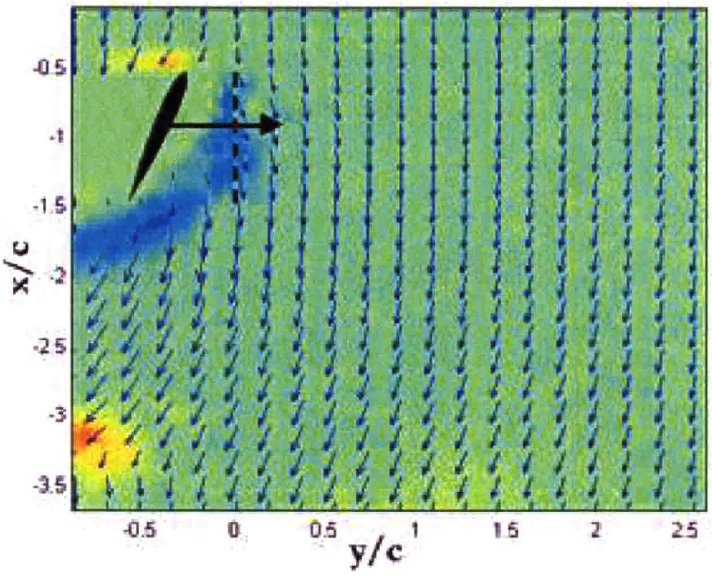

Figure 6-10: Roll angle = -4 degrees

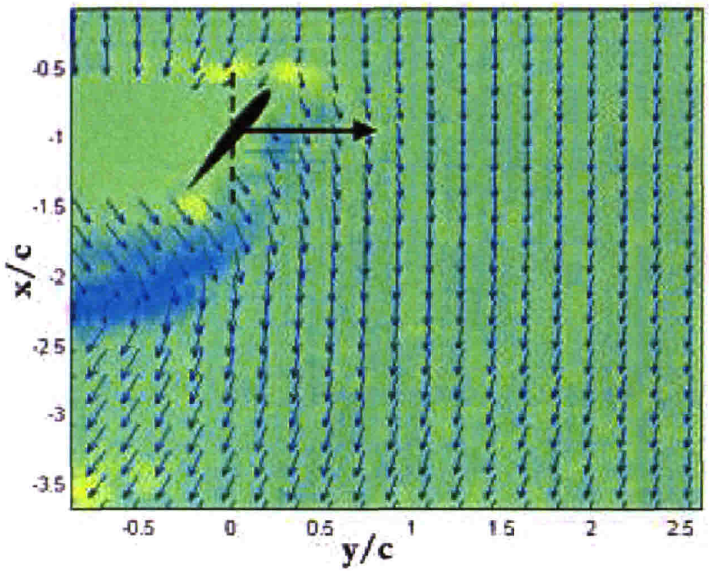

Figure 6-11: Roll angle = 0 degrees

(counter-clockwise), while the blue represents negative vorticity (clockwise). The axes of the plot are non-dimensionalized by the average foil chord. The labels x and y are consistent with the global coordinate system definition in figure 3-4.

We see in Figure 6-5 a thrust vortex approximately c/2 downstream of the trailing edge, as well as a weaker leading edge vortex. As we follow the foil's progression in figures 6-6 through 6-8, we see another vortex with the same sign being generated while the previous one is convected downstream. This second vortex could be paired with the leading edge vortex to satisfy the solid body boundary condition at the foil. The leading edge vortex gets stronger throughout this quarter-cycle progression. Figures 6-9 through 6-11 show the foil moving back towards center. During this quarter-cycle, we see the leading edge vortex merge with its pair and move downstream and to the left as it is shed. The opposite signed vortex weakens the leading edge vortex, which reduces the thrust performance. Based on the position of the shed vortices, the wake width seems to be 1-2 chord lengths, or about 15 cm which is roughly the same as the excursion of the foil.

Chapter 7

Summary

The primary purpose of this investigation was to measure the propulsive and maneuvering forces produced by a three-dimensional flapping foil. First, propulsion tests were completed to measure the mean thrust coefficient over a range of frequency and pitch amplitudes, at two different roll amplitudes. We included a small set of runs actuating only the pitch motion. Next, some maneuvering tests were accomplished by adding a bias offset to the pitch amplitude. Measuring the forces resulting from impulsive starts of the foil in still water and at $U = 0.4\ m/s$ concluded maneuvering tests. Finally, wake visualization tests were accomplished for one flapping condition of moderately high thrust using LDV and PIV.

A secondary purpose of this investigation was to test the limitations of our physical actuator. Flapping foil actuator design is thoroughly reviewed by Polidoro [26]. We began to discover the effects of inertia and vibration while conducting experiments. Mechanical limitations, such as the torque available from the motors, the robustness of the watertight seal, and the strength of the pitch coupling played key roles in determining what types of motions were feasible. Although we were able reach thrust coefficients above 2, mechanical fatigue could result from actually operating at these high frequencies for an extended period of time.

7.1 Propulsion

Propulsion tests were accomplished for two roll amplitudes, $h_{0.7}/c = 1.00$ and $h_{0.7}/c = 1.50$. The test matrix included frequencies and pitch amplitudes corresponding to Strouhal numbers of 0.2 to 0.8 and α_{max} from 15° to 50°. The maximum planform area C_T measured was 2.07 (4.8 Newtons) for $St = 0.8$ and $\alpha_{max} = 40°$ at a roll amplitude of $h_{0.7}/c = 1.5$. Average lift forces were near zero, although peak lift forces over a cycle were roughly twice as large as peak thrust forces. The maximum peak lift measured was 15 N.

Read's [6] highest C_T was 2.4 for 35 degrees maximum angle of attack at $h_o/c = 1.00$. For our set of $h_{0.7}/c = 1.00$ runs, the highest C_T was 1.5 for 45 degrees maximum angle of attack. However, there are a few key differences in our tests. First, our foil had a tapered trailing edge and an aspect ratio of 4.4. Read and Haugsdal used a rectangular foil with an aspect ratio of 6. With our tapered trailing edge, we have less area moving at the high roll velocity. The center of area for a triangular shape is 1/3 while for a rectangle it is 1/2. Perhaps a correction factor to C_T accounting for foil geometry would bring our measurements more in-line with other's results. We also have 3-D tip and hub effects, vibration, and inertial effects of internal components that have impacted our measurements.

We found that high thrust is produced generally at high Strouhal number and high angle of attack. High Strouhal number and low angle of attack create distorted angle of attack profiles for pure sinusoidal motion, i.e. an inflection point. Thrust overcame drag at a Strouhal number of 0.25 for $h_{0.7}/c = 1.50$. The transition point is higher ($St = 0.45$) for $h_{0.7}/c = 1.00$.

Finally the flutter tests, where only the pitch axis was actuated in still water, were not too promising. The forces measured were fractions of a Newton. An optimum foil shape and flexibility would certainly help in producing larger forces.

7.2 Maneuvering

Two sets of maneuvering tests were done, bias tests and impulsive starts. First, we biased the foil's pitch amplitude and measured the thrust and lift forces. A mean C_L of 3.6 was recorded for a 30_o bias for a Strouhal number of 0.7. The static lift coefficient of our foil was 0.55. Flapping frequency and bias angle had a large effect on mean lift. Higher flapping frequency produced larger lift forces. However, mean lift was nearly independent roll amplitude. The maximum mean lift produced by the lower Strouhal number runs was near 2 for a bias angle of 30°. Compared to the static case even the $St = 0.4$ low roll amplitude case produced high lift. Furthermore, the highest bias angle tested did not appear to be the dynamic stall limit. We speculate that higher bias angles produce even larger forces.

We compared lift forces to thrust forces as well and saw that for motions which produce high lift we also produce drag, and for moderate lift we still can produce some positive thrust. The transition from drag to thrust (approximately 20°) represents a bias angle where the AUV would purely rise in the water without moving forward or backward.

Impulsive start tests showed high peak forces and moderate impulse forces. We characterized the impulse in still water with the specifications of a transient response of a second order system to a step input. The numbers for rise time, maximum percent overshoot, peak time, and settling time fully describe the response. In still water, we see that a half-cycle motion produces half of the impulse compared to a full-cycle motion. Of the three roll velocities tested, the highest roll amplitude always well out-performed the slower roll velocities. By out-performed, we mean that the impulse was greater, maximum forces were greater, and rise time, peak time, and settling time were all shorter. The time measurements show how quickly the vehicle can use the thrust to propel forward. Therefore, a high roll velocity with a moderate amount of pitch, between 30 and 50 degrees, produced the best response.

Impulsive start tests were done for comparison at the lowest stable tunnel speed, $U = 0.4\ m/s$. We saw a change in angle of attack profile due to the inflow speed. High

pitch angles (above 60°) produced drag and could be used as a braking device. The final impulses measured were only slightly lower than those in still water. This seems to indicate that once the vehicle starts moving, it can continue to accelerate. The impulses that we measured were relatively small, about 1 Newton-second. However, larger foils and a greater number of foils certainly will produce a higher impulsive force to accelerate the vehicle from rest.

7.3 Wake Measurements

Measurements were conducted using LDV and PIV in accompanying experiments. By measuring the mean flow across the wake, we see a velocity jet nearly 1.5 times greater than the steady inflow, U. This highest velocity in the wake was recorded behind the foil's mid-span ($R_{0.5}$). The mean flow across the wake at the hub was the lowest, which was expected because this is also where the angle of attack is lowest.

Phase-average data taken by the LDV system downstream of $R_{0.7}$ in the wake produced a 3-D wake plot. We saw the evolution of the wake as a function of foil position rather than the mean at one span. We show a jet of high velocity being produced down the middle of the wake. We validated our assumption that the wake width could be approximated as $2h_{0.7}$ by non-dimensionalizing the y-coordinate across the wake by $h_{0.7}$ and found a wake width of -1 to 1 (assuming symmetry).

DPIV results for a Strouhal number of 0.60 and $h_{0.7}/c = 1.5$ show a wake width between 1-2 chord lengths based on the positioning of shed vortices. We see at least three vorticies throughout in the half-cycle of data, a negative leading edge vortex as well as two positive vortices. The leading edge vortex appears to enhance the thrust producing shed vortex, although it is weakened by an opposite signed vortex. Our DPIV data is insufficient to draw direct conclusions of exactly how many vortices are shed per cycle, but it did provide interesting results.

7.4 Recommendations for Future Work

Further work optimizing the shape, size, and flexibility of the foil would be of great interest. The foil in this experiment was chosen because of the size constraints of the water tunnel and for its somewhat similar shape to a penguin wing. Foils designed differently, especially with flexibility, would be an interesting study.

The wake measurements shown here are only a small fraction of the types of wake visualization experiments possible. PIV technology has improved such that now 3-D particle field pictures are possible. This opens the door for experiments in flow visualization for 3-D flapping foils in propulsion, pitch bias, and starting maneuvers. Higher pitch bias angles could be attempted. Furthermore, impulsive starts using different foil motions could be studied.

Finally, a great deal of work remains to map the forces measured in experiments like these to a control system for an AUV using flapping foil propulsion. Once an AUV employing flapping foils is fabricated, pool tests or tow tank tests could be attempted to measure the forces produced by the sum of the foils. At that point, many experiments over a range of flapping parameters could be attempted to further understand the propulsive forces of flapping foils applied to underwater vehicles.

Appendix A

Propulsion Time Data

In the following figures we show data from selected propulsion experiments. The X and Y force traces have been filtered using a perfect low-pass filter with a cut-off frequency of 8 Hz. We chose 8 Hz because above this frequency structural vibrations begin to occur (see Figure 3-10). It is not clear for the runs at Strouhal number = 0.80 whether a higher harmonic of the forces are being filtered out, since the driving frequency is 3 Hz. Structural vibrations are a concern in moving to an AUV application.

We show the four data traces recorded by the two different computers during an experiment, plus the calculated angle of attack profile. Both the angle of attack profiles at $R_{0.7}$ and the root are shown. The time traces show the filtered X and Y force data as well as the pitch and roll position from the recorded encoder feedback. The two data sets, forces and positions, were linked using the pulse signal as a marker. The pulse signal is not shown, but was used in processing to line up the data sets in time. The sampling rate and therefore time is known for the force signal, but determining the real time of the recorded encoder feedback data requires the user to input the commanded frequency. Then we checked that the frequency was correct by comparison with the pulse signal.

We saw in Figure 3-11 that the measured forces have a hydrodynamic and mechanical component. The signals shown here are the measured forces, so there is a component due to mechanics that is not subtracted. The reason it was not sub-

tracted is because it was too difficult to accurately align the two data sets in time to guarantee a perfect subtraction. Additionally, since this is an actuator that could be used in AUV design, the mechanical component would be present. In this case we choose to show the filtered time trace, but with the magnitude of hydrodynamic plus mechanical forces.

The encoder position time trace has slight irregularities. We believe these are due to either communication interrupts between the onboard motion control card and our sampling program, or slightly irregular sampling of our C++ interface program.

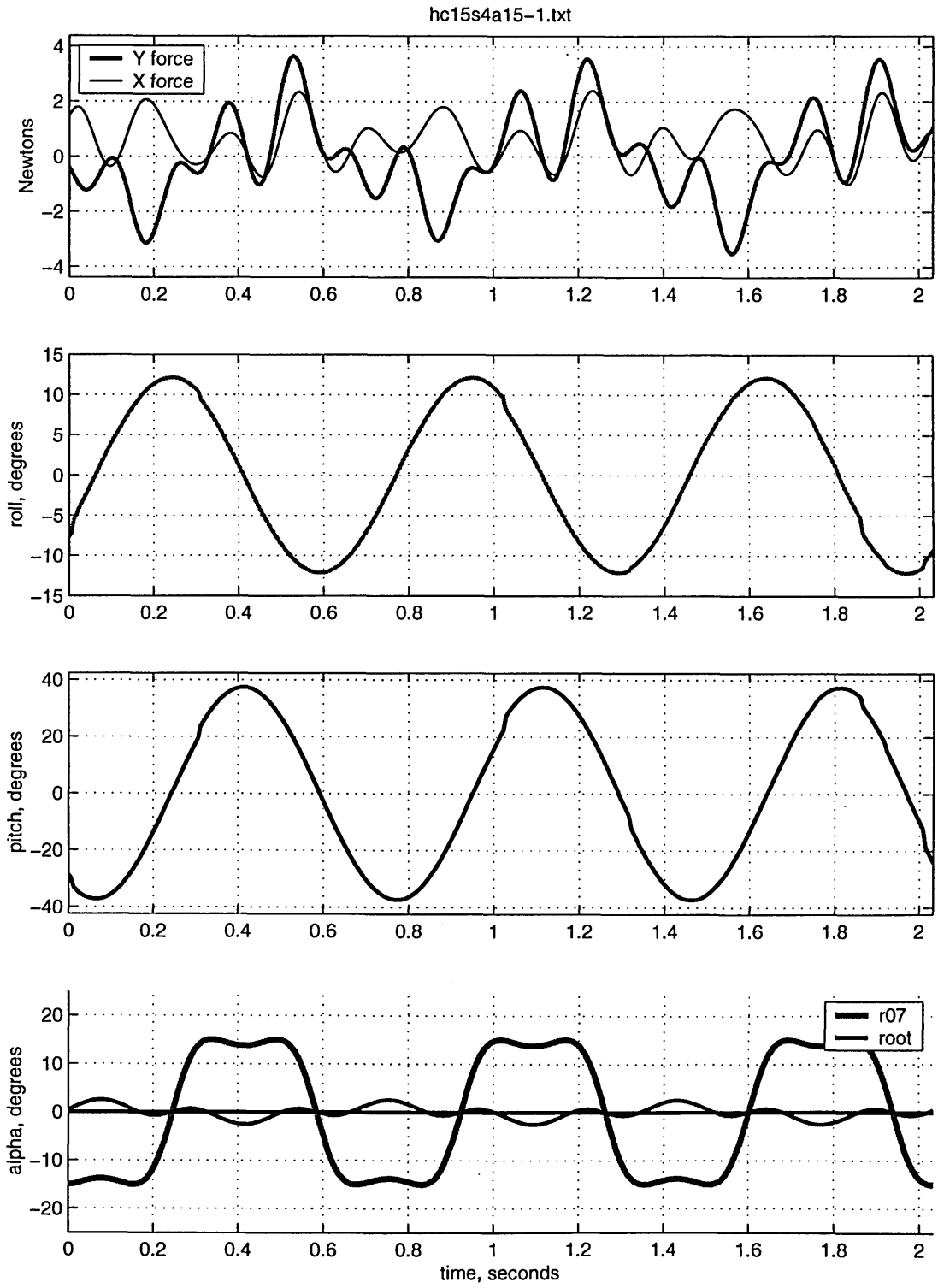

Figure A-1: $h_{0.7}/c = 1.5$, $St = 0.40$, $\alpha_{max} = 15°$

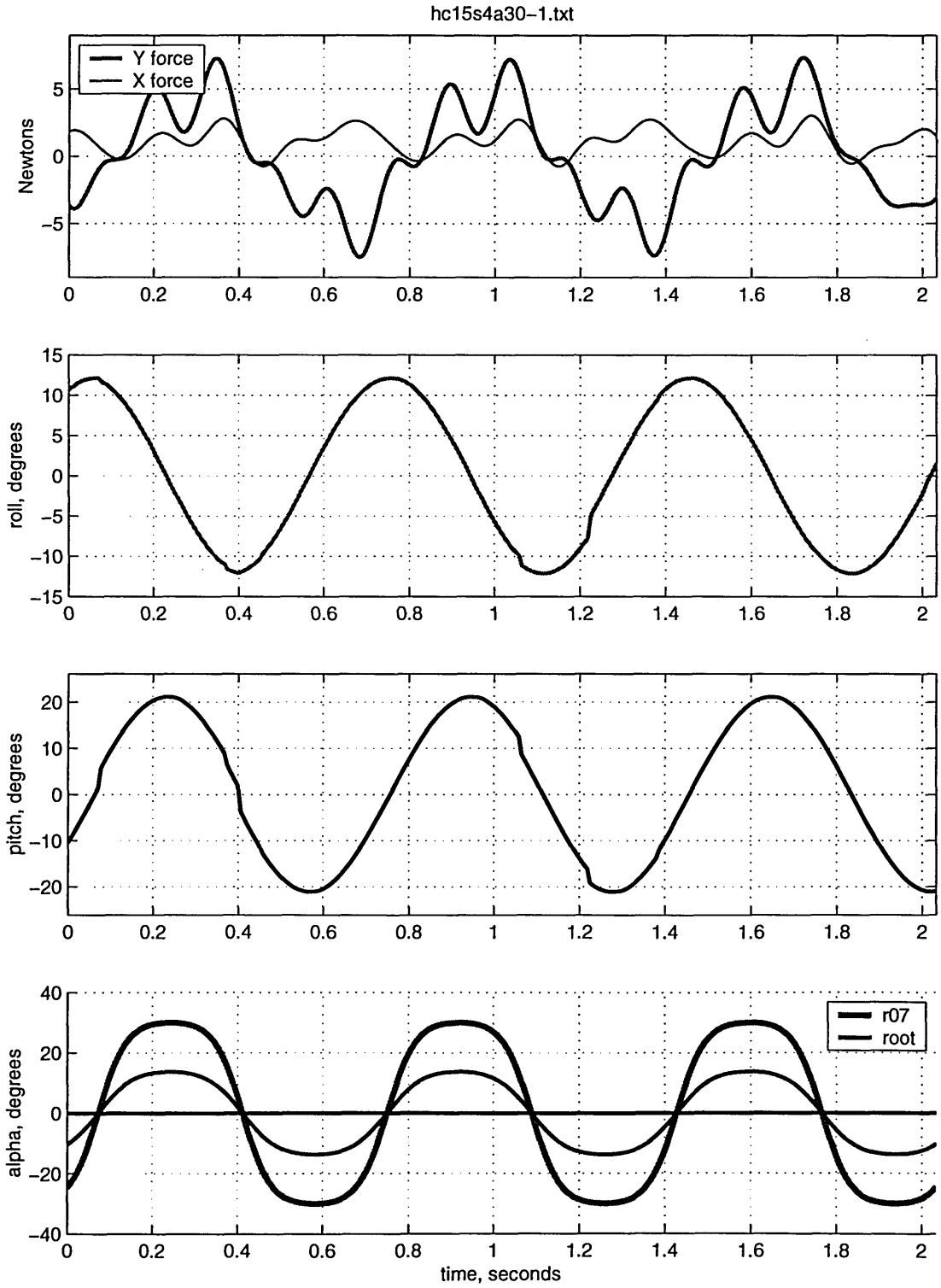

Figure A-2: $h_{0.7}/c = 1.5$, $St = 0.40$, $\alpha_{max} = 30°$

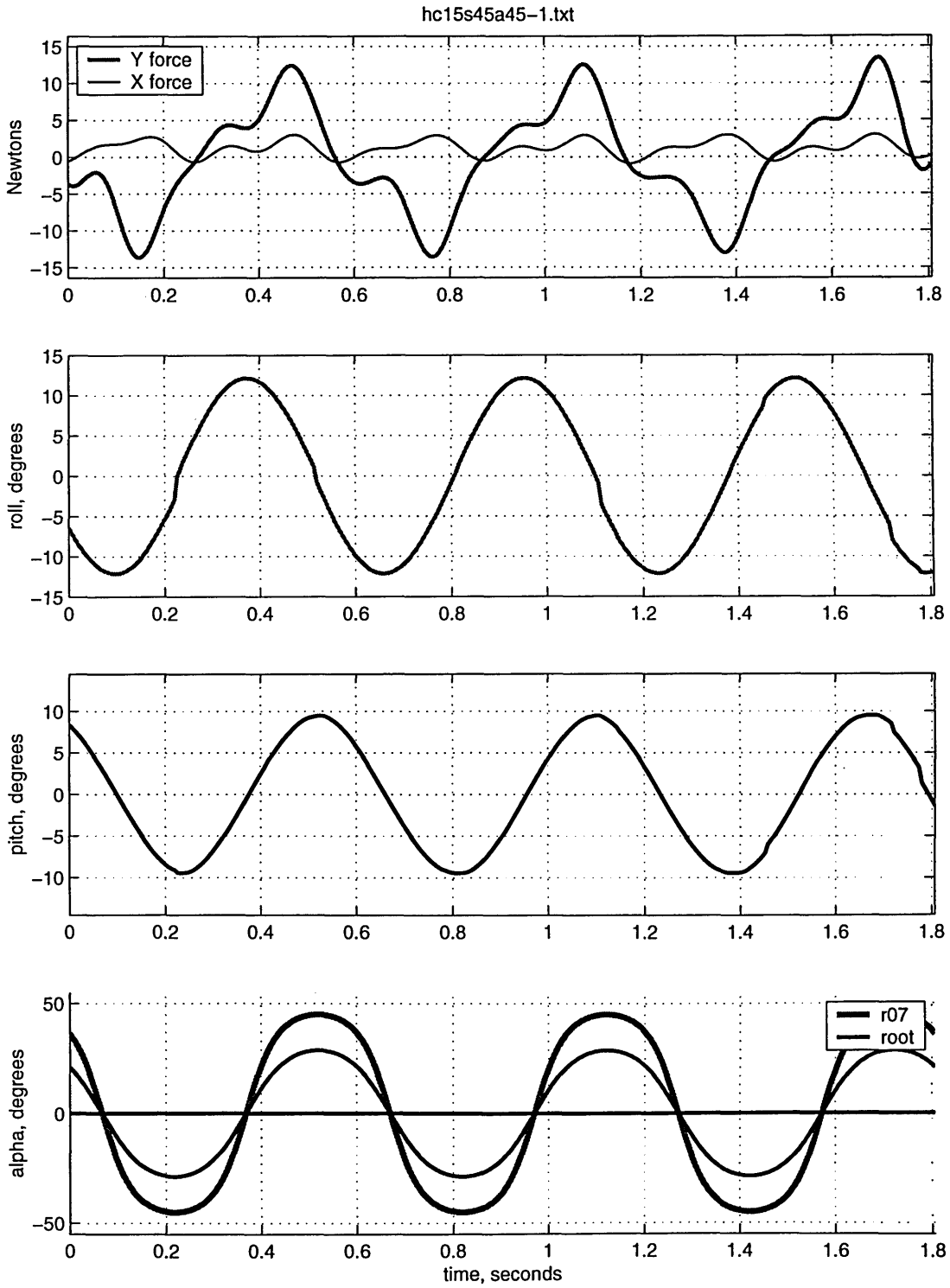

Figure A-3: $h_{0.7}/c = 1.5$, $St = 0.45$, $\alpha_{max} = 45°$

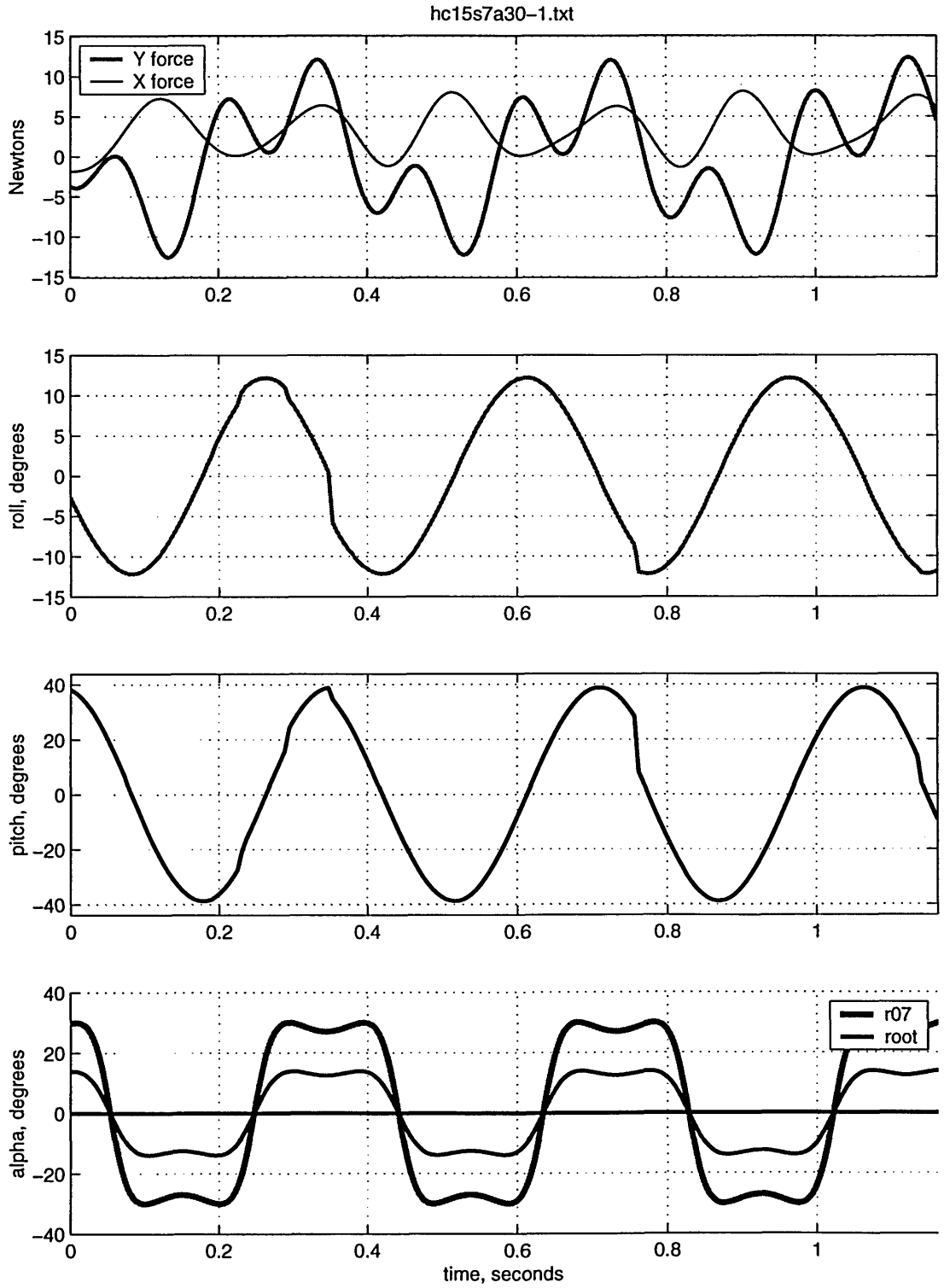

Figure A-4: $h_{0.7}/c = 1.5$, $St = 0.70$, $\alpha_{max} = 30°$

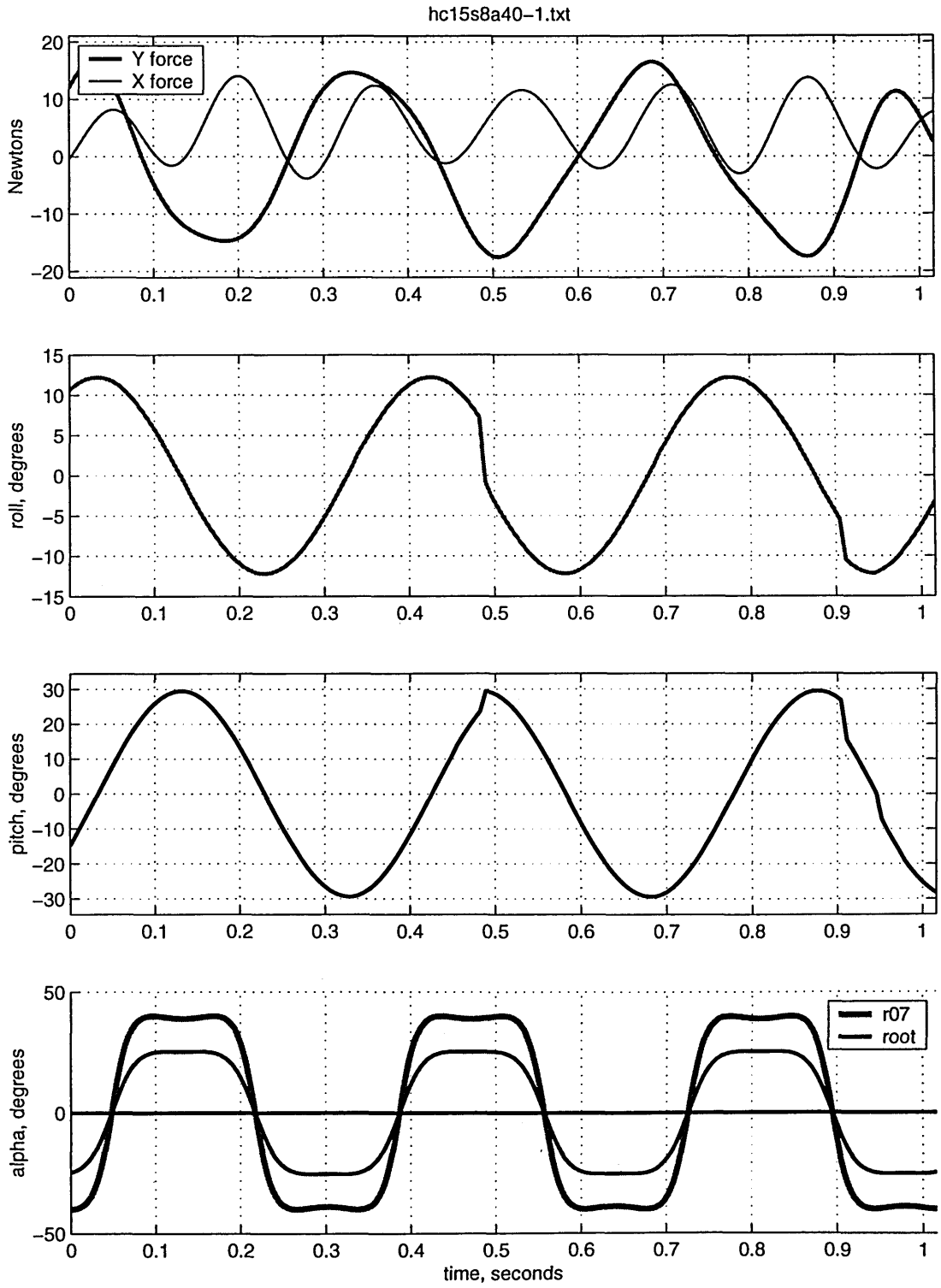

Figure A-5: $h_{0.7}/c = 1.5$, $St = 0.80$, $\alpha_{max} = 40°$

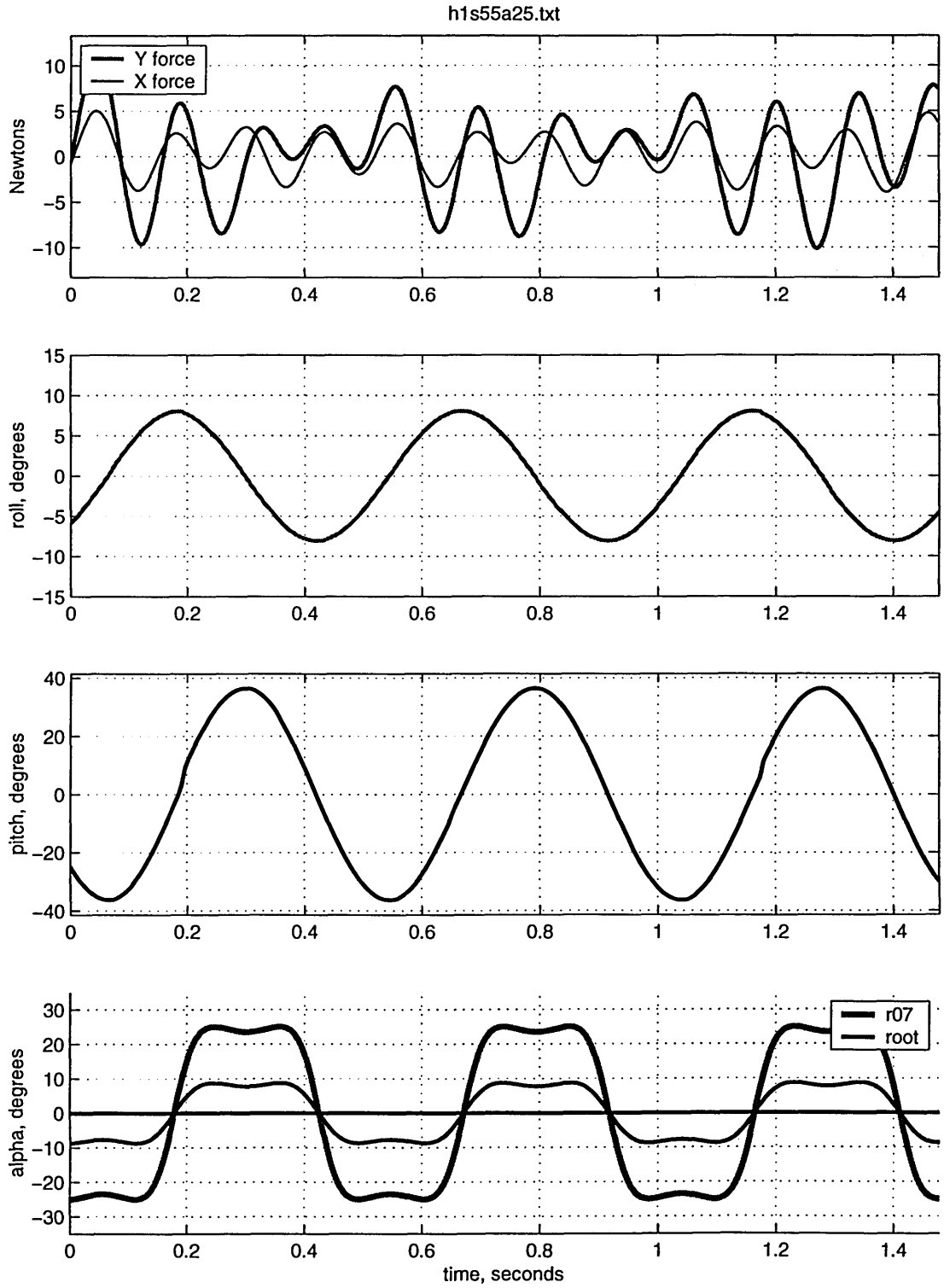

Figure A-6: $h_{0.7}/c = 1.0$, $St = 0.55$, $\alpha_{max} = 25°$

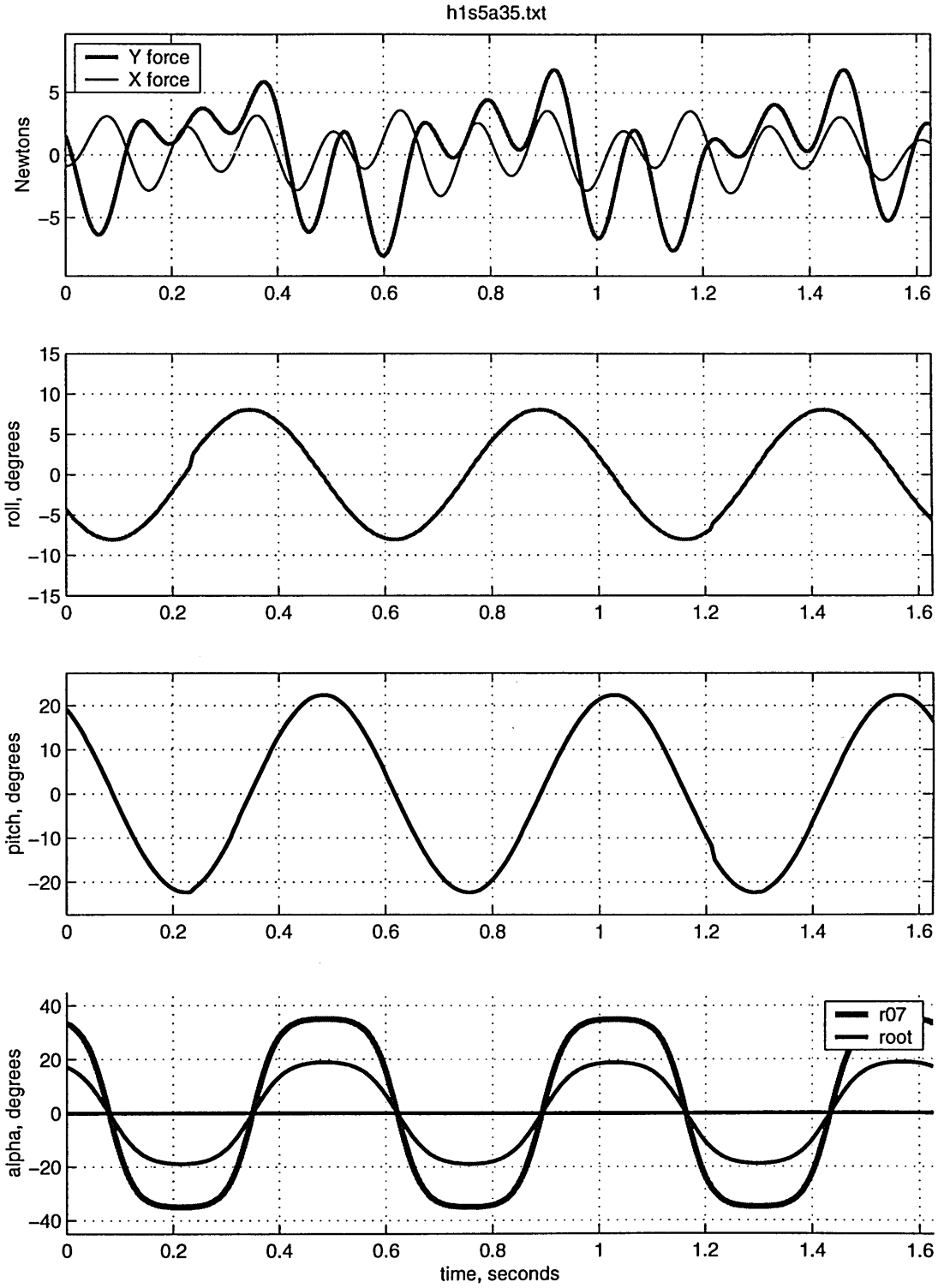

Figure A-7: $h_{0.7}/c = 1.0$, $St = 0.50$, $\alpha_{max} = 35°$

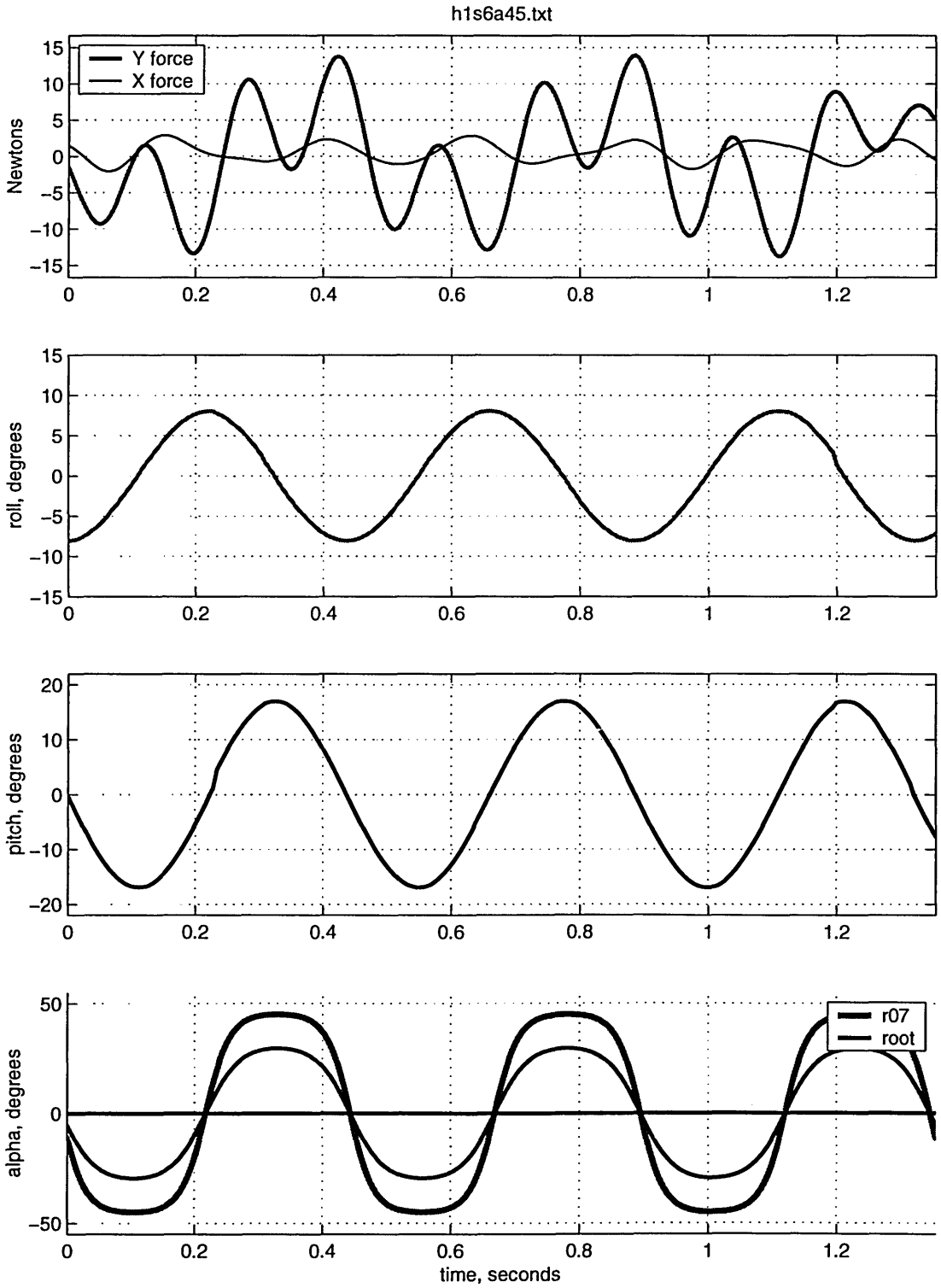

Figure A-8: $h_{0.7}/c = 1.0$, $St = 0.60$, $\alpha_{max} = 45°$

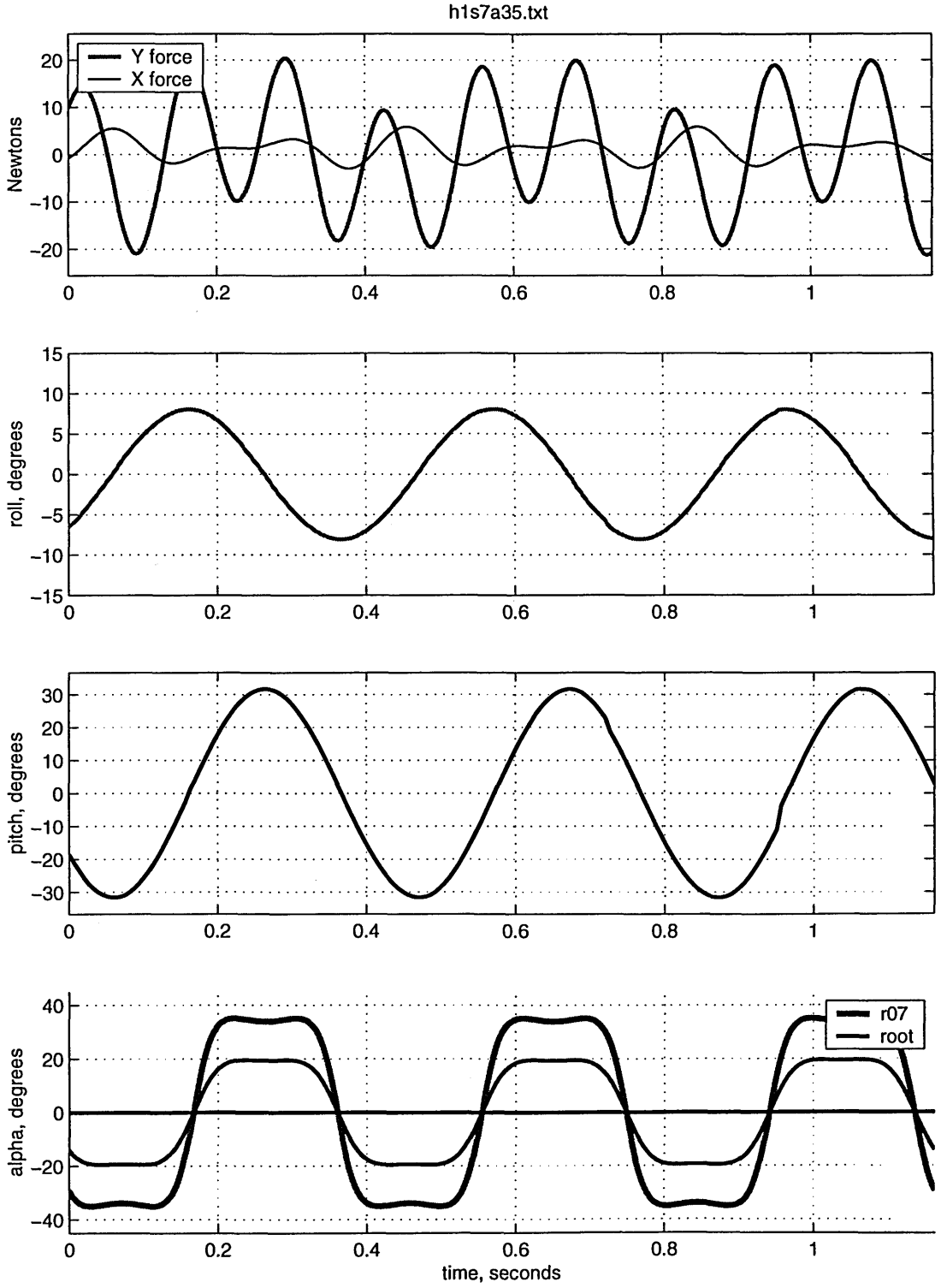

Figure A-9: $h_{0.7}/c = 1.0$, $St = 0.70$, $\alpha_{max} = 35°$

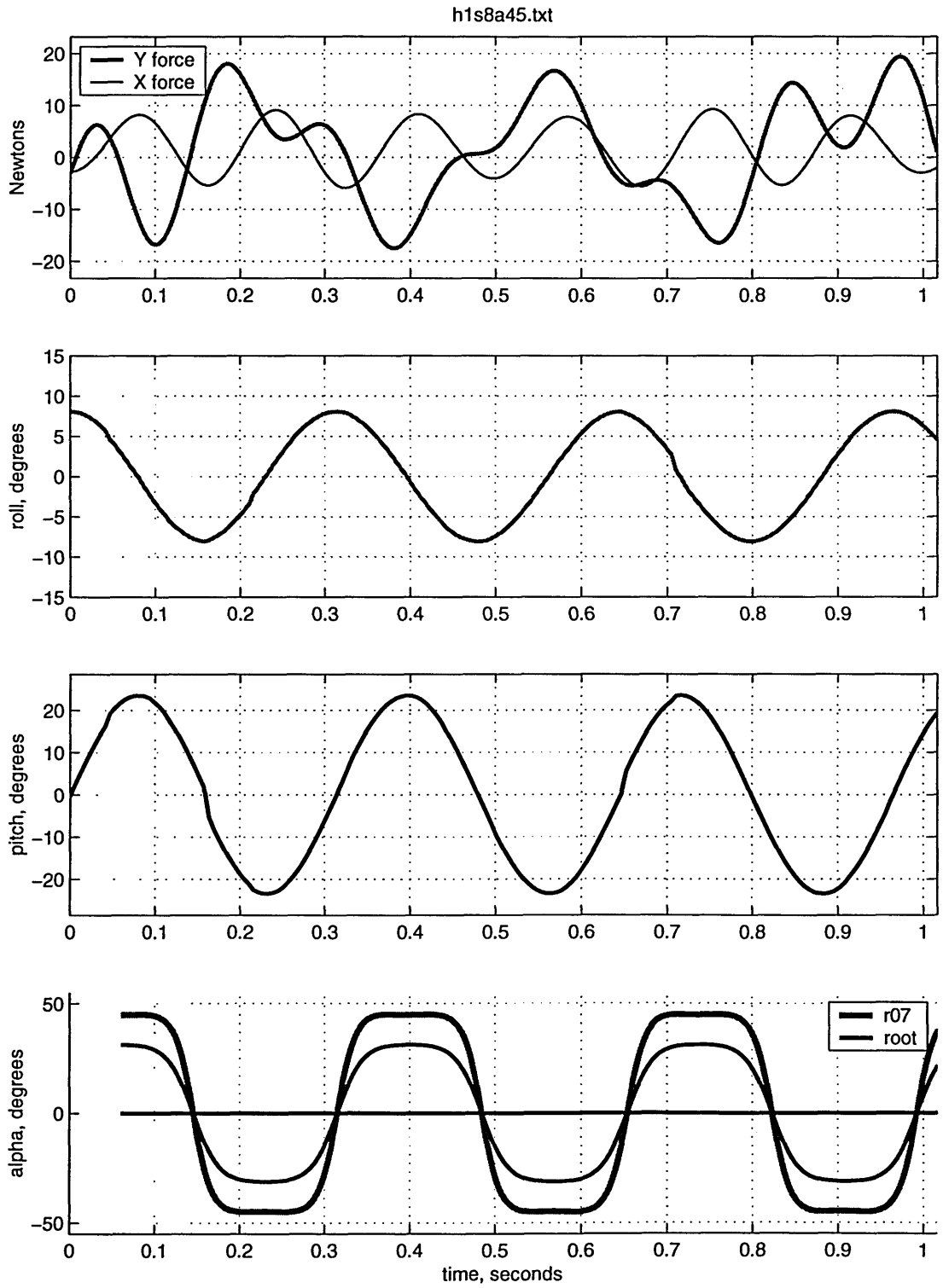

Figure A-10: $h_{0.7}/c = 1.0$, $St = 0.80$, $\alpha_{max} = 45°$

Appendix B

Pitch Bias Time Data

In these figures we show data from selected pitch bias experiments. Filter and calculations are the same as those for Appendix A. Since we see from Figure 5-3 that the $h_{0.7}/c$ parameter does not have much effect on the mean values of thrust and lift, we chose to show only $h_{0.7}/c = 1.5$ experiments with a range of Strouhal numbers and pitch bias angles.

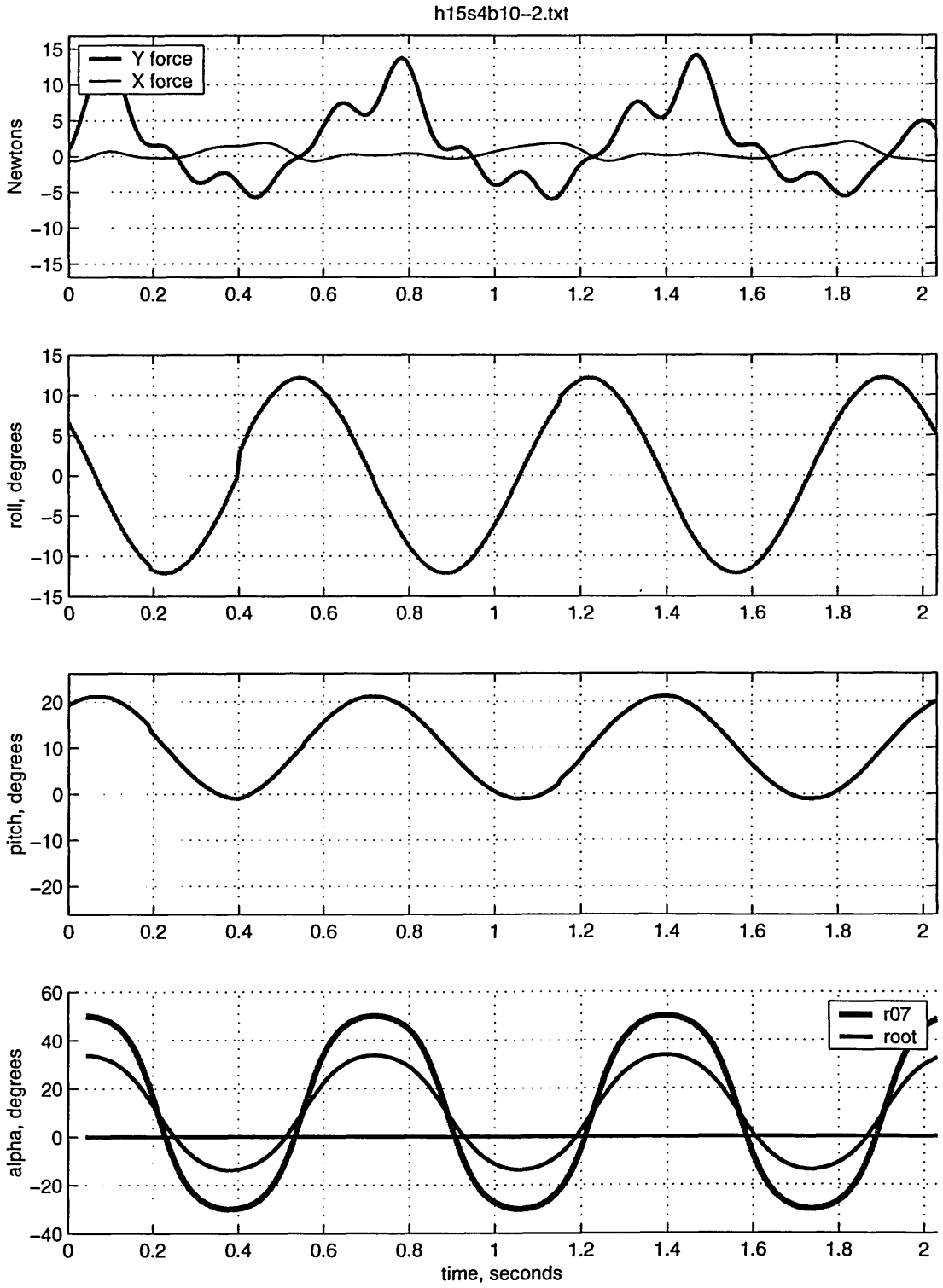

Figure B-1: $h_{0.7}/c = 1.5$, $St = 0.40$, $bias = 10°$

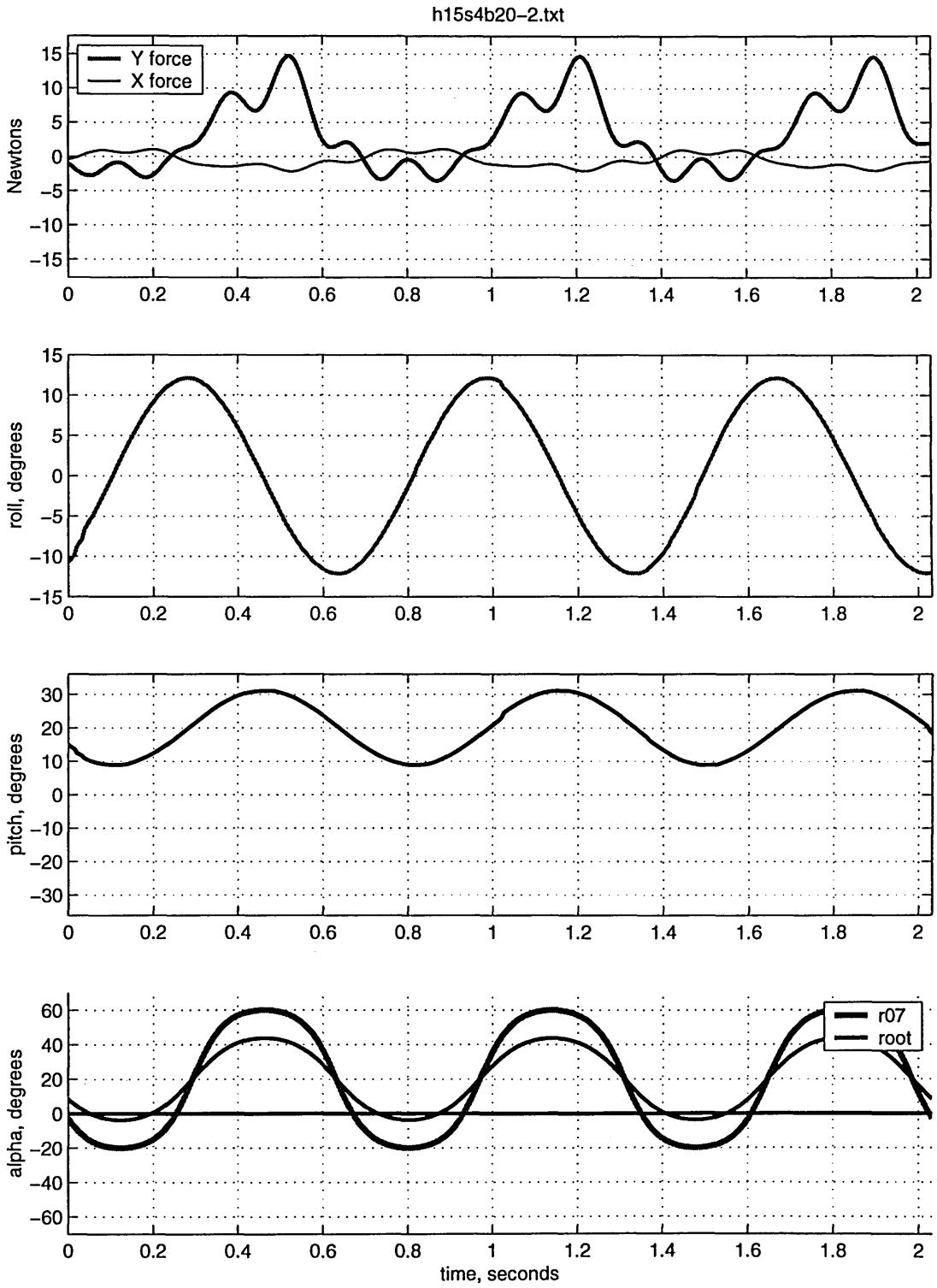

Figure B-2: $h_{0.7}/c = 1.5$, $St = 0.40$, $bias = 20°$

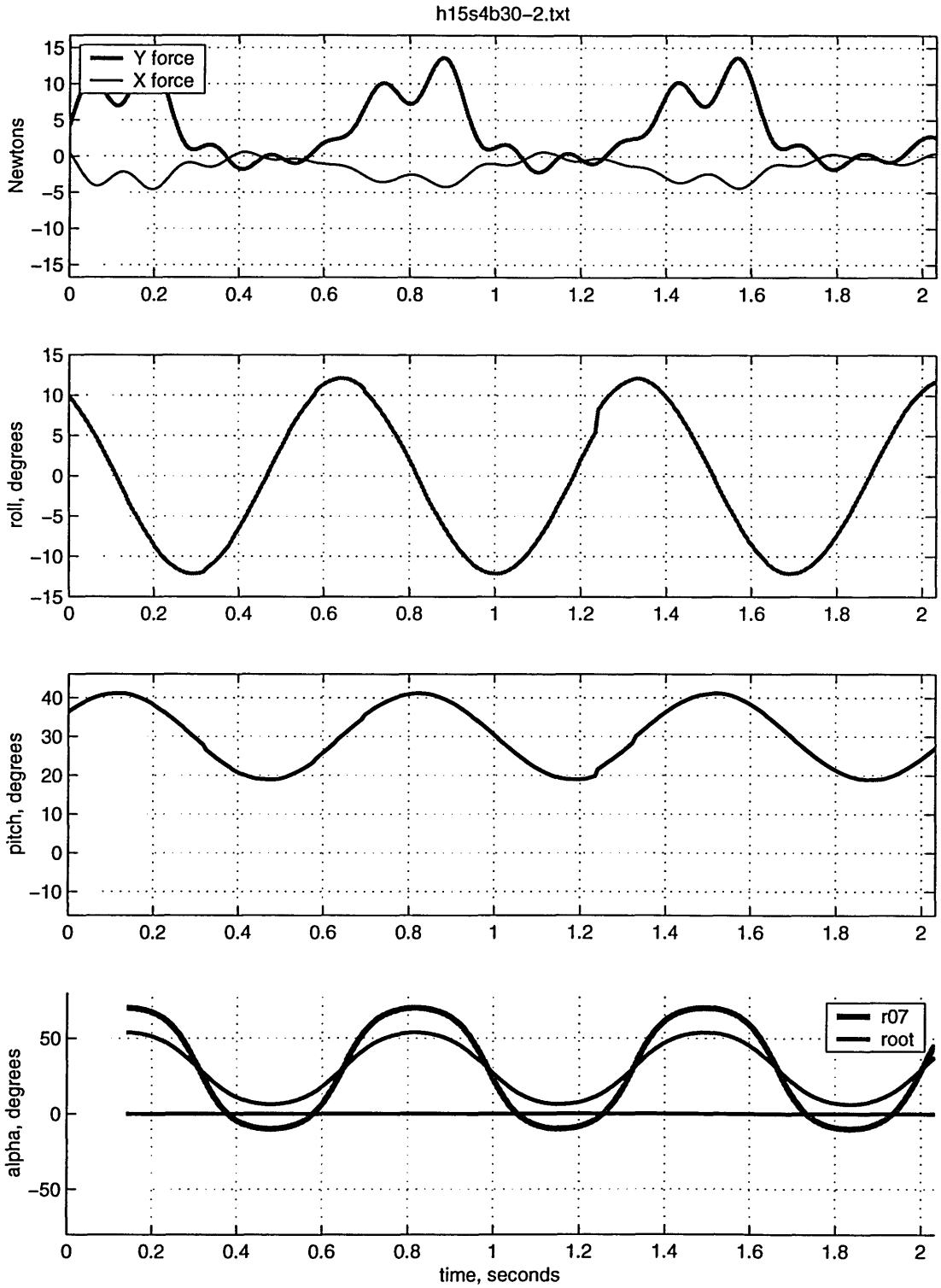

Figure B-3: $h_{0.7}/c = 1.5$, $St = 0.40$, $bias = 30°$

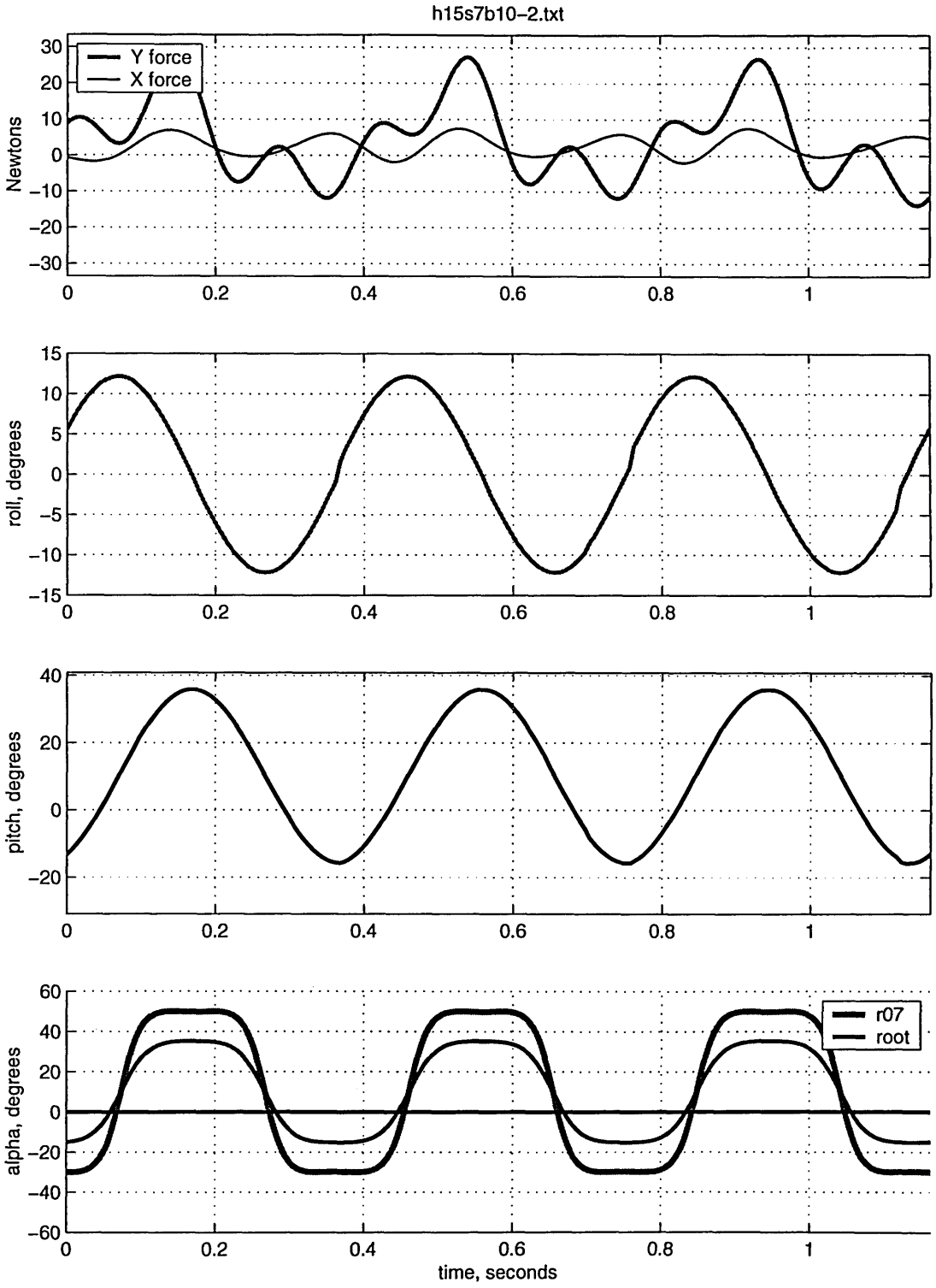

Figure B-4: $h_{0.7}/c = 1.5$, $St = 0.70$, $bias = 10°$

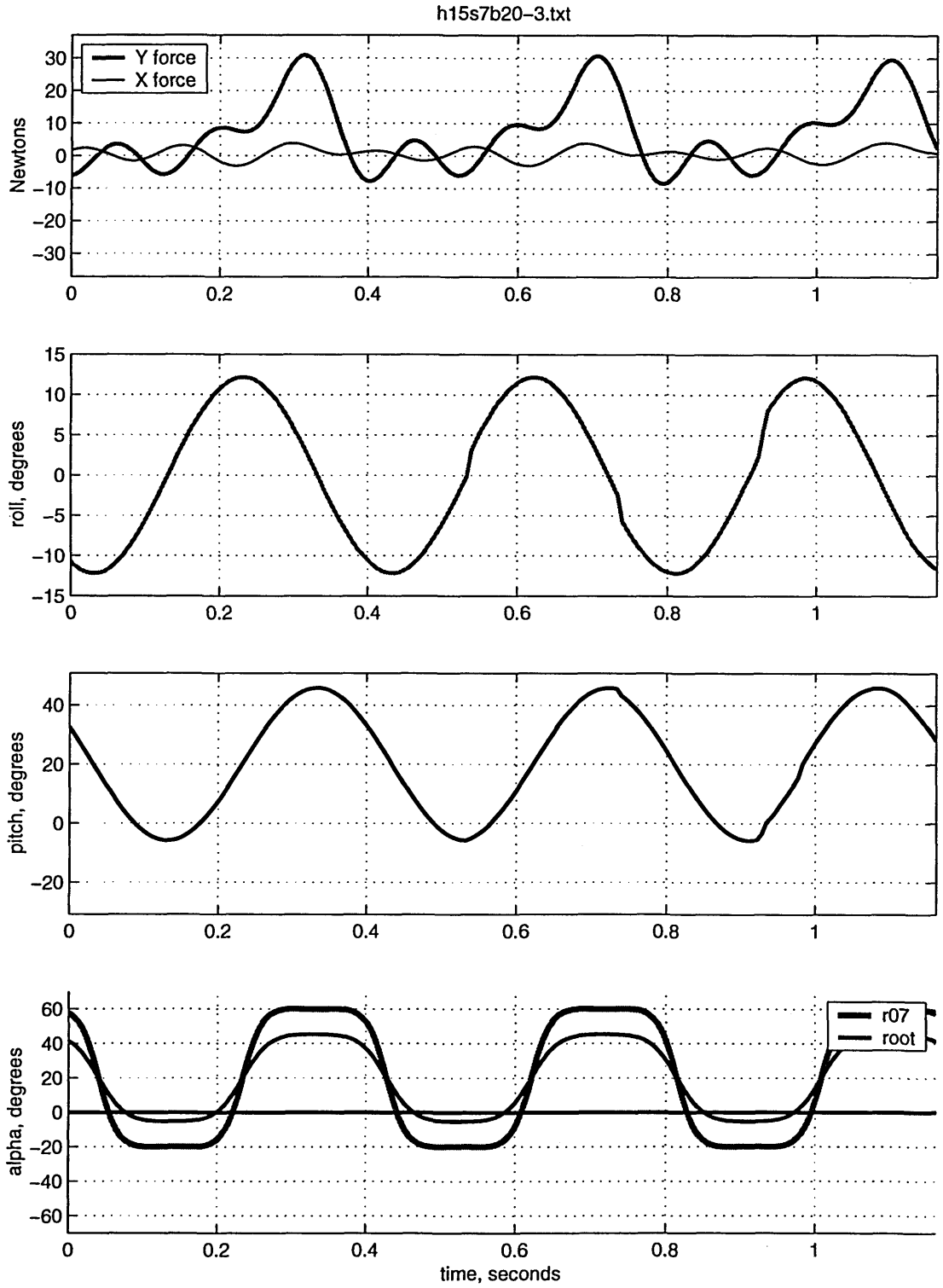

Figure B-5: $h_{0.7}/c = 1.5$, $St = 0.70$, $bias = 20°$

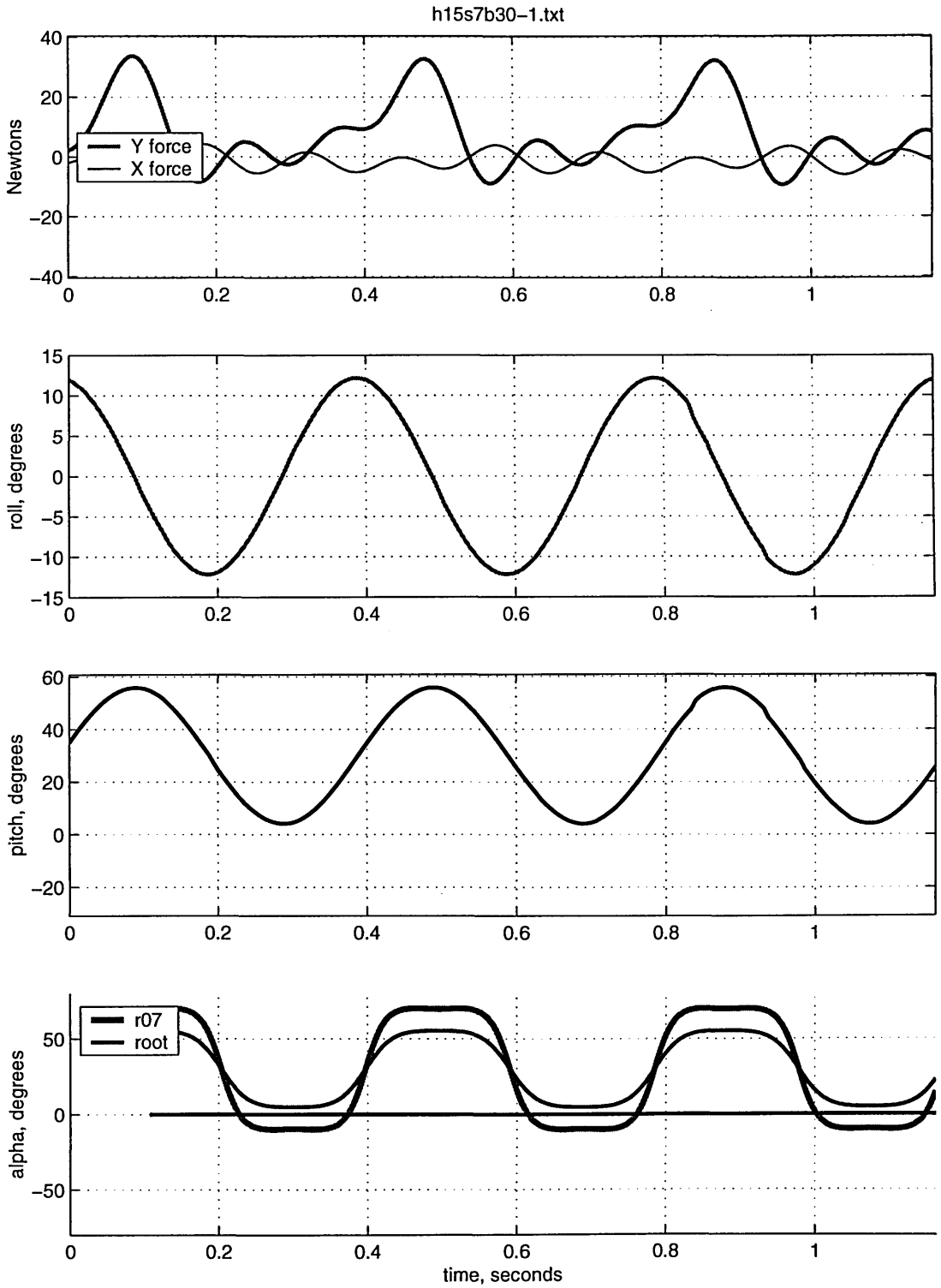

Figure B-6: $h_{0.7}/c = 1.5$, $St = 0.70$, $bias = 30°$

Appendix C

Impulse Start Time Data

In the following figures we show data from selected impulse start experiments. The X and Y force traces have been filtered using a perfect low-pass filter with a cut-off frequency of 3 times the fundamental driving frequency f. The data used to calculate the impulse was filtered.

We show the four data traces recorded by the two different computers during an experiment. The time traces show the filtered X and Y force data as well as the pitch and roll position from the recorded encoder feedback. The two data sets, forces and positions, were linked using the pulse signal as a marker. The pulse signal is not shown, but was used in processing to line up the data sets in time.

The following tables give all of the transient response specifications defined in the chapter for half and full-cycle motions, X and Y forces in still water.

$T(sec)$	$\theta_o(deg)$	$J_X(Ns)$	$M_p(\%)$	$F_{Xmax}(N)$	$t_r(sec)$	$t_p(sec)$	$t_s(sec)$
0.40	30	0.937	10.551	11.588	0.0780	0.1220	0.1520
0.40	40	1.069	8.523	12.423	0.0850	0.1290	0.1530
0.40	50	1.075	6.262	11.411	0.0960	0.1390	0.1510
0.40	60	0.958	7.774	9.373	0.1100	0.1560	0.1770
0.40	70	0.828	9.141	7.596	0.1240	0.1720	0.1970
0.70	30	0.487	6.063	2.760	0.1710	0.2590	0.2640
0.70	40	0.538	10.417	2.965	0.1810	0.2810	0.3600
0.70	50	0.594	3.388	2.878	0.2070	0.2940	0.2980
0.70	60	0.562	6.938	2.697	0.2110	0.3020	0.3060
0.70	70	0.490	10.147	2.451	0.2410	0.3310	0.3350
0.70	80	0.440	10.608	2.566	0.2880	0.3680	0.3720
0.70	90	0.302	24.097	2.780	0.3010	0.3790	0.4500
1.00	30	0.371	2.933	1.382	0.2620	0.3860	0.3860
1.00	40	0.373	5.717	1.407	0.2570	0.3960	0.3960
1.00	50	0.384	10.376	1.390	0.2710	0.4270	0.5190
1.00	60	0.406	6.310	1.338	0.3070	0.4450	0.4450
1.00	70	0.357	9.147	1.248	0.3450	0.4750	0.5150
1.00	80	0.289	6.136	1.148	0.4400	0.5450	0.5450
1.00	90	0.223	10.112	1.344	0.4840	0.5750	0.6030

Table C.1: Transient response specification for half-cycle impulsive start in still water, X direction

$T(sec)$	$\theta_o(deg)$	$J_Y(Ns)$	$M_p(\%)$	$F_{Ymax}(N)$	$t_r(sec)$	$t_p(sec)$	$t_s(sec)$
0.40	30	-0.839	128.106	10.401	0.1090	0.1830	0.6580
0.40	40	-0.663	135.274	8.111	0.1040	0.1840	0.7710
0.40	50	-0.525	130.609	6.003	0.0990	0.1830	0.7790
0.40	60	-0.339	158.283	4.466	0.0800	0.1790	1.0390
0.40	70	-0.297	128.149	3.329	0.0770	0.1790	0.6840
0.70	30	-0.495	116.921	3.193	0.1580	0.3090	0.6940
0.70	40	-0.312	181.520	2.816	0.1350	0.3160	1.3210
0.70	50	-0.274	164.466	2.153	0.1400	0.3310	1.3910
0.70	60	-0.195	198.435	1.875	0.1190	0.3330	1.3990
0.70	70	-0.174	160.544	1.504	0.1080	0.3320	1.3980
0.70	80	-0.121	212.538	1.429	0.1030	0.3790	0.9680
0.70	90	-0.104	171.311	1.249	0.0800	0.3490	0.6510
1.00	30	-0.247	203.912	1.710	0.1770	0.4480	1.3340
1.00	40	-0.205	198.951	1.487	0.1600	0.4340	1.3430
1.00	50	-0.253	117.099	1.085	0.2130	0.4560	1.3720
1.00	60	-0.146	195.614	1.148	0.1590	0.4590	1.3670
1.00	70	-0.061	360.250	0.878	0.0840	0.4620	1.4130
1.00	80	-0.031	649.333	0.772	0.0880	0.5720	1.6000
1.00	90	-0.053	311.524	0.692	0.1100	0.5560	1.7000

Table C.2: Transient response specification for half-cycle impulsive start in still water, Y direction

$T(sec)$	$\theta_o(deg)$	$J_X(Ns)$	$F_{Xmax}(N)$	$t_r(sec)$	$t_s(sec)$
0.40	30	2.056	11.145	0.2670	0.2820
0.40	40	2.212	11.733	0.2740	0.2890
0.70	30	1.045	2.819	0.4960	0.5220
0.70	40	1.149	2.922	0.5120	0.5370
0.70	50	1.125	2.836	0.5160	0.5390
0.70	60	1.091	2.479	0.5530	0.5820
0.70	70	0.932	2.763	0.5520	0.5690
0.70	80	0.698	2.962	0.5880	0.6000
1.00	30	0.778	1.433	0.7030	0.7380
1.00	40	0.852	1.519	0.7190	0.7530
1.00	50	0.863	1.451	0.7440	0.7800
1.00	60	0.742	1.273	0.7550	0.7860
1.00	70	0.665	1.899	0.7990	0.8150
1.00	80	0.489	1.459	0.8440	0.8590
1.00	90	0.382	1.635	0.9030	0.9130

Table C.3: Transient response specification for full-cycle impulsive start in still water, X direction

$T(sec)$	$\theta_o(deg)$	$J_Y(Ns)$	$M_p(\%)$	$F_{Ymax}(N)$	$t_p(sec)$	$t_s(sec)$
0.40	30	0.201	-1073.803	19.512	0.2810	0.8450
0.40	40	0.059	-2922.742	15.615	0.2530	1.4610
0.70	30	-0.019	5530.334	6.552	0.4040	1.7990
0.70	40	0.033	-2935.270	5.377	0.4210	1.6650
0.70	50	0.095	-873.103	4.402	0.4240	1.4200
0.70	60	-0.042	1320.782	3.392	0.4260	1.8840
0.70	70	-0.122	283.835	2.463	0.3250	1.7400
0.70	80	-0.127	193.389	1.872	0.3570	1.7640
1.00	30	0.042	-1934.438	3.381	0.4870	1.9370
1.00	40	0.000	-1946.116	2.539	0.4950	1.8710
1.00	50	-0.028	1927.542	2.119	0.5720	1.9950
1.00	60	-0.050	799.861	0.0870	0.5070	1.5860
1.00	70	-0.099	267.907	0.0910	0.4590	1.8520
1.00	80	-0.198	50.975	0.3470	0.5060	2.0400
1.00	90	-0.175	30.407	0.805	0.4970	2.1700

Table C.4: Transient response specification for full-cycle impulsive start in still water, Y direction

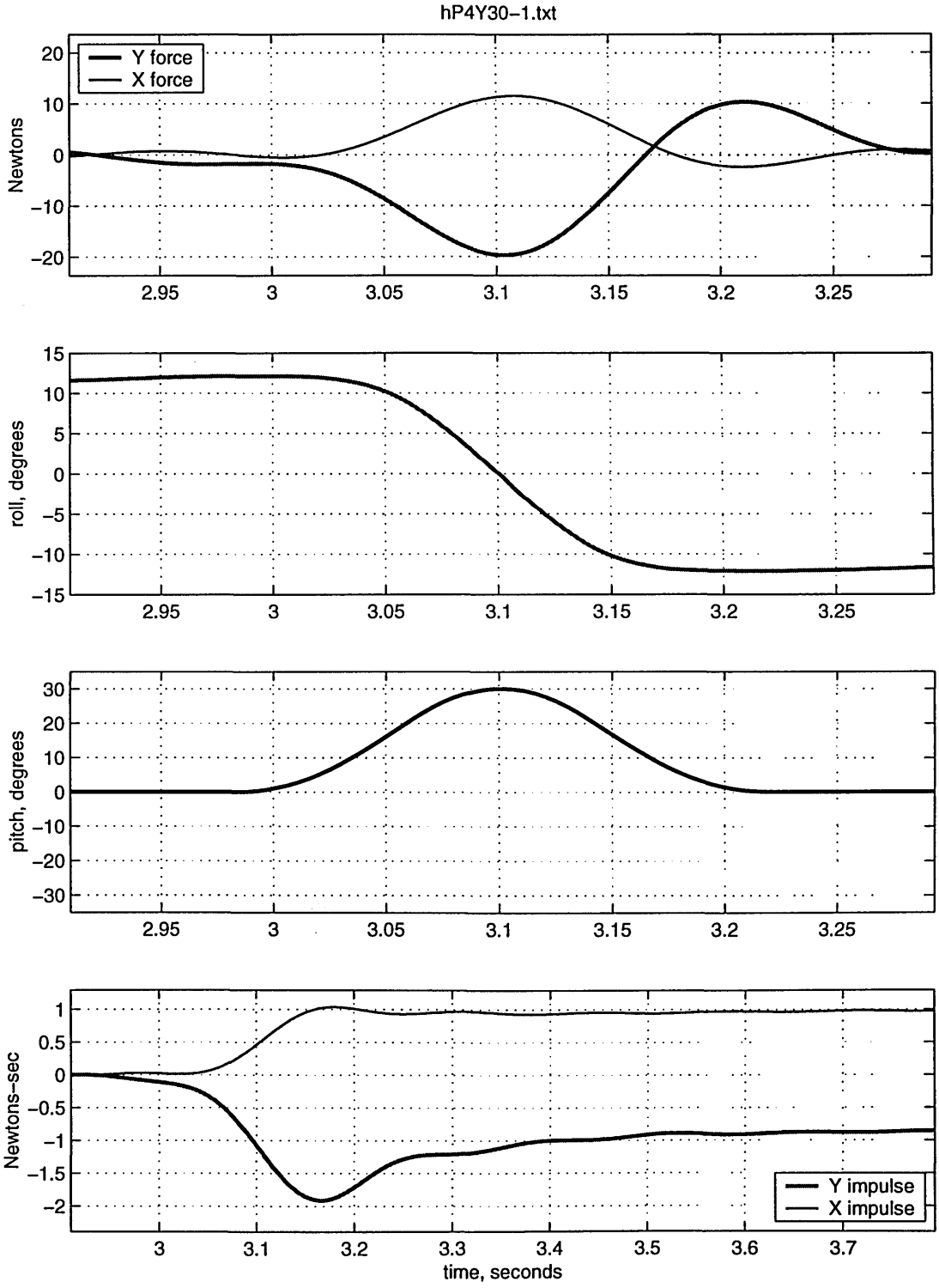

Figure C-1: Half-cycle, $U = 0\ m/s$, *Max. Roll Velocity* = 1.28 m/s, $\theta_o = 30°$

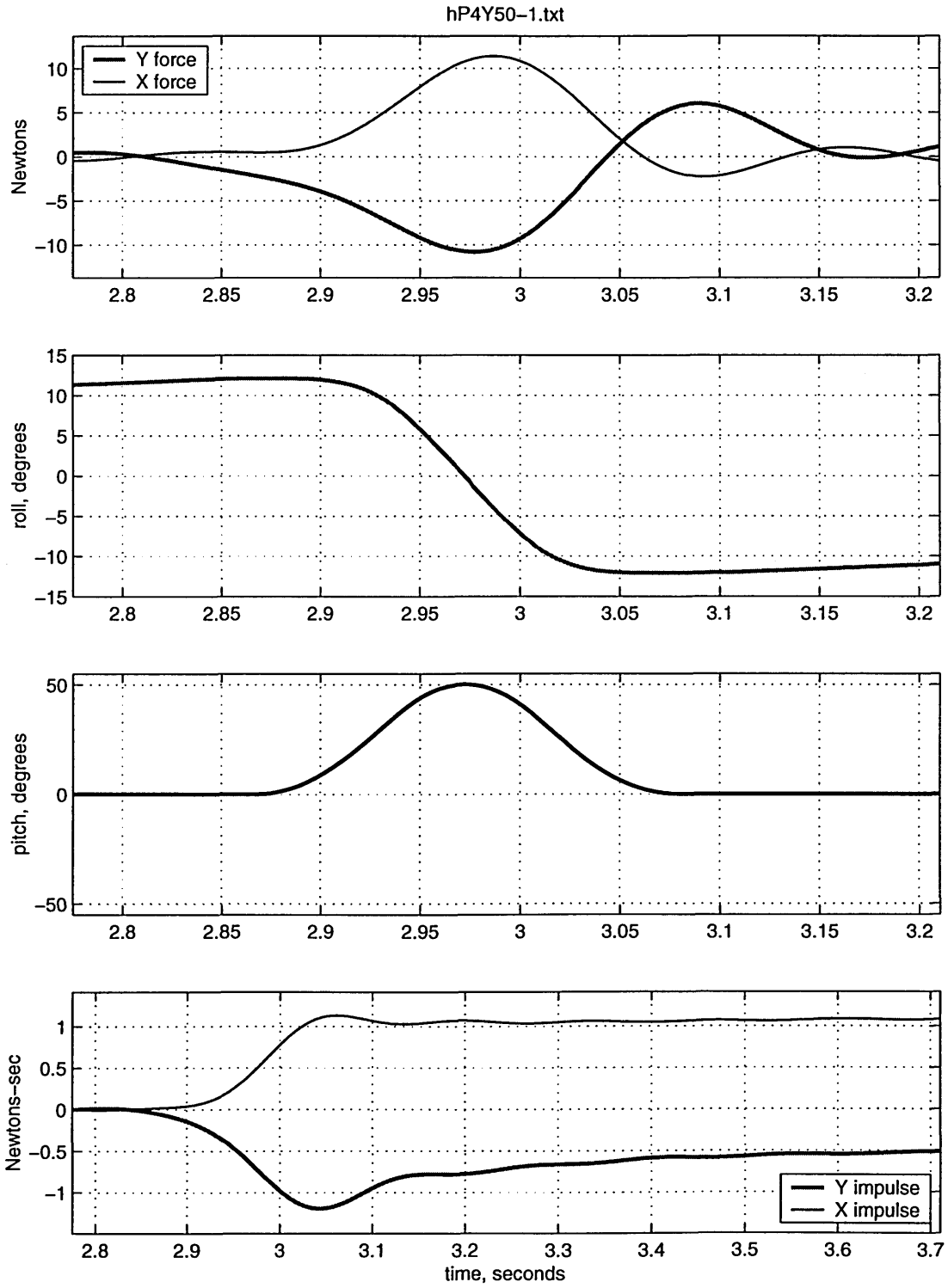

Figure C-2: Half-cycle, $U = 0\ m/s$, *Max. Roll Velocity* = 1.28 m/s, $\theta_o = 50°$

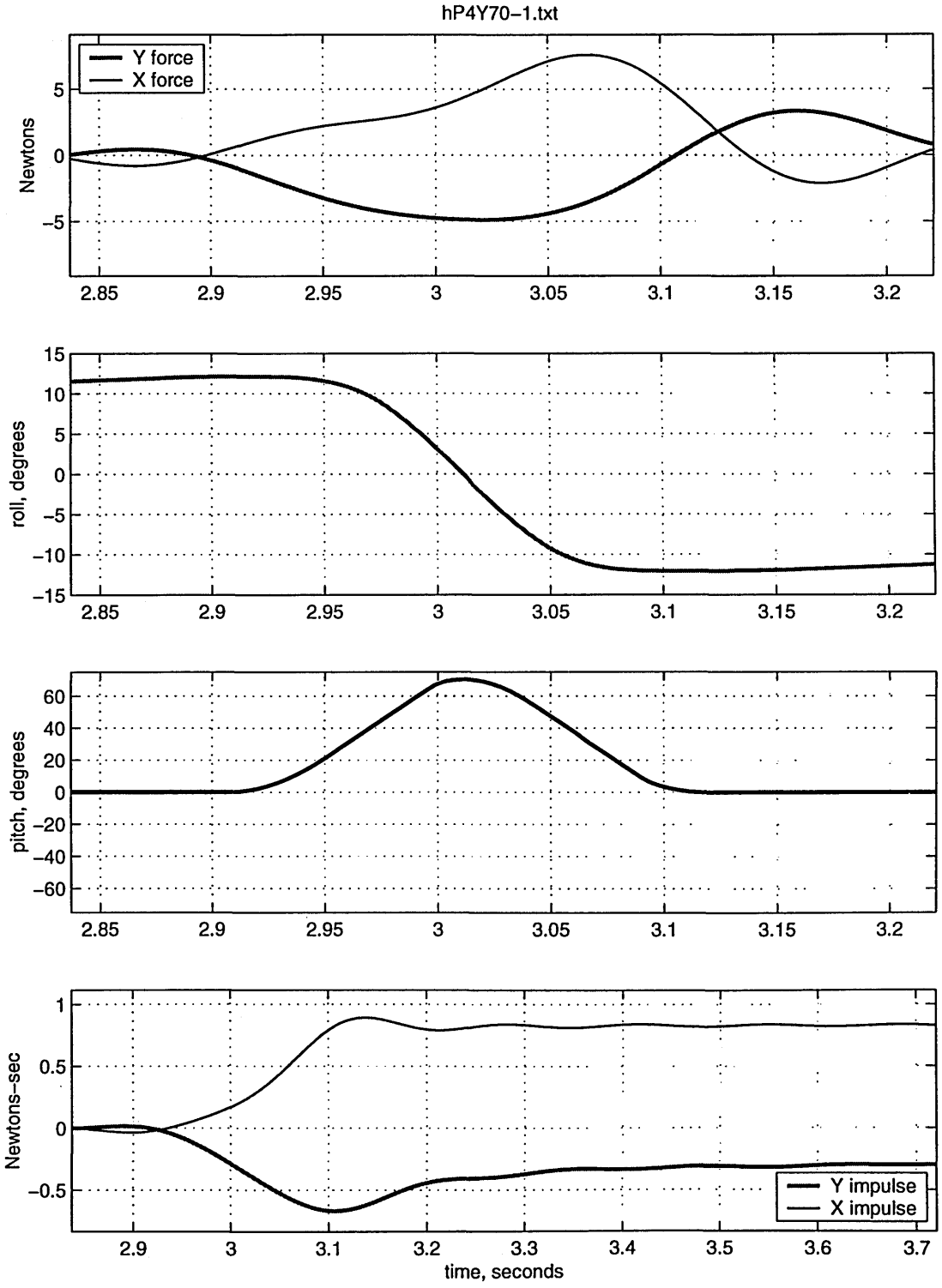

Figure C-3: Half-cycle, $U = 0\ m/s$, *Max. Roll Velocity* = 1.28 m/s, $\theta_o = 70°$

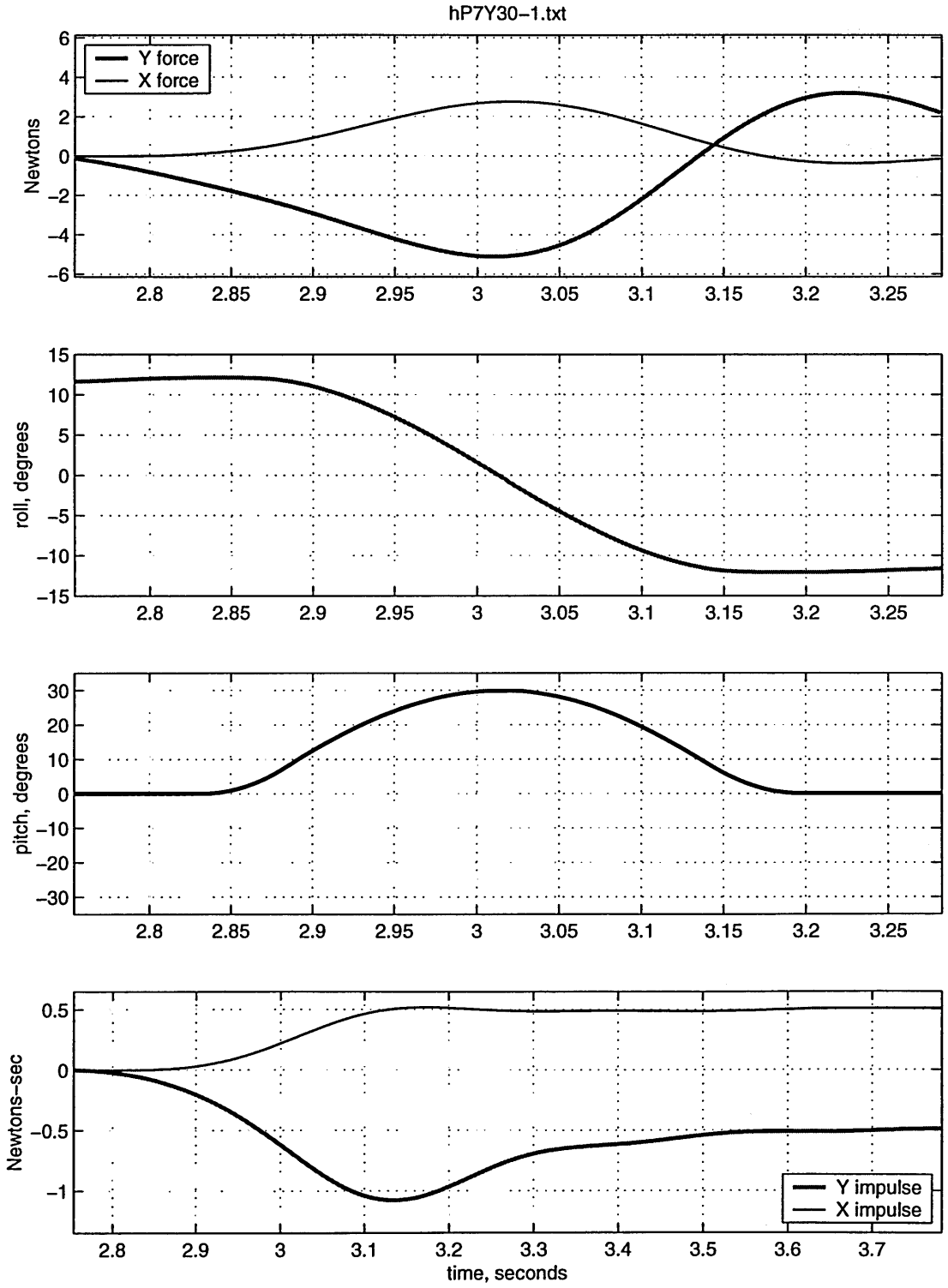

Figure C-4: Half-cycle, $U = 0\ m/s$, *Max. Roll Velocity* = 0.72 m/s, $\theta_o = 30°$

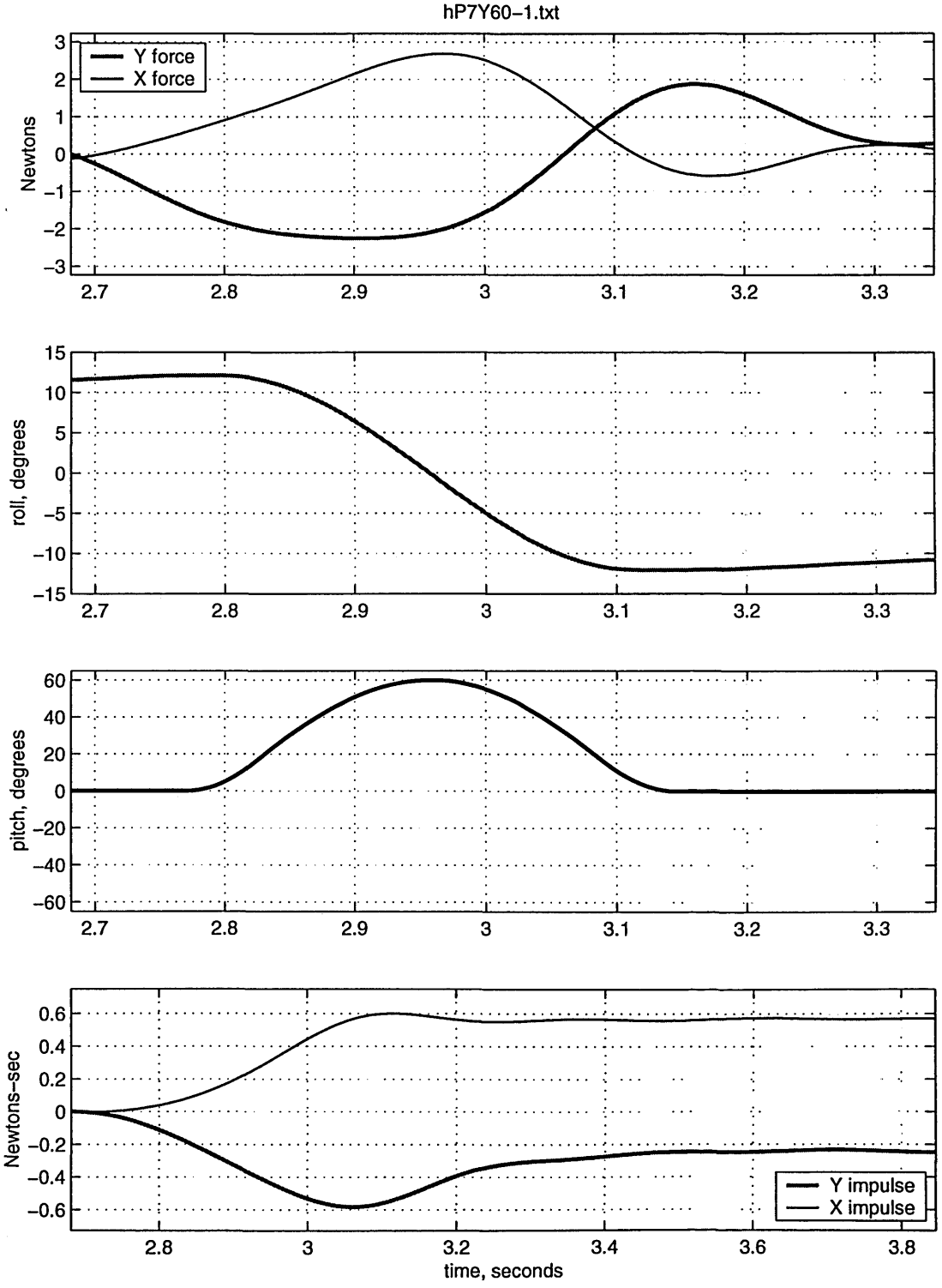

Figure C-5: Half-cycle, $U = 0\ m/s$, *Max. Roll Velocity* = 0.72 m/s, $\theta_o = 60°$

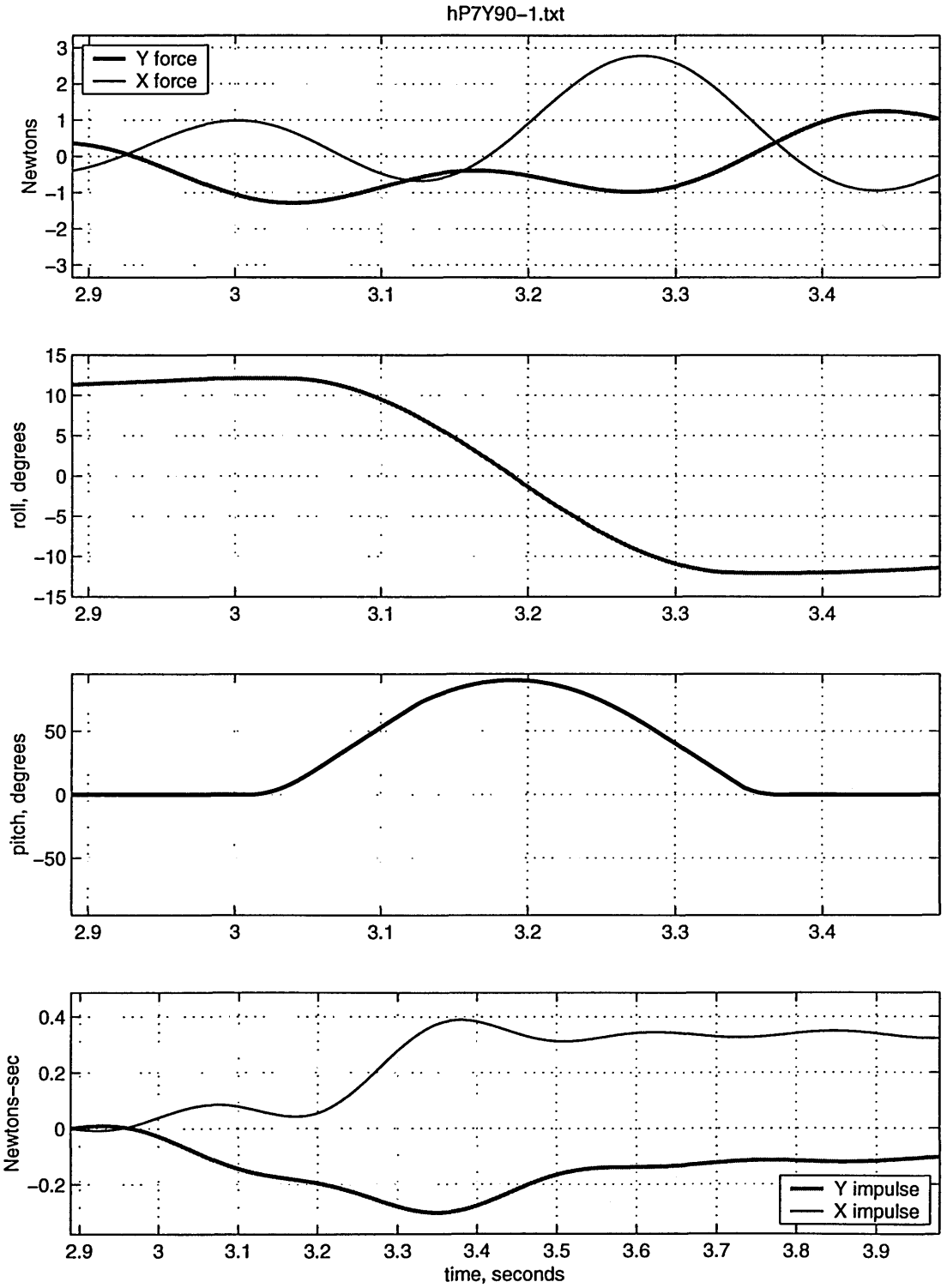

Figure C-6: Half-cycle, $U = 0\ m/s$, *Max. Roll Velocity* = 0.72 m/s, $\theta_o = 90°$

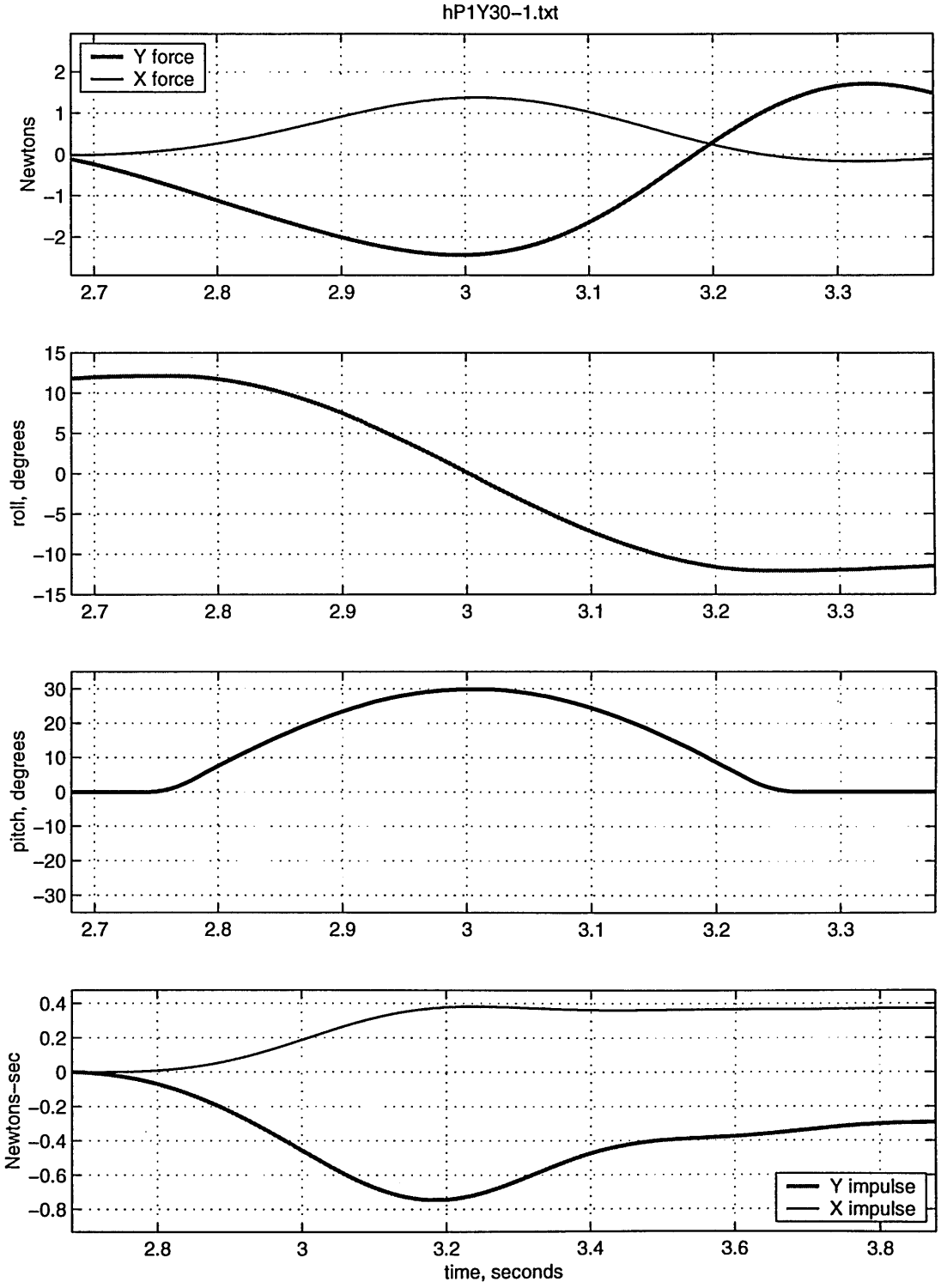

Figure C-7: Half-cycle, $U = 0\ m/s$, *Max. Roll Velocity* = 0.51 m/s, $\theta_o = 30°$

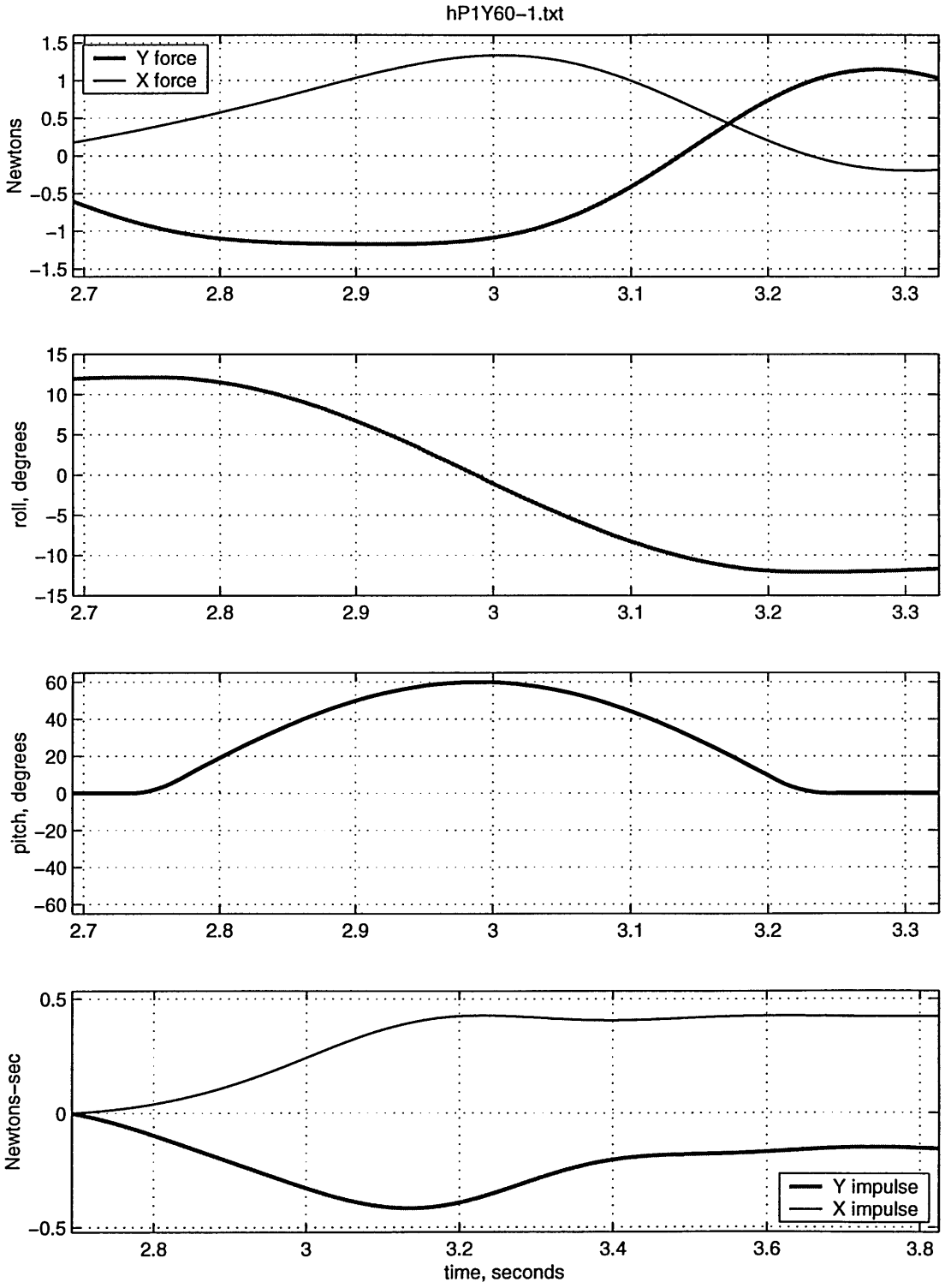

Figure C-8: Half-cycle, $U = 0\ m/s$, *Max. Roll Velocity* = 0.51 m/s, $\theta_o = 60°$

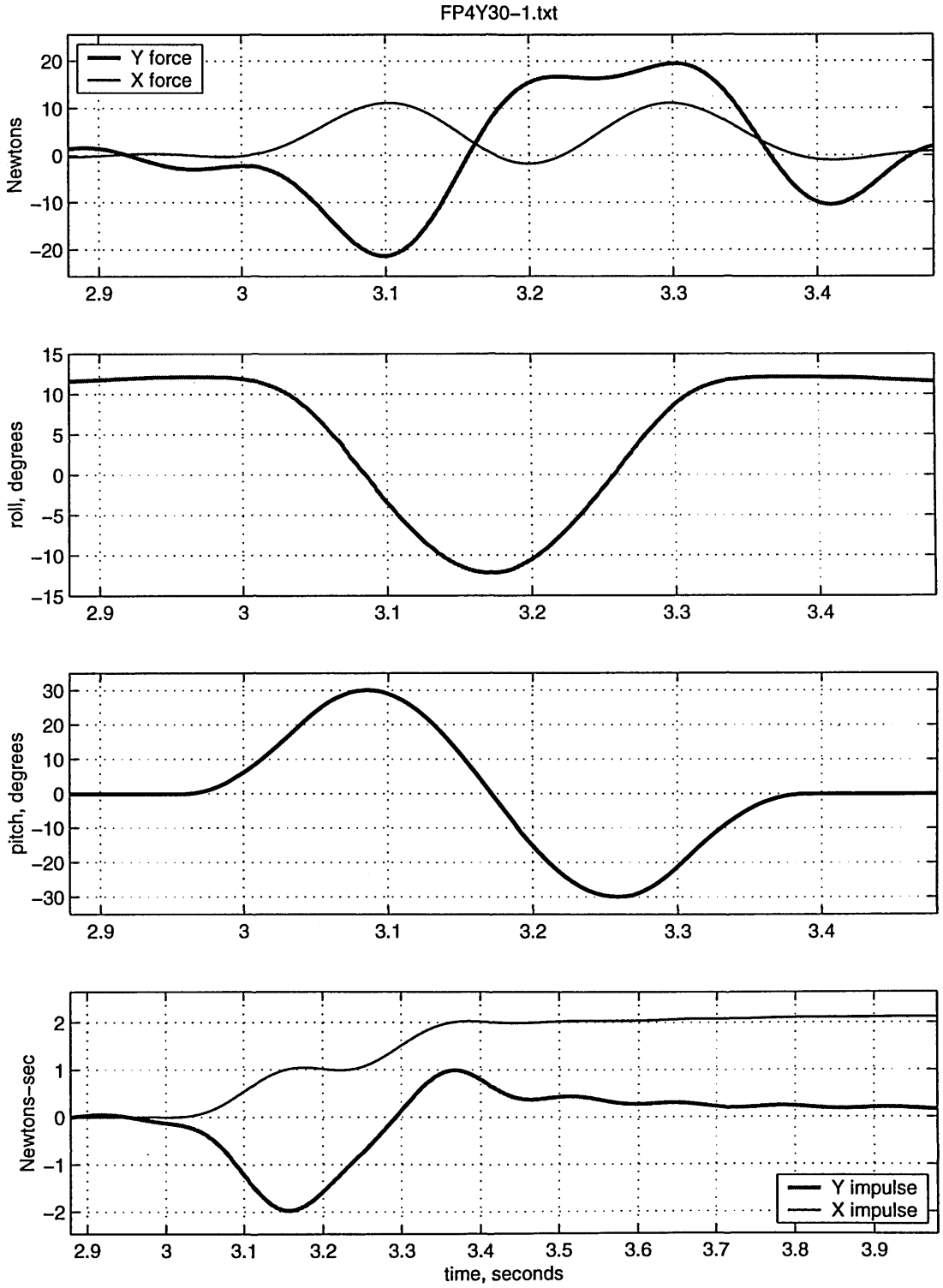

Figure C-9: Full-cycle, $U = 0\ m/s$, *Max. Roll Velocity* = 1.28 m/s, $\theta_o = 30°$

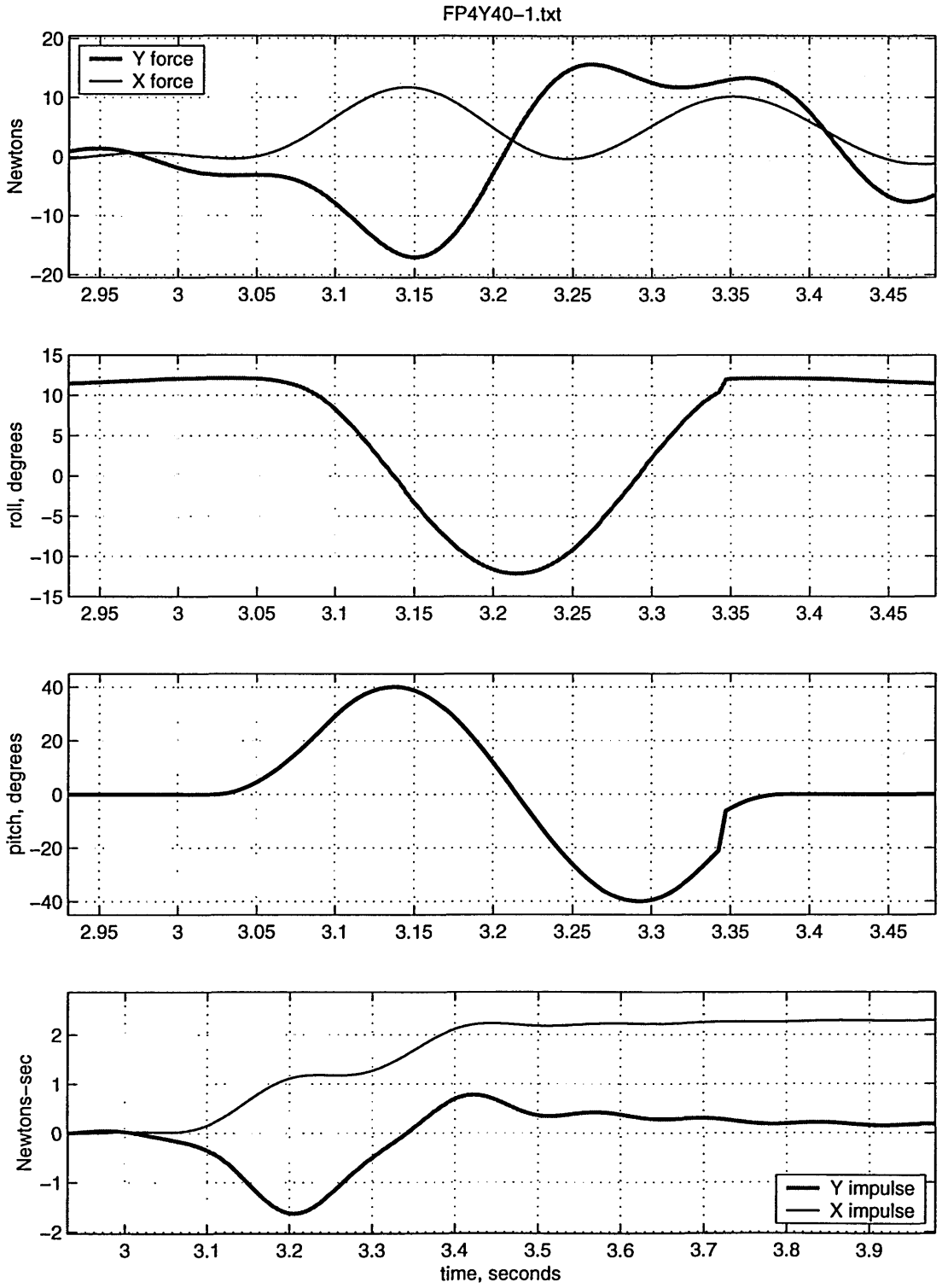

Figure C-10: Full-cycle, $U = 0\ m/s$, *Max. Roll Velocity* = 1.28 m/s, $\theta_o = 40°$

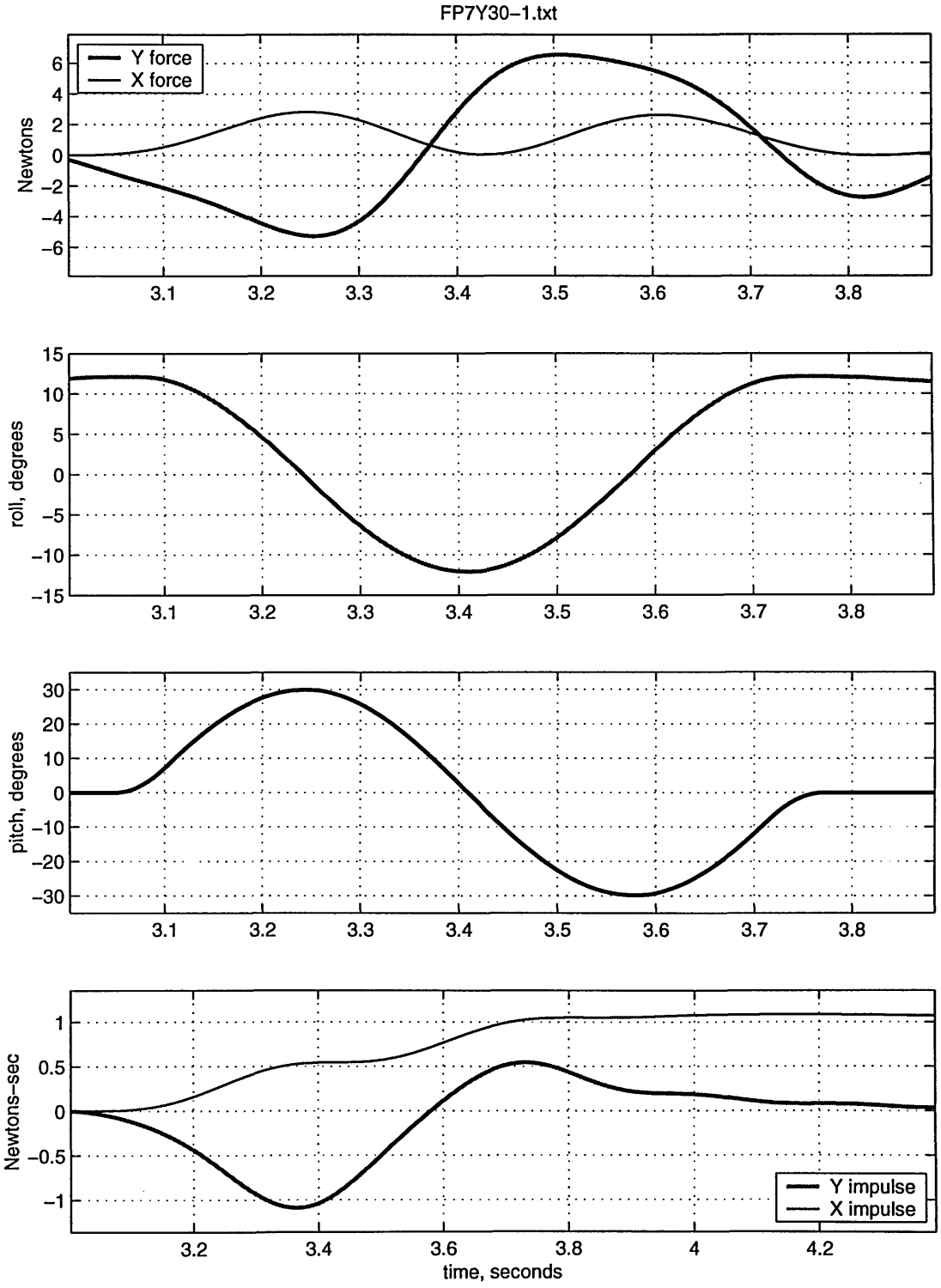

Figure C-11: Full-cycle, $U = 0\ m/s$, *Max. Roll Velocity* = 0.72 m/s, $\theta_o = 30°$

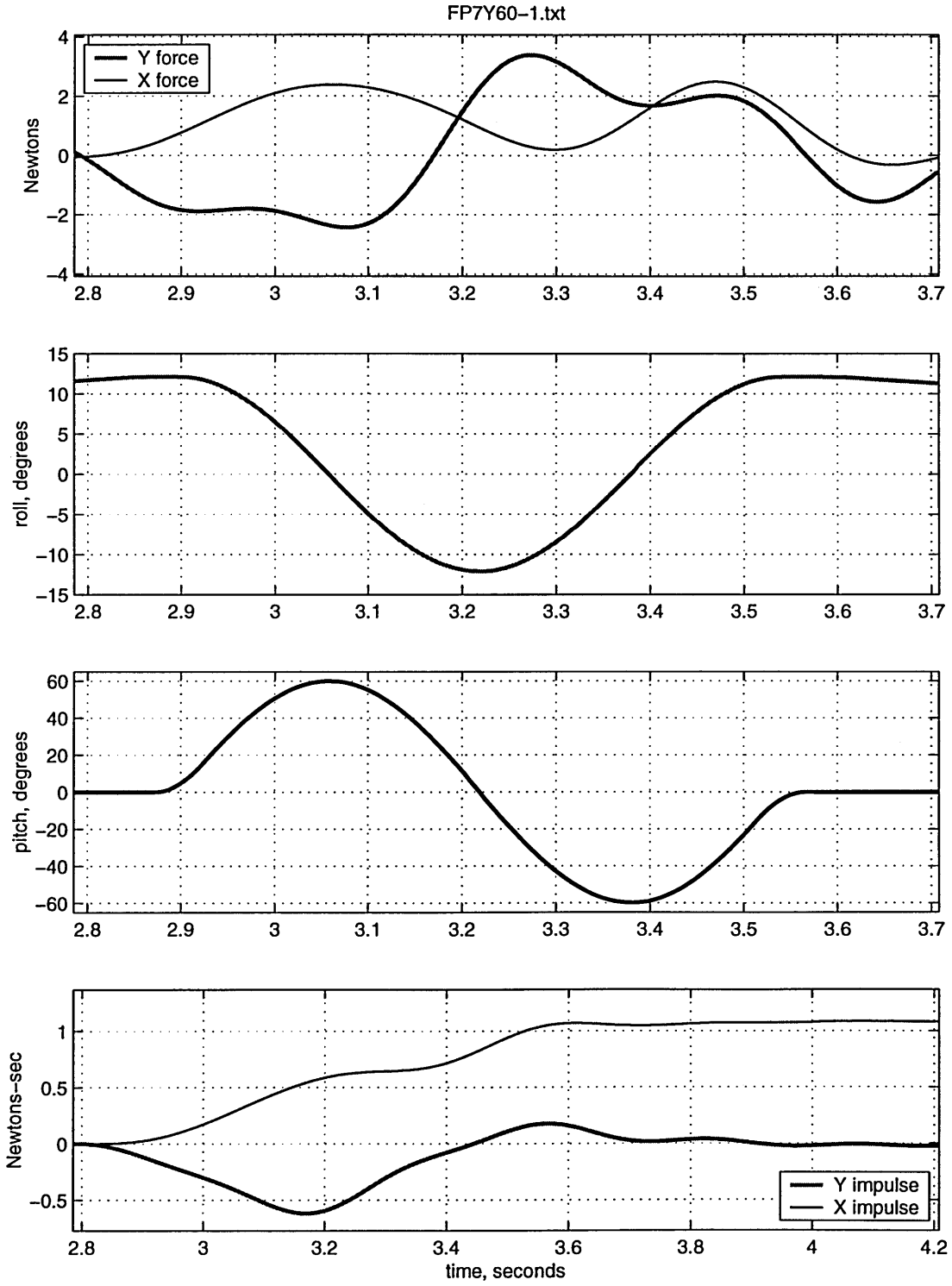

Figure C-12: Full-cycle, $U = 0\ m/s$, *Max. Roll Velocity* = 0.72 m/s, $\theta_o = 60°$

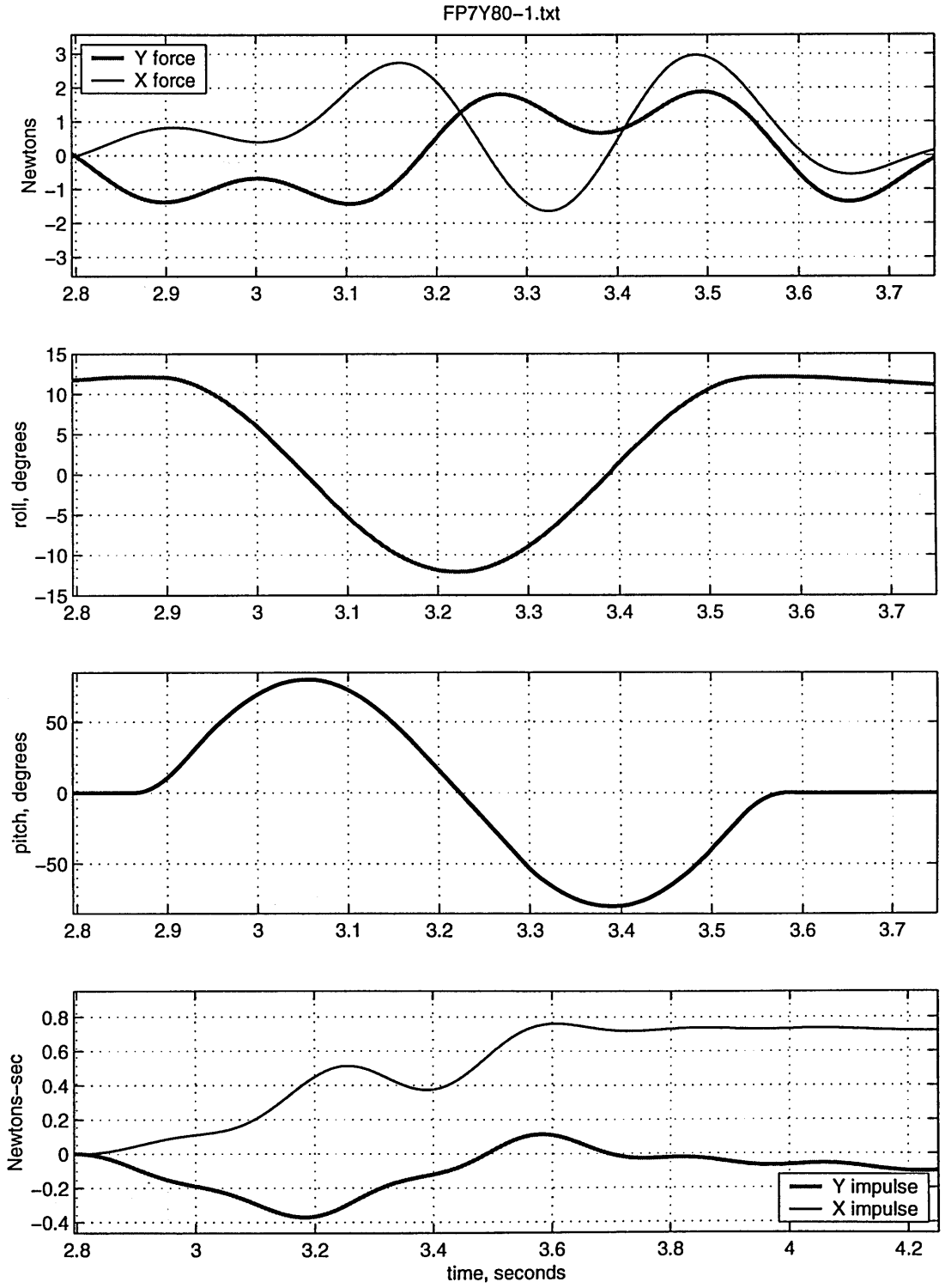

Figure C-13: Full-cycle, $U = 0\ m/s$, *Max. Roll Velocity* = 0.72 m/s, $\theta_o = 80°$

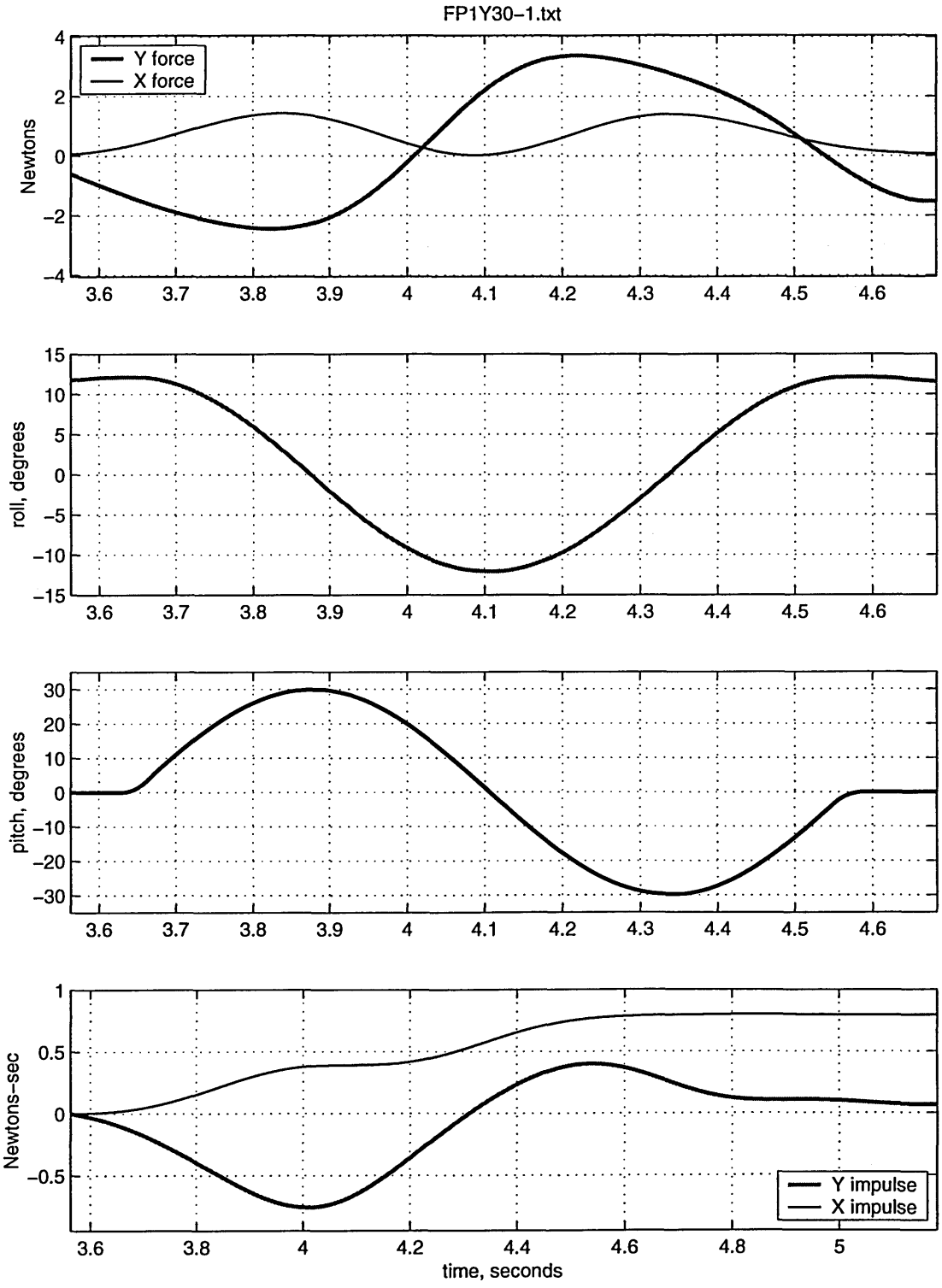

Figure C-14: Full-cycle, $U = 0\ m/s$, *Max. Roll Velocity* = 0.51 m/s, $\theta_o = 30°$

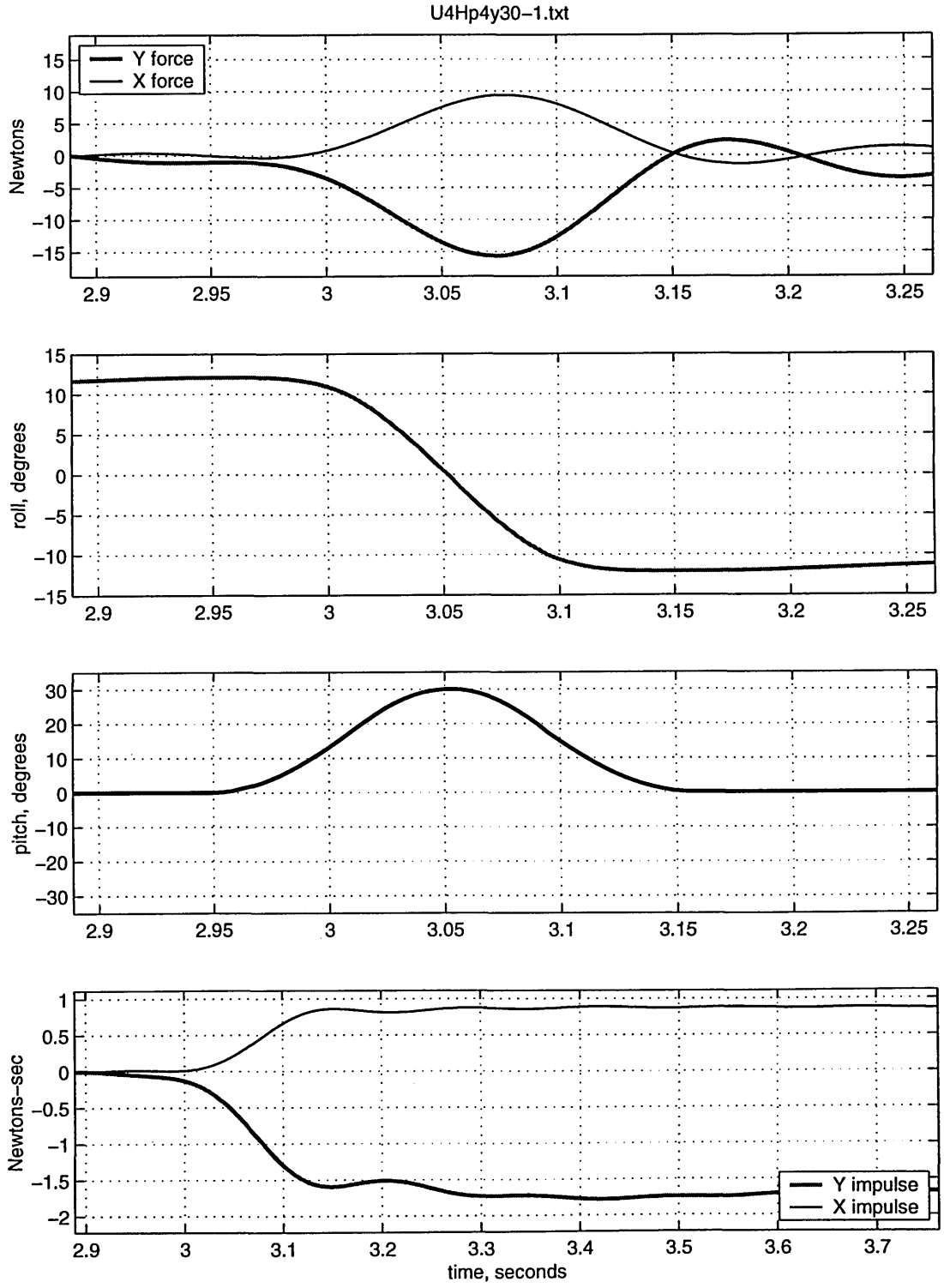

Figure C-16: Half-cycle, $U = 0.4\ m/s$, *Max. Roll Velocity* = 1.28 m/s, $\theta_o = 30°$

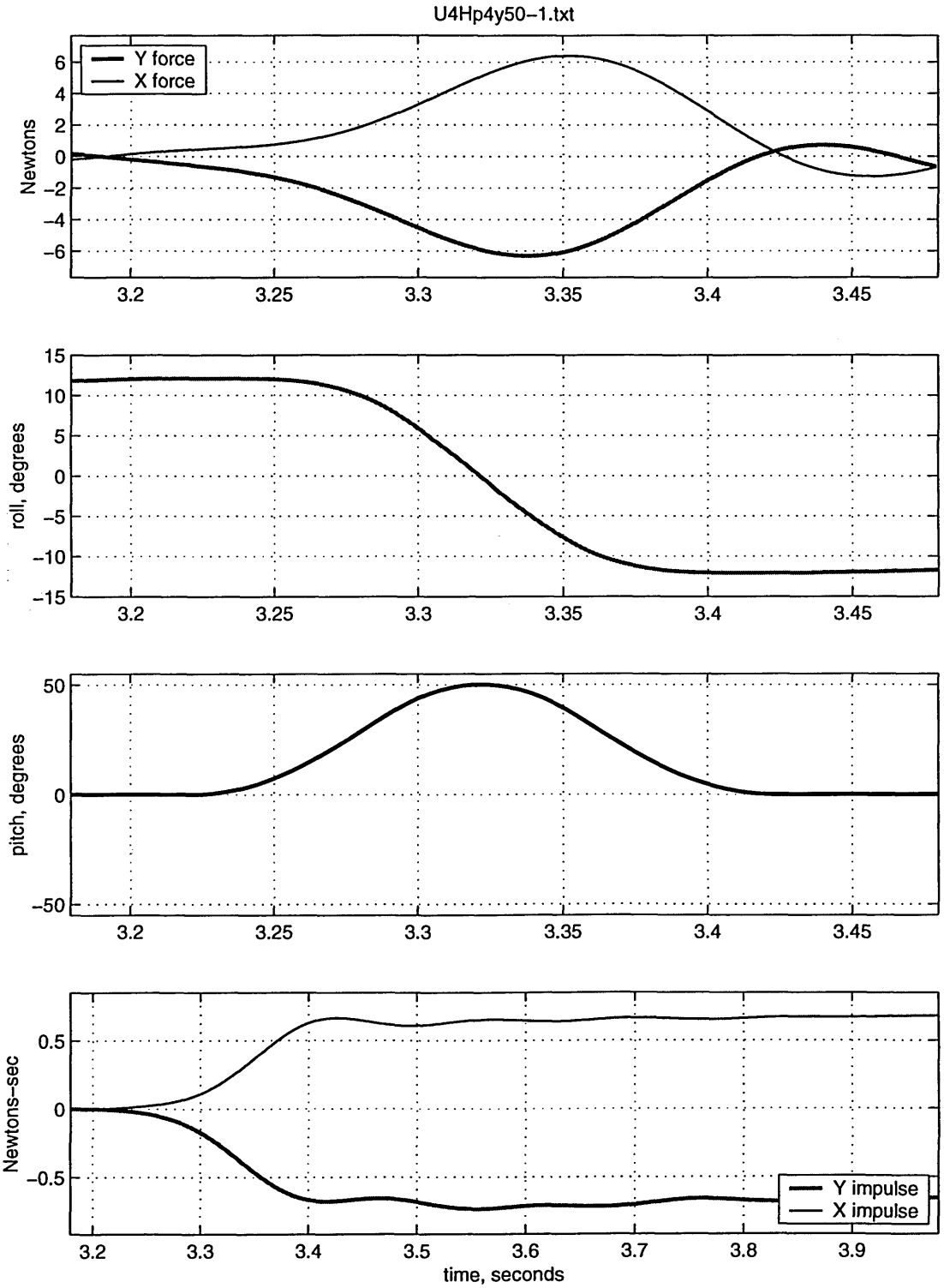

Figure C-17: Half-cycle, $U = 0.4\ m/s$, *Max. Roll Velocity* = 1.28 m/s, $\theta_o = 50°$

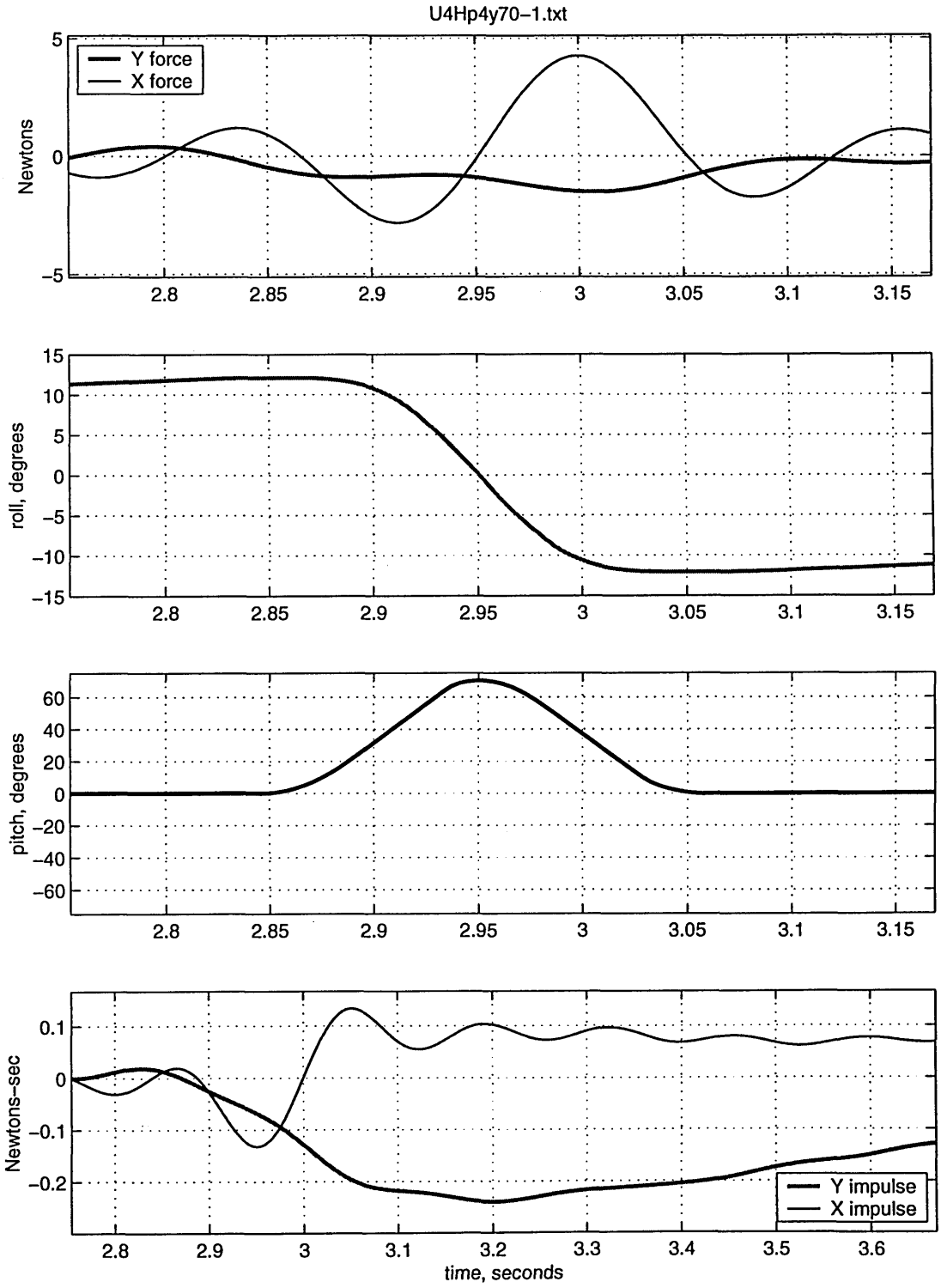

Figure C-18: Half-cycle, $U = 0.4\ m/s$, *Max. Roll Velocity* = 1.28 m/s, $\theta_o = 70°$

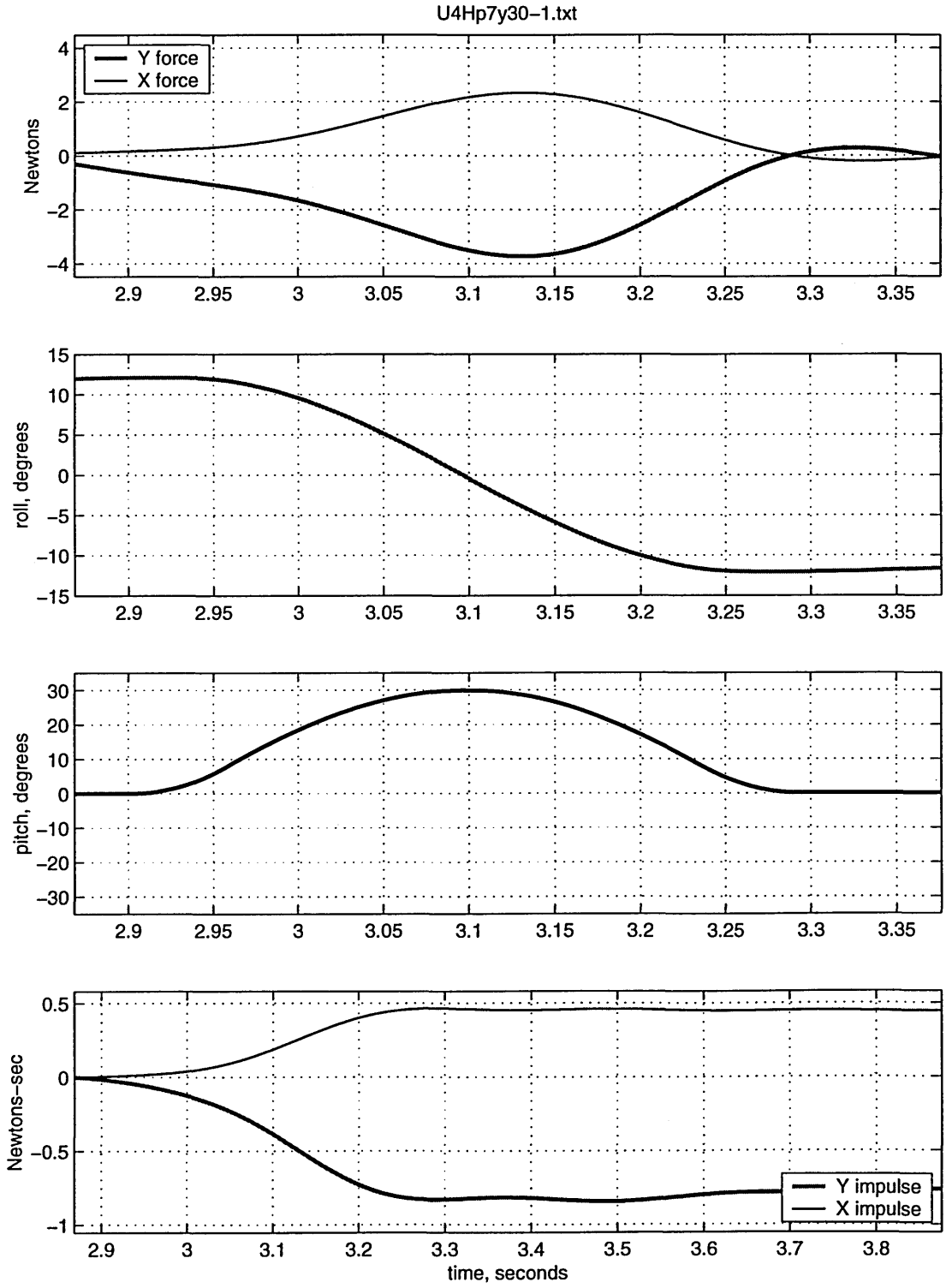

Figure C-19: Half-cycle, $U = 0.4\ m/s$, *Max. Roll Velocity* = 0.72 m/s, $\theta_o = 30°$

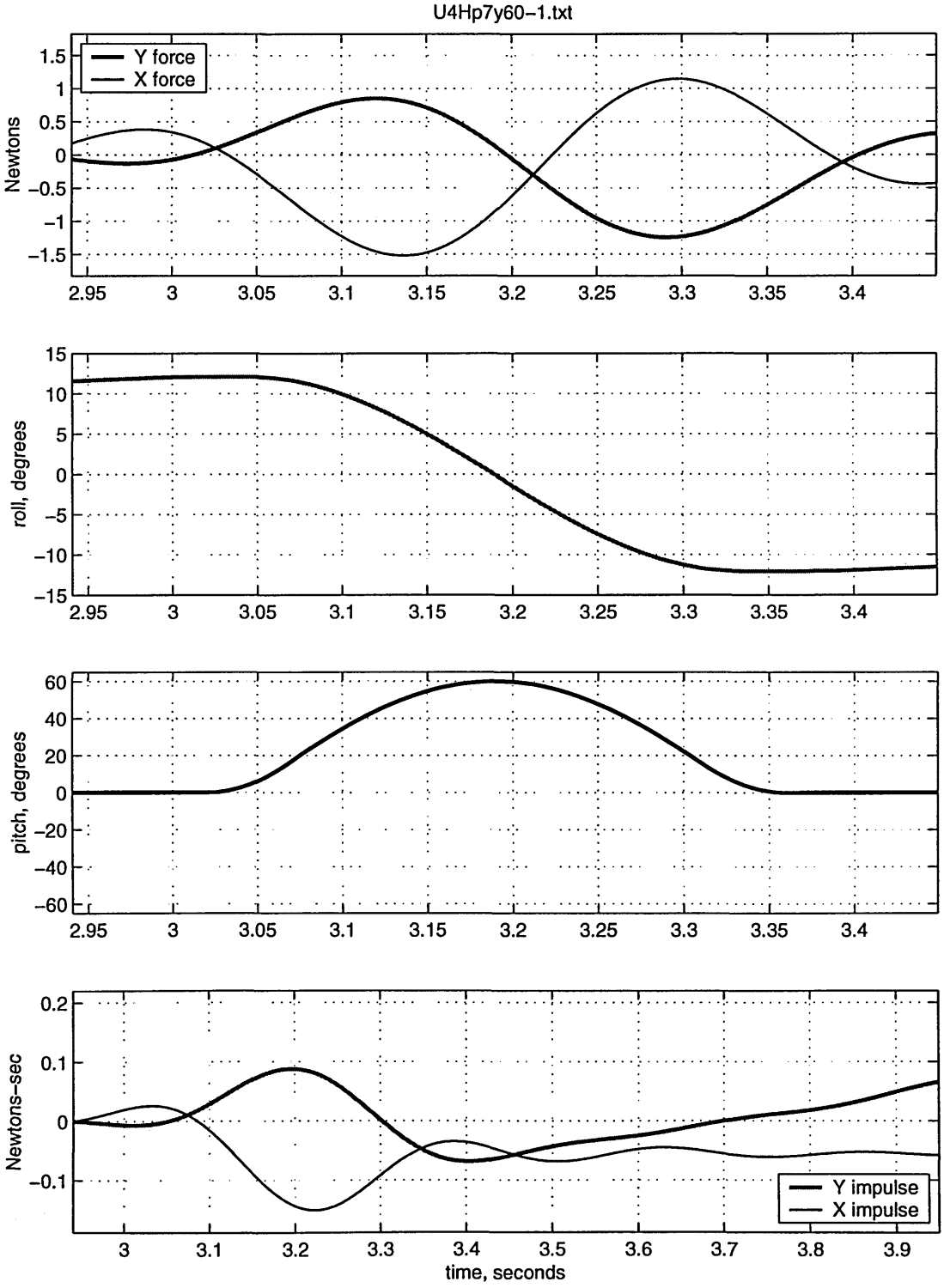

Figure C-20: Half-cycle, $U = 0.4\ m/s$, *Max. Roll Velocity* = 0.72 m/s, $\theta_o = 60°$

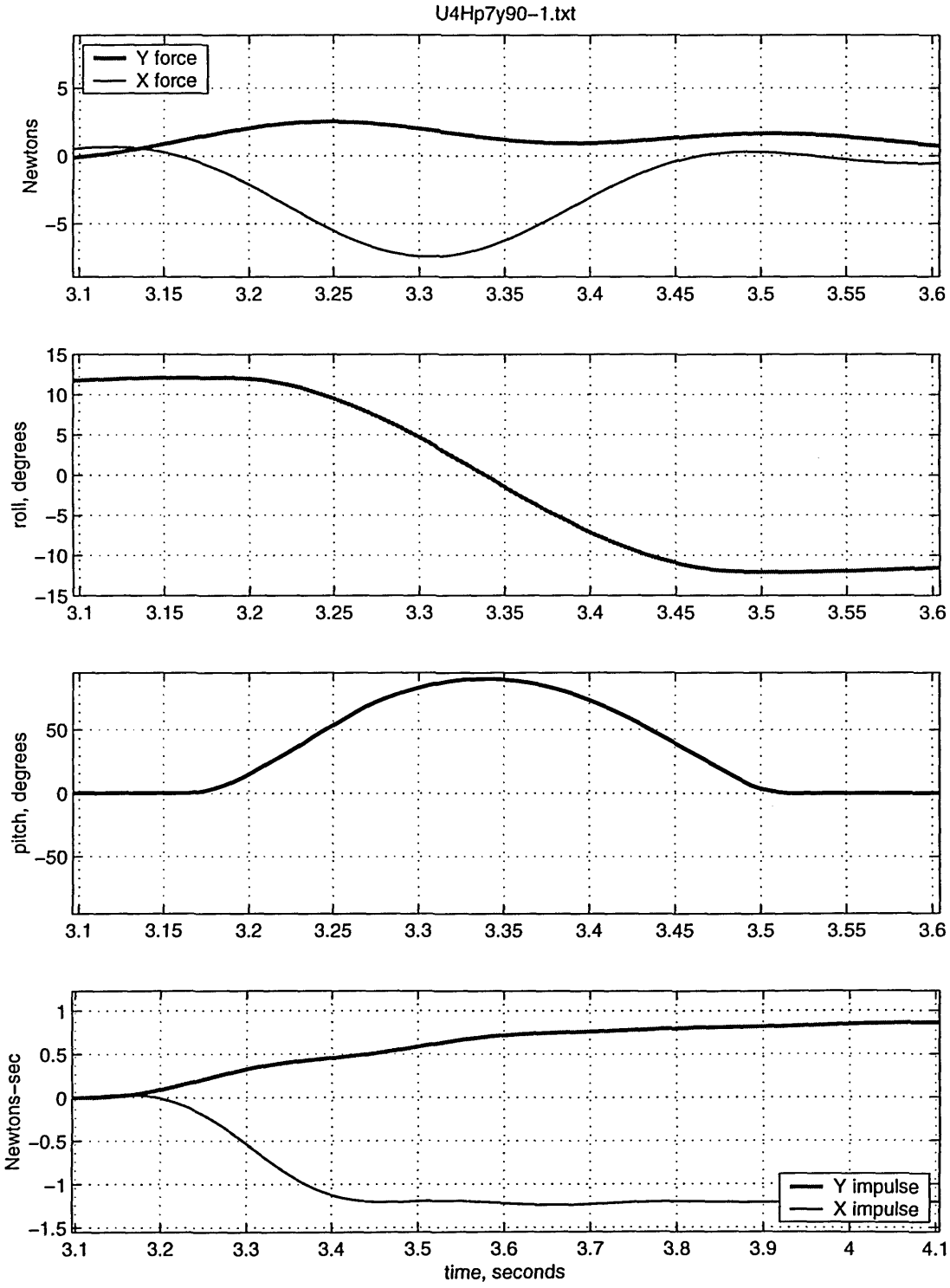

Figure C-21: Half-cycle, $U = 0.4\ m/s$, *Max. Roll Velocity* = 0.72 m/s, $\theta_o = 90°$

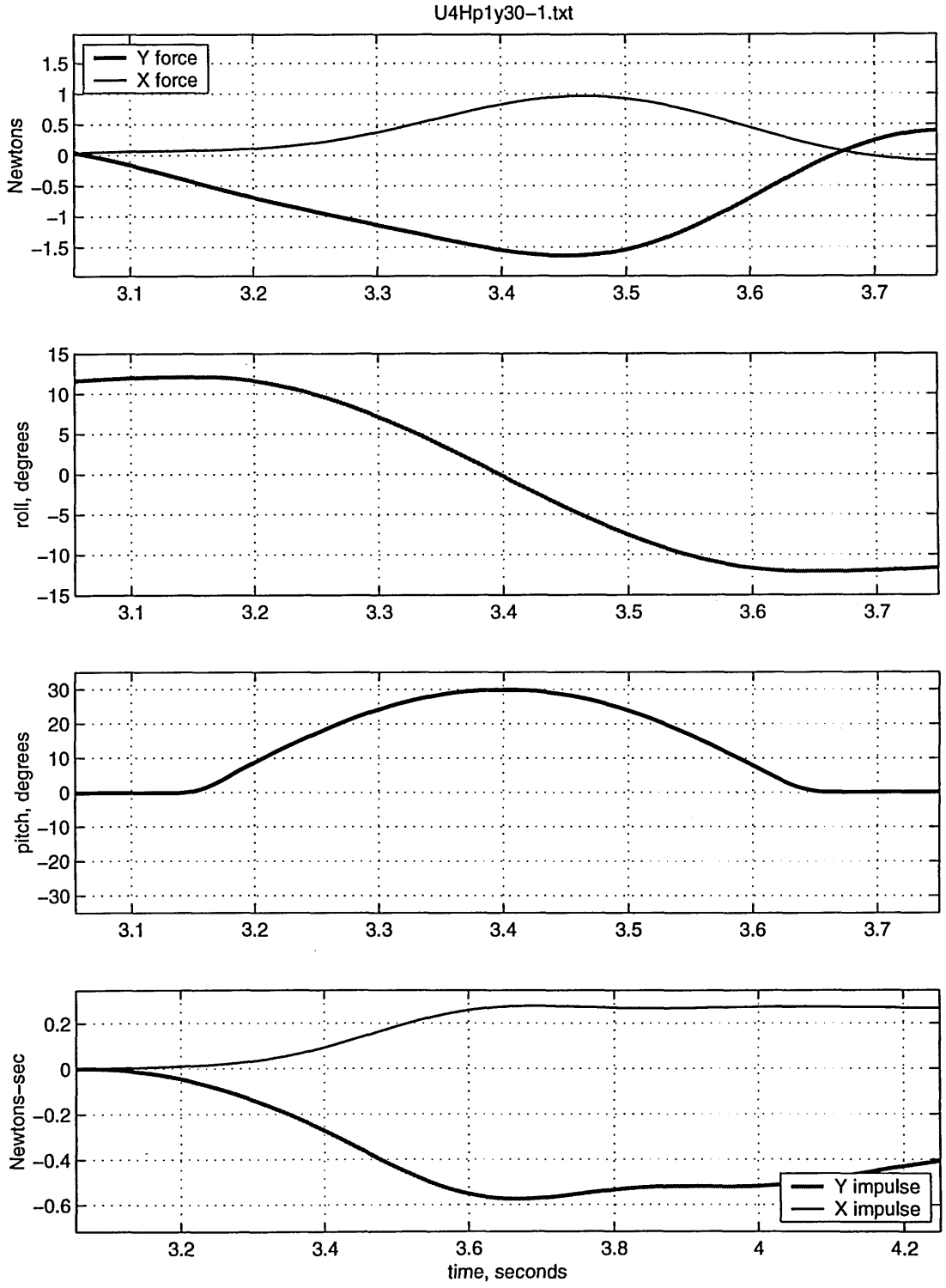

Figure C-22: Half-cycle, $U = 0.4\ m/s$, *Max. Roll Velocity* = 0.51 m/s, $\theta_o = 30°$

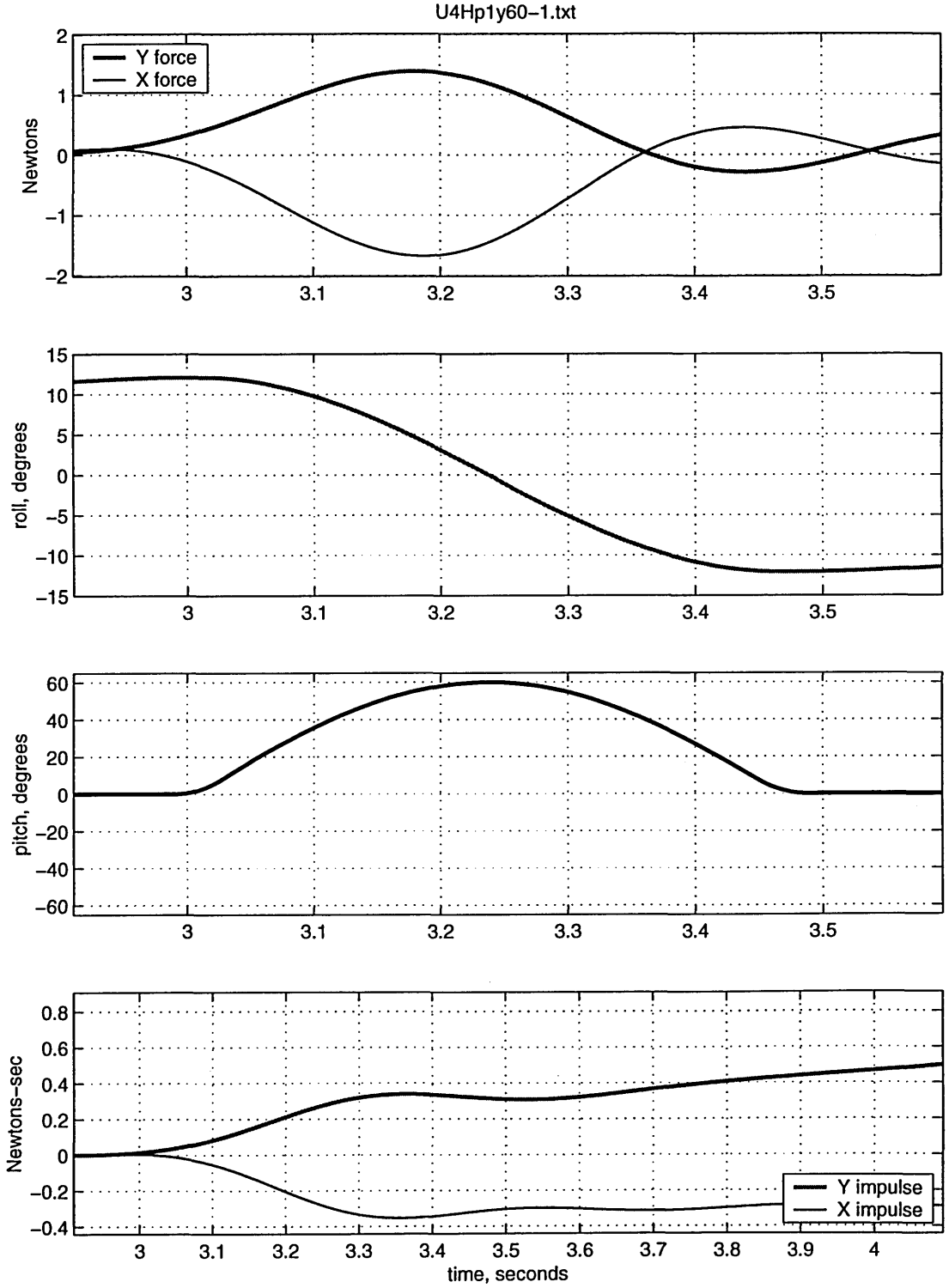

Figure C-23: Half-cycle, $U = 0.4\ m/s$, *Max. Roll Velocity* = 0.51 m/s, $\theta_o = 60°$

Bibliography

[1] M. S. Triantafyllou, G. S. Triantafyllou, and R. Gopalkrishnan. Wake mechanics for thrust generation is oscillating foils. Physics of Fluids, 3:2835-2837, 1991.

[2] M. M. Koochesfahani. Vortical patterns in the wake of an oscillating airfoil. AIAA Paper 87-0111, 1987.

[3] P. Freymuth. Propulsive vortical signature of plunging and pitching airfoils. AIAA Journal, 26:881-883, 1988.

[4] Jamie M. Anderson. Vorticity Control for Efficient Propulsion. PhD thesis, MIT/Woods Hole Oceanographic Institution, 1996.

[5] F. S. Hover, O. Haugsdal, and M. S. Triantafyllou. Control of Angle of Attack Profiles in Flapping Foil Propulsion. Journal of Fluids and Structures, *submitted*, 2003.

[6] D. A. Read, F. S. Hover, and M. S. Triantafyllou. Forces on oscillating foils for propulsion and maneuvering. Journal on Fluids and Structures, 17:163-183, 2003.

[7] G. S. Triantafyllou, M. S. Triantafyllou, and M. A. Grosenbaugh. Optimal thrust development in oscillating foils with application to fish propulsion. Journal of Fluids and Structures, 7:205-224, 1993.

[8] M. S. Triantafyllou, D. S. Barrett, K. Streitlien, and J. M. Anderson. Flapping foils of high propulsive efficiency. 1996.

[9] M. J. Lighthill. Aquatic animal propulsion of high hydrodynamic efficiency. Journal of Fluid Mechanics, 44:265-301, 1970.

[10] Sir James Lighthill. Mathematical Biofluiddynamics. Society for Industrial and Applied Mathematics, Philadelphia, PA. 1975.

[11] J. A. Walker and M. W. Westneat. Labriform Propulsion in Fishes: Kinematics of Flapping Aquatic Flight in the Bird Wrasse Gomphosus Varius (Labridae). J. exp. Biol. 200:1549-1569, 1997.

[12] J. A. Walker and M. W. Westneat. Mechanical Performance of Aquatic Rowing and Flying. Proc. R. Soc. Lond. B 267:1875-1881, 2000.

[13] M. Riedman. The pinnipeds. Berkeley, CA: University of California Press, 1990.

[14] J. E. Kerwin. The MIT Marine Hydrodynamics Water Tunnel - A 53rd Anniversary Celebration Marine Technology, Vol. 31, No. 3, July 1994, pp. 183-194.

[15] E. H. Lurie. Unsteady response of a two-dimensional hydrofoil subjected to high reduced frequency gust loading. Master's thesis, MIT, 1993.

[16] TSI Corporation. System 9100-7 Laser Doppler Velocimeter Instruction Manual P/N1990157, Rev. B, January 1987.

[17] Dantec Corporation. BSA/FVA Flow Software Installation and User's Guide Vol. 1 & 2, Publication # 9040U5714, 4th Edition, 2000.

[18] R. W. Kimball. Experimental investigations and numerical modelling of a mixed flow marine waterjet. PhD Thesis, MIT Department of Ocean Engineering, 2001.

[19] Alexandra H. Techet. PhD thesis, MIT Department of Ocean Engineering, 2001.

[20] C. E. Willert and M. Gharib. Digital particle image velocimetry. Exps. Fluids, 10:181-193, 1991.

[21] R. J. Adrian. Particle-imaging techniques for experimental fluid mechanics. Ann. Rev. Fluid Mech., 23:261-302, 1991.

[22] S. Hoerner. Fluid Dynamic Lift. 2nd Edition, 1985. pg. 4-2.

[23] J. Kerwin. 13.04 Lecture Notes, Hydrofoils and Propellers. 2001. pgs. 115-120.

[24] W. C. Reynolds and L.W. Carr. Review of unsteady, driven, separated flows. AIAA Paper, 85-0527, 1985.

[25] K. W. McAlister, L. W. Carr, and W. J. McCroskey. Dynamic stall experiments on the NACA 0012 airfoil. Technical Paper 1100, NASA, January 1978.

[26] V. Polidoro. Flapping Foil Propulsion for Cruising and Hovering Autonomous Underwater Vehicles. Master's thesis, MIT Department of Ocean Engineering, June 2003.

[27] K. Ogata. System Dynamics. pgs. 546-547, 2nd Edition, Prentice-Hall, 1992.